Field and Frequency Dependence of Ferroelectric-Ferromagnetic Multilayer Heterostructures

Thesis submitted in partial fulfillment of the
requirements for the degree of Doctor of Philosophy

Fernando Javier Aponte Rivera

Department of Physics
University of Puerto Rico -Rio Piedras Campus
San Juan, Puerto Rico

Submitted August 5, 2021

Field and Frequency Dependence of Ferroelectric-Ferromagnetic Multilayer Heterostructures

Accepted by the Faculty of the Doctoral Program in Chemical Physics of the University of Puerto Rico, Rio Piedras Campus, in partial fulfillment of the requirements for the degree of Doctor of Philosophy.

Dr. Ratnakar Palai

Thesis Advisor

Dr. Ram S. Katiyar

Thesis committee member

Dr. Carlos R. Cabrera

Thesis committee member

August 5, 2021

Abstract

Multiferroic composite comprising of ferroelectric and ferromagnetic materials exhibit room temperature magnetoelectric (ME) effects greater than that of single-phase ME known to date. Spin capacitors have the potential to store both the electronic charge and magnetic spin that can produce conventional electric current and spin polarized current. The time evolution of spin polarized electrons injected into the piezoelectric material can be used for accurate sensing of ME fields. Ferromagnetic/Ferroelectric/Ferromagnetic (FM/FE/FM) tri-layer artificial multiferroelectric heterostructures in spin capacitor configuration were fabricated by sputtering ferromagnetic electrodes on lead zirconate titanate (PZT) substrates and depositing PZT on ferromagnetic sheets by Spray Pyrolysis. Magneto-dielectric (MD) measurements were carried out by a wide range of frequencies and magnetic fields at room temperature. We also compared the MD measurements with FM/PZT/Ag and Ag/PZT/Ag. A series of PZT barrier thickness were studied, including 200 μm and 1 mm, and a range of films of 1.4 μm to 7 μm. Ferroelectric polarization hysteresis loops were measured at different magnetic fields to determine the ME polarization of samples with nickel ferromagnets. The nickel spin capacitors have a very peculiar behavior compared to that of the iron and cobalt spin capacitors. Dielectric Peak behavior and positioning was studied for the samples. Different relaxation times are present, dependent on thickness and the presence of the FM material. As well, resonance is present in most samples at the range of $\approx$1 MHz. Impedance spectroscopy show that the samples behave as brick-layer type, having grains and grain boundary interaction, with grain being the main driving factor. The Spray Pyrolysis deposition of PZT on ferromagnetic sheets was successful and yielded results similar of that given by the PZT pre-made substrates.

Acknowledgements

First of all, I give my thanks and deepest love to my family: my mother Beatriz, my father Pascasio, my brother Francisco J. and his wife and children; my great friends Amílcar, Giovanni, Gladys, Juan, Roberto, and Denisse for their continuous love, support, help, and encouragement towards finishing this great feat. To my love Natalia, thank you for all the great love, literal support, and the push needed to finish this and everything ahead of us.

I want to express my greatest respect and gratitude to my advisor Dr. Ratnakar Palai for the continuous support, guidance, inspiration, and suggestions during all my graduate studies and research. His guidance helped me all along the research and writing of my theses. Besides my advisor, I would like to thank the rest of my thesis committee: Dr. Ram S. Katiyar, and Dr. Carlos Cabrera, for accepting this role and their support. Thanks, again to Dr. Ram S. Katiyar whom shared laboratory resources and equipment.

I am thankful to my fellow labmates and friends Dr. Kiran Dasari, Dr. Jaime Santillan, Postdoc Dr. Ricardo Martinez, and Yamile for their immense help, stimulating discussions throughout this research and all of these years in graduate studies research and more. My sincere thanks also go to Dr. G. Srinivasan from the Department of Physics in Oakland University, Rochester, MI, who shared laboratory resources. Thanks to the National Science Foundation (NSF), Partnerships for Research and Education in Materials (PREM), and the Department of Physics of the UPRrp for financial support throughout my graduate studies.

Fernando J. Aponte Rivera

List of Symbols

The following symbols are used throughout this thesis. Other symbols have been used occasionally and are introduced as needed.

2D	Two dimensional	3D	Three dimensional
A	Surface Area	Å	Angstrom
AC	Alternating Current	Ag	Silver
a, b, c	Lattice constants	d	Interplanar spacing
C	Capacitance	Co	Cobalt
C_0	Capacitance with no Dielectric	E_0	External Electric Field
e^-	Electron	ϵ	Dielectric Permittivity
ϵ_0	Dielectric Constant of Free Space	f, v	Frequency
FE	Ferroelectric Material	Fe	Iron
FM	Ferromagnetic Material	h	Planck's constant
L	Inductor	λ	Wavelength
ρ	Charge Density	θ	Angle
M	Modulus	n	Integer
Ni	Nickel	Q	Electric Charge
R	Resistance	Y	Admittance
Z	Impedance		

Contents

List of Figures

List of Tables

Chapter 1

Introduction

1.1 Aims and Outline of the Thesis

The greatest driving force behind the progress and prosperity of society and a great symbol of civilizations has been the application of new materials, ever since the early days. For the 21^{st} century, the development, integration, and application of multifunctional materials have become an important aspect. Oxide materials are of great scientific and technological interest because of their complex and multifunctional properties. The understanding the magnetodielectric (MD) coupling in nanostructured single-phase multiferroics and ferroelectric(FE)/ferromagnetic(FM) heterostructures are very important for the realization of novel magnetoelectric and spintronic devices. The aims for the present study are to enhance, control, and understand the origin of magnetodielectric (MD) coupling in artificially engineered multiferroics using FE and FM materials [1, 2]. Almost all single-phase multiferroics show weak ME and MD coupling. The main hypothesis concerned is that multiferroic heterostructures have a greater coupling between the ferroic orders which in part exceeds that of single-phase magnetoelectric, the combination of a ferromagnetic material with a ferroelectric material will yield a better magnetoelectric coupling. In order to enhance the ME coupling, the present work is focused on artificially engineered multiferroic heterostructures using a combination of ferroelectric/ferromagnetic materials.

In view of the above existing problems and challenges, the objectives of the present work are:

- Fabrication of artificially engineered multiferroic heterostructures using FM/FE/FM spin capacitor configuration with PZT as a ferroelectric.
- Investigation of electric, dielectric, and ferroelectric properties as a function of FE thickness, frequency, and magnetic field for the qualitative and quantitative understanding.
- Study the effect of magnetoelectric and magnetodielectric coupling using different ferromagnets as electrodes.

In the present work, multiferroic heterostructures were built from lead zirconate titanate ($Pb[Zr_xTi_{1-x}]O_3$) as the ferroelectric and coupled with iron (Fe), cobalt (Co), and nickel (Ni) as the ferromagnetic layer using sputtering to grow the ferromagnetic layers. The ferroelectric layer was synthesized for growth using spray pyrolysis and commercially available substrates. Systematic studies of electric, dielectric, and magnetic properties. This thesis consists of 6 chapters. Chapter 1 introduces the fundamental background to understand this research project. It contains information on the classification, the work that has been done, the applications, and emphasis on the materials utilized throughout this research which include Lead Zirconate Titanate ($Pb[Zr_xTi_{1-x}]O_3$), iron, cobalt, and nickel with the fundamental theory background for dielectric measurements and their meaning.

Chapter 2 discuss the experimental details within this research, the synthesis and what is used to characterize the samples. This chapter introduces the key components of sputtering, spray pyrolysis, and solid-state reaction for the

synthesis of $Pb[Zr_xTi_{1-x}]O_3$. Followed with the characterization techniques used to measure and determine all the important information necessary.

Chapter 3, 4, and 5 describes the measurements and data obtained for the multiferroic heterostructure with iron, cobalt, and nickel as ferromagnets, each respectively per chapter. All the measure data and observations are included.

Finally, the thesis will be concluded, and future direction will be given to continue the present research in Chapter 6, here the outlines the outcomes and achievements of the current work will be briefly summarized.

1.2 General Overview

Multiferroic composites comprising of ferroelectric and ferromagnetic materials exhibit room temperature magnetoelectric effects greater that of single-phase magnetoelectrics known to date. Since the effects are mediated at the interface of the coupling between the two ferroic components, the magnetoelectric response should be enhanced by the increase in interface coupling which would improve their quality. This is applied in this thesis project having a composite multi-phase multiferroic heterostructure with the shape: Ferromagnet/Ferroelectric/Ferromagnet with Lead Zirconate Titanate (PZT) as the ferroelectric barrier (FM/PZT/FM). To further understand our samples, their characteristics, and behavior we need to first dive into the theory and history behind the data that we can obtain to get to a viable answer. There are many ways to measure a sample and many different types of procedures, and these all will tell a specific property of the sample being studied. With aims and sets of objectives we can determine which types of measurements to be done and what theoretical background is the most important to understand what we get from the mea-

sured data. As well, we need to understand the substrate and materials being studied, finding out what they are, what makes them important and relevant, and what has been already done with them. Since we utilize ferroic materials of different kinds we dive into what we call the multiferroics, their importance and applications. Further on inside multiferroics, we learn what are our materials, in this case: ferroelectrics and ferromagnets. Then we explore their interactions as a complex system. With this background information we can perform measurements available to us, the physics behind them and what can we learn from such measurements and interpretation of them, having in mind what is physically possible and what has already been recorded. All these aspects will be studied in this thesis and some important information will be mentioned when needed.

This project aim to explore the effects of fabrication of a ferroelectric spin capacitor with structure ferromagnet/ferroelectric/ferromagnet on dielectric and multiferroic properties. Fabrication of effective and usable thin films by spray-pyrolysis for improving its multiferroic properties at room temperature for dielectric uses. Emphasis will be also given to understand the mechanism behind the electric, dielectric, and magnetoelectric coupling.

1.3 Multiferroics

Electronics have gone a long way since the time where they used simple circuits with cables, resistors, inductors, and capacitors. To this day, it has evolved to where one material can house the behavior of more than one of the previous components of circuits in less area and with less net loss of the power required. The combination of materials that are known and the future materials that are studied now can provide to further on the advancement of modern electronics

with the most important outcome, to have materials that are highly efficient and effective with the necessity of less power applied and less net loss. Here comes one of the most influential area of study in modern electronics, the multiferroics. Multiferroic materials are those that exhibit more than one primary ferroic ordering in the same phase, these include: ferromagnetism, ferroelectricity, and ferroelasticity [4]. These materials have recently stimulated a sharply increasing number of research activities for their scientific interest and significant technological promise. The terminology of "multiferroics" extends as well into the non-primary orderings like antiferromagnetism, as well as composites with individual ferroics, and now days is most often used to refer specifically to magnetoelectric materials combining ferroelectric and magnetic behaviors. Importantly, the combination of ferroic orders in multiferroics can lead to coupling between them, so that one ferroic property can be manipulated with the conjugate field of the other, with particular excitement generated by the prospect of switching the orientation of magnetization using an electric field [5, 6]. The combining and control of these simultaneous ferroic orderings is challenging, requiring engineering of new material chemistries, and development of new tools to compute and characterize the novel properties associated with the coupled behaviors. In turn, it offers routes to entirely new device architectures. There are a few promising new materials and combinations emerging, but the most widely studied multiferroic is $BiFeO_3$ [7–11]. The most common path taken in the engineering of new multiferroics is by combining one magnetic and one ferroelectric mechanism into one sample. There are materials that show both ferroelectric and ferromagnetic properties which have a close correlation between the dielectric and magnetic properties that gives a coupling interaction between the ferroelectric and magnetic orders. This kind of magnetoelectric correlation is

defined as the magnetoelectric effect, where there is a magnetization induced by the electric field and magnetic field induced electric polarization [12]. There exists a group of single-phase multiferroics, which means that the ferroelectric and magnetic properties appear in the same phase, whereas there is another group of multiferroic composites which consist of two phases, which these are the ferroelectric and the magnetic phases. In the present, the multiferroic composites are the most attractive choice than to single-phase multiferroics since these have a potentially larger magnetoelectric effects [13]. The concept of multiferroic and magnetoelectric materials with compounds and their classification can be observed in Figure 1.1 [14, 15]. Here we see that ferromagnets (ferroelectrics) form a subset of magnetically (electrically) polarizable materials such as paramagnets and antiferromagnets (paraelectrics and antiferroelectrics) found in the red circle. The area inside the red and green circle are multiferroic materials and the black circle show the materials that demonstrate magnetoelectric coupling. The materials that have a coexistence of ferroelectric, magnetic orders, and exhibit magnetoelectric coupling are called the magnetoelectric multiferroics.

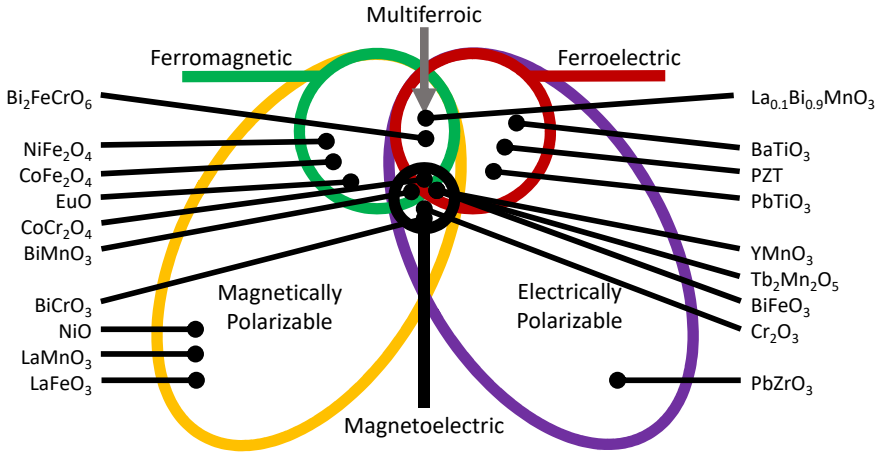

Figure 1.1: Relationship between multiferroic and magnetoelectric materials with examples and their classification.

The biggest challenges to further advance in multiferroics start with discovering new room temperature multiferroics with robust coupling between the ferroelectric and magnetic orders, low leakage, and high remanent magnetic moment. This seems to be the highest priority within the multiferroics research community. For future technology applications, some challenges to overcome are to achieve thermal stability of robust ferroelectric and magnetic order coupling within the 10 nm length scale at room temperature. This requires detailed and continuous research of magnetoelectric and multiferroics phenomena at said scales.

There exist various microscopic origins for the ferroelectricity, with this we can have different types of multiferroics. Generally, there exist two groups categories for multiferroics, these are: Type I multiferroics and Type II multiferroics. These are based on the origin of ferroelectricity in them [16]. Type I multiferroics contain perovskite materials of which ferroelectricity and ferromagnetism have different sources. These materials have weak magnetoelectric coupling, the ferroelectricity typically appears at higher temperatures than magnetism, and they exhibit large spontaneous polarization. Example materials are $BiFeO_3$($T_C{}^{FE}$~1110 K, T_N~643 K, P~90 $\mu C/cm^2$) and $YMnO_3$ ($T_C{}^{FE}$~914 K, T_N~76 K, P~6 $\mu C/cm^2$). These materials have been continually studied since the 1960's and still a major challenge with these materials has been to enhance the values of magnetoelectric coupling coefficient. Type I multiferroics can be further on be divided in subclasses with the basis of origin of ferroelectricity as main subject: ferroelectricity due to shifting B-cation, ferroelectricity due to lone pairs, ferroelectricity due to charge ordering, and Geometric ferroelectricity.

Type II multiferroics are materials that ferroelectricity is originated from magnetism and exhibit strong magnetoelectric coupling. On the other side, these

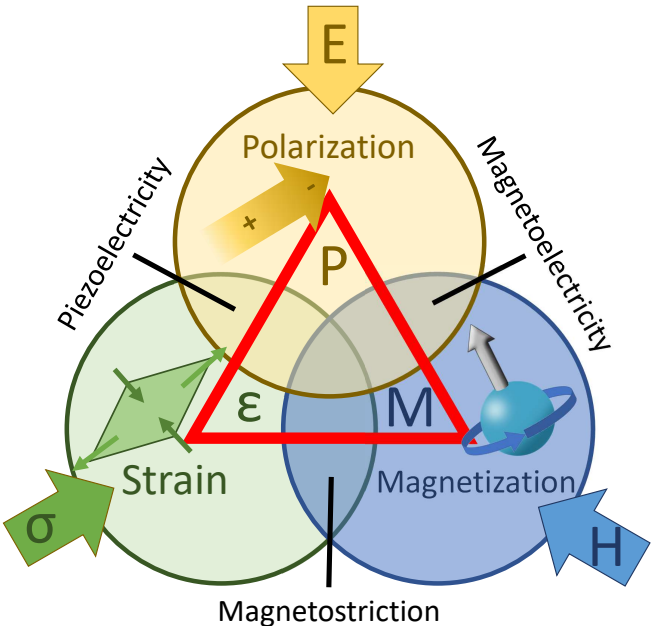

Figure 1.2: Cross coupled effects in ferroics and multiferroics. The electric field E, magnetic field H, and stress σ, control the electric polarization P, magnetization M, and strain ε respectively.

materials tend to have smaller polarization ($\approx 10^{-2}$ μC/cm^2). Most of these materials have been recently discovered, these include $TbMnO_3$ and $TbMn_2O_5$ [17, 18]. With $TbMnO_3$, the polarization rotates by 90° when a critical field is applied in a certain direction [19]. For $TbMn_2O_5$, the influence of the magnetic field is stronger. The polarization changes sign with the magnetic field. With the discovery of these materials, this has pushed for other Type II multiferroics with strong magnetoelectric coupling to be discovered and studied further. Using as a base the mechanism of multiferroic behavior, we can further divide the Type II multiferroics in two subclasses: spiral Type II multiferroics, and Type II multiferroics with collinear magnetic structures.

Another way to get a more enhanced magnetoelectric coupling is by introducing an indirect coupling by strain between two materials such as a ferromagnetic

and ferroelectric, also known as composite or multiferroic heterostructures [20]. Strain coupling requires a good contact between a piezomagnetic (or magnetostrictive) and piezoelectric (or electrostrictive) material. This can be achieved by composites, laminates, or epitaxial multilayers [21–23]. The coupling constant depends on the frequency of the magnetic field. This multiferroics are attractive in technical applications like microwave frequency transducers.

There has been much research done in multiferroics with one of the most popular ideas is that multiferroic bits may be used to store information in the magnetization $\mathbf{M}$ and polarization $\mathbf{P}$. This can bring forth a 4-stage memory, with two $\mathbf{M}\uparrow\downarrow$ and two ferroelectric $\mathbf{P}\uparrow\downarrow$ states [24, 25]. This kind of memory would not need the coupling between ferroelectricity and magnetism. If the magnetoelectric coupling is present then the applications of the device can be done where information is written magnetically but be stored in the electric polarization, this leads to a non-volatile memory.

In the present work, we make an artificially engineered multiferroic heterostructure by coupling a ferromagnetic with a ferro/piezo-electric. This include iron, cobalt, and nickel for the ferromagnetic material and the ferroelectric being the lead zirconate titanate $\mathrm{Pb}[\mathrm{Zr}_x\mathrm{Ti}_{1-x}]\mathrm{O}_3$.

1.4 Ferromagnetism

Iron, nickel, cobalt and some of the rare-earths (gadolinium, dysprosium) exhibit a unique magnetic behavior which is called ferromagnetism with iron (ferrum in Latin) being the most common and most dramatic example. Samarium and neodymium in alloys with cobalt have been used to fabricate very strong rare-earth magnets. Ferromagnetic materials exhibit a long-range ordering phe-

Table 1.1: Important physical and structural properties of Iron, Cobalt and Nickel [47].

Element	Iron	Cobalt	Nickel
Atomic Symbol	Fe	Co	Ni
Atomic Number	26	27	28
Atomic Weight	55.845	58.933	58.6934
Physical State at 20° C	Solid	Solid	Solid
Melting Point	1811 K (1538° C)	1768 K (1495° C)	1728 K (1455° C)
Boiling Point	3134 K (2862° C)	3200 K (2927° C)	3003 K (2730° C)
Density	7.874 g/cm^3	8.90 g/cm^3	8.908 g/cm^3
Crystal Structure	bcc	hcp	fcc
Electron Configuration	[Ar]3d^{6}4s^2	[Ar]3d^{7}4s^2	[Ar]3d^{8}4s^2 or [Ar]3d^{9}4s^1
Element Category	Transition Metal	Transition Metal	Transition Metal
Thermal Conductivity	80.4 W/(m·K)	100 W/(m·K)	90.9 W/(m·K)
Electrical Resistivity	96.1 nΩ·m (at 20° C)	62.4 nΩ·m (at 20° C)	69.3 nΩ·m (at 20° C)
Bohr Magneton (μ_b)	5.4	4.8	3.2

nomenon at the atomic level which causes the unpaired electron spins to line up parallel with each other in a region called a domain. Within these domains, the magnetic field is intense, but when the material comprised of many domains as a bulk sample, will usually be unmagnetized because the many domains within will themselves be randomly oriented with respect to one another. Ferromagnetism manifests itself in the fact that a small externally imposed magnetic field, say from a solenoid or a magnetized material, can cause the magnetic domains to line up with each other according to the external field and the material is said to be magnetized. The driving magnetic field will then be increased by a large factor which is usually expressed as a relative permeability for the material. There are many practical applications of ferromagnetic materials, from the simple electromagnet down to even a transistor [48].

Ferromagnets will tend to stay magnetized to some extent after being subjected to an external magnetic field. This tendency to "remember their magnetic history" is called hysteresis. The fraction of the saturation magnetization which is retained when the driving field is removed is called the remanence of the material and is an important factor in permanent magnets. All ferromagnets

have a maximum temperature where the ferromagnetic property disappears because of thermal agitation. This temperature is called the Curie temperature (T_{C}). Once the material has reached his specific T_{C}, all domains rearrange in a random order which gives a neutral net magnetization, until an external field re-magnetize these domains. The Curie temperature of iron is about 1043 K. The Curie temperature gives an idea of the amount of energy it takes to break up the long-range ordering in the material. At 1043 K the thermal energy is about 0.135 eV compared to about 0.04 eV at room temperature. Ferromagnetic materials can respond mechanically to an applied external magnetic field, which can change its length slightly in the direction of the applied field. This property is called magnetostriction. This can be observed, or rather, heard in the particular hum generated by transformers as they respond mechanically to 60 Hz AC high-voltages [49].

The long range order which creates magnetic domains in ferromagnetic materials arises from a quantum mechanical interaction at the atomic level. This interaction is remarkable in that it locks the magnetic moments of neighboring atoms into a rigid parallel order over a large number of atoms in spite of the thermal agitation which tends to randomize any atomic-level order. Sizes of domains range from a 0.1 mm to a few mm. When an external magnetic field is applied, the domains already aligned in the direction of this field grow at the expense of their neighbors. If all the spins were aligned in a piece of iron, the field would be about 2.1 T. A magnetic field of about 1 T can be produced in annealed iron with an external field of about 0.0002 T, a multiplication of the external field by a factor of 5000. For a given ferromagnetic material the long range order abruptly disappears at a certain temperature which is called the Curie temperature for the material. The Curie temperature of iron is about 1043 K [50].

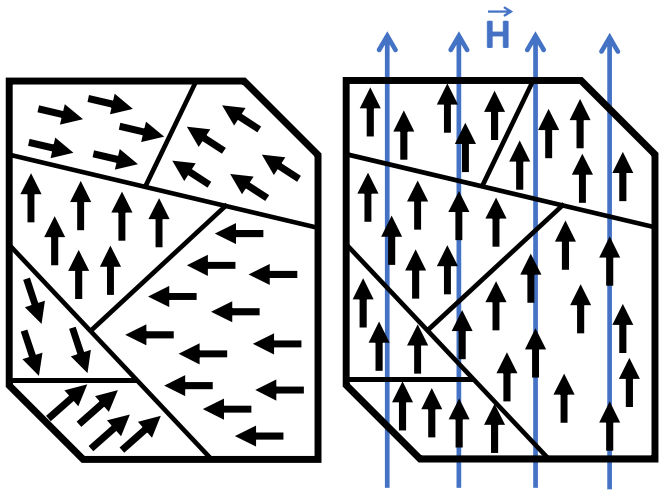

Figure 1.3: Schematic of the magnetic domains affected by an applied field with (a) randomly aligned state and (b) aligned domains by an external field.

1.5 Ferroelectrics

Ferroelectricity is a subset of pyroelectricity and piezoelectricity and are materials that exhibit a reversible spontaneous polarization with the presence and interaction of an electric field [42, 43]. There is a rise in interest for ferroelectric properties that has occupied a place in the modern science and technology many electronic applications. The classification of "ferroelectricity" for a material is similar to that of the term "ferromagnetism", this is where a material has a permanent magnetic moment. Even though the term"ferroelectric" contain the word "ferro", the majority of these materials do not contain iron. The ferroelectric behavior was first discovered by J. Valasek in 1921 on Rochelle salts that had a composition of $NaKC_4H_4O_64H_2O$ [41]. Followed by this, A. von Hippel found in 1944 barium titanate ($BaTiO_3$) to be a ferroelectric material. Today there exists more than 1,000 ferroelectric materials. some of the most important within these are lead titanate ($PbTiO_3$), lead lanthanum zirconate titanate

(PLZT) and lead zirconate titanate (PZT). PZT will be discussed later.

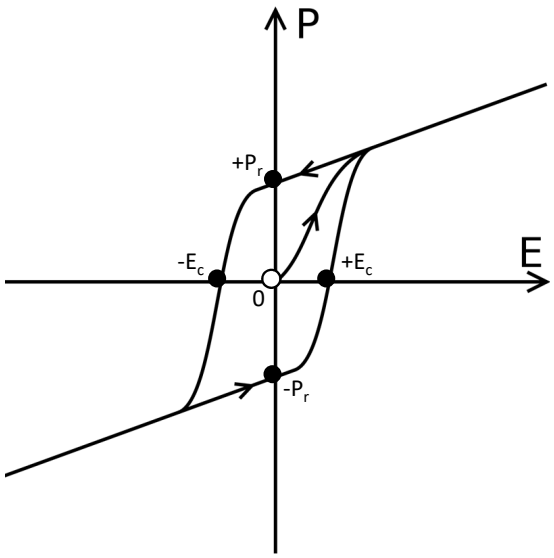

Figure 1.4: Diagram of a typical hysteresis loop.

The ferroelectric materials have nonlinear relationship with polarization '**P**' and the applied electric field '**E**'. This relationship is given by a hysteresis loop, a basic loop can be shown in Figure 1.4. The lengths between points 0 (origin) to '+P_r' and 0 to '-P_r' represent the magnitude of spontaneous polarization, and the direction of spontaneous polarization is called the ferroelectric axis. The lengths from 0 to '+E_c' and of 0 to '-E_c' represent the coercive field strength. The slope of this hysteresis loop of the material, with the absence of an external field, represents the susceptibility of the material. A symmetrical hysteresis loop is the most ideal shape for a loop, since when the positive and negative parts of the coercive field and spontaneous polarization are equal. These parameters and the shape of the loop may be affected by many factors, including temperature, defects, mechanical stress, and electrical measurement conditions imposed on the sample. There are ideas that the occurrence of a hysteresis loop is a consequence of changes in the ferroelectric domain. This includes the growth of existing

anti-parallel domains, nucleation and growth of new anti-parallel domains and domain wall motion. The ferroelectric domains are the regions where there is uniformly oriented spontaneous polarization, and the domain wall is the region between two domains within the material.

The occurrence of a hysteresis loop is suggested to be a consequence of the changes in the ferroelectric domain, such as the growth of existing anti-parallel domains, domain wall motion, and nucleation and growth of new anti-parallel domains, whereby ferroelectric domains are the regions with uniformly oriented spontaneous polarization and the domain wall is the region between two domains [42, 44, 45].

The ferroelectric effects can be related to the crystal classification of the material. There exist 32 different crystal classes, where 11 have a center of symmetry, these are not able to support ferroelectricity. Having aside the O-point group, then the remaining 20 classes do exhibit piezoelectric effects. The pyroelectric crystals are a subset of piezoelectric crystals; here there are 10 classes of crystals from the piezoelectrics that show pyroelectricity. Ferroelectrics are themselves a subset within pyroelectrics, with a condition that they exhibit reversible polarization. When we have an asymmetrical lattice with non-covalent bonds follows to create a ferroelectric crystal. Comparing to one of the most important materials, the diamond crystal is a trihedral structure with symmetrical covalent atoms between all carbon atoms, this gives no net electric fields. Whereas PZT, which is ferroelectric, has a tetragonal structure with asymmetrical and partially ionic bonds between the oxygen atoms and metals. These crystals show large dielectric constant and high coupling factor. Polycrystalline ceramics of these materials show ferroelectric effect only after poling or aligning the dipoles.

Ferroelectrics have a wide variety of applications, of which include: capacitors, non-volatile memory, ferroelectric liquid crystals for displays, thermistors, light deflectors, modulators, displays, sensors and actuators. Capacitors are simple structures (as shown in Figures 1.7, 1.8, and 2.20, where we have metal plates divided by space or a dielectric, in this case we replace the dielectric with a ferroelectric. The polarization of charges and direction of polarization of the ferroelectric material within the capacitor are shown in Figure 1.7. They are used in digital electronics as part of ferroelectric RAM and in analog electronics as tunable capacitors (varactors). They act as powerful capacitors because they are able to achieve very high dielectric constants, up to 30,000 for perovskites. When a metal-ferroelectric-metal structure is in short circuit, the charge accumulation occurs at the metal-ferroelectric interface and, thus, electric displacement of the ferroelectric is screened. This results in a decrease in voltage across the ferroelectric capacitor [52]. Ferroelectric capacitors, when they are utilized on memory applications, they are used as a way to store logical value of data. Being used as part of a memory, the data value is read by applying an electric field. Application of a "read" electric field allows the measurement of the amount of charge needed to flip the memory cell to the opposite state, with this revealing the previous state of the cell. When the electric field is applied during the read operation, this destroys the current memory state which needs to be followed by a write operation so to write the bit back in. This is a limiting factor for single ferroelectrics utilized as a memory element, where a read cycle needs to be accompanied by a write cycle. It also has a high, but not infinite, write cycle limit [53].

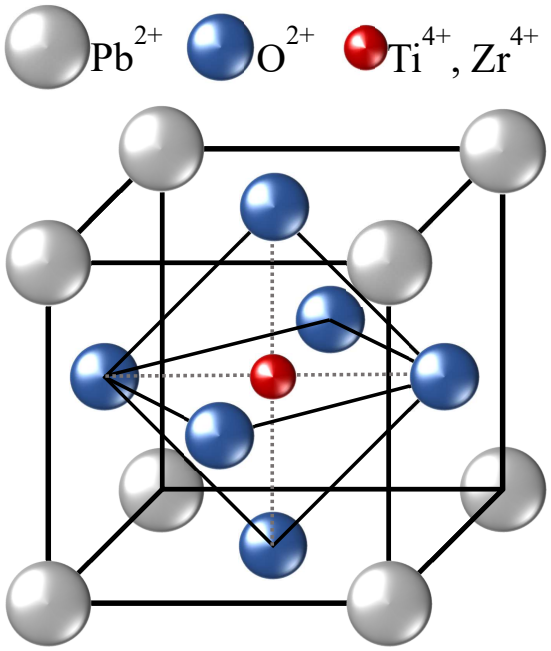

Figure 1.5: Perovskite crystalline structure of Lead Zirconate Titanate (PZT).

1.5.1 Lead Zirconate Titanate (PZT)

Lead Zirconate Titanate (PZT) with the chemical composition formula $Pb[Zr_xTi_{1-x}]O_3$, is one of the worlds most widely commercially used piezoelectric ceramic materials. PZT has a perovskite crystal structure, each unit of which consists of a small tetravalent metal ion in a lattice of large divalent metal ions. In the case of PZT, the small tetravalent metal ion is usually titanium or zirconium. The large divalent metal ion is usually lead. Under conditions that confer a tetragonal or rhombohedral symmetry on the PZT crystals, each crystal has a dipole moment. The lattice constant for PZT is 4 $\mathring{A}$, and this lattice constant decreases when the temperature decreases. Below the Curie temperature, the lattice shrinks and distorts. A simple representation of the lattice at this stage, shown in Figure 1.5, can be described as: the body-centered atom slides up approximately 0.05 $\mathring{A}$ above the plane of the oxygen atoms. The electron

Table 1.2: Important physical and structural information of lead zirconate titanate [46].

Name	Navy Type II (PZT-5A)
Formula	$Pb[Zr_xTi_{1-x}]O_3$
Crystalline Structure	Perovskite
Material Type	Ceramic
ϵ_r	1800
Bandgap	$\sim$ 3.53 eV
Curie Temperature	$>$ 200° C
$\mathbf{d_{33}(x10^{-12}m/V)}$	350
Polarization	39 $\mu C/cm^2$

occupation remains mostly around the oxygen atoms, and a net vertical dipole is created [51]. Extra information about PZT can be found in Table 1.2.

At high temperatures and pressures for all perovskites, the cubic prototype structure is always expected. Perovskites have attracted much attention due to coupling of spin, charge and orbital ordering which offers a wide range of electric, magnetic, transport and multiferroic properties [42]. In perovskite structure, the structural phase transitions are attributed to doping or changes in the physical parameters (i.e., temperature, pressure, electric field). The perovskite structure is very flexible because it can accommodate atoms of variable valence. The physical properties (i.e., ferroelectricity, colossal magneto-resistance, superconductivity, charge ordering and spin-dependent transport) of the perovskites are influenced by structural changes which are significant from application point of view [42-46].

1.6 Spintronics

The term "spintronics" (from the words spin electronics) is used to encompass the area that studies the active control and manipulation of spin degrees in solid state systems [34]. Spintronics, differs from conventional charge transport in that spin is a non-conserved quantity in solids, in part due to spin-orbit coupling. The term "spin" comes from either the spin of a single electron "e^-", this can be detected by its magnetic moment, or by the average "spin" of a group of electrons which are present by magnetization. Then, to set the control of spins of either the population and the phase of the spin of a group of particles, or a manipulation of the spin of a single or small group spin system. With spintronics, it is tried to understand the interactions between the spin of the particle within the solid state environment and with this to take advantage of their properties to make new useful devices. Important information that is constantly studied on spintronics is the most effective ways to polarize the spins in the system, to determine the effective time of the remembered spin orientation and to detect this spin moments [33–35].

There are several ways to achieve a spin polarization, which in turn is a non-equilibrium state in spin, of which commonly is done by optical methods by which circularly polarized photons transfer their angular momenta to electrons [36–40]. A second method is by electrically injecting the spin polarization, this method is the most wanted [54]. By electrically injecting the spin polarization, a magnetic electrode must be connected to the sample. When this electrode is being electrically driven, the spin polarized electrons inject into the sample, this creates a non-equilibrium spin accumulation in the sample. The rate at which the spins accumulate will depend on the spin relaxation, this is the process that happens when the spins accumulated return to a state of equilibrium. Several

mechanisms for spin relaxation are known, most of them involving the coupling of spin and orbit which has a potential that is dependent of the spin with momentum scattering that provides a randomizing force. Most of the time scales for spin relaxation within electronic systems is in the range of nanoseconds. In the end, what its mostly sought after is to maximize the spin detection sensitivity to a point in which what is detected is the changes in spin and not the spin itself. With this and Multiferroics, we have a connection, where we use magnetism and ferroelectrics to have a combination of both worlds and dive further into two-phase composite multiferroics.

1.7 Dielectric Resonator Oscillator

Dielectrics have many uses, not only can they be used in computational electronics, they can be used in communications as antennas as well. With the rapid increase of information quantity needed to be transported from one place to another, antennas need to update for the demand of the ever growing communications world. Antennas need to transmit more information and at better speeds and rates than before. These antennas need to accommodate for larger bandwidths, higher gain, smaller in size, and temperature resilience. Various front-end antenna solutions relying on monopoles, dipoles, and patch antennas have been proposed for millimeter-wave applications. These antennas are characterized by small size, low weight, and low cost and can be easily integrated on chip. However, unless advanced design solutions based on the integration of suitable dielectric superstrates or lensing structures are adopted, these antennas typically suffer from reduced radiation efficiency and narrow impedance bandwidth due to the effect of lossy silicon substrate materials. On the other

hand, dielectric resonator antennas (DRAs) are promising candidates to replace traditional radiating elements at high frequencies, especially for applications at millimeter waves and beyond. The DRAs depend on radiating resonators that can convert guided waves into unguided waves (RF signals) [58]. There are many advantages to the use of dielectric resonator oscillators (DROs) in antennas and it starts with the size. The size of a DRA is proportional to:

$$\lambda_0 = \sqrt{\epsilon_r} \tag{1.1}$$

$$\lambda_0 = c/f_0 \tag{1.2}$$

with λ_0 being the free-space wavelength at a resonant frequency f_0, and ϵ_r is the relative permittivity of the material forming the radiating structure. Where on the other hand, traditional metallic antennas size is proportional to λ_0. With a higher dielectric constant material at hand, the form factor of the DRA becomes smaller in size.

Another advantage is that since there are no conducting materials within the DRA, this characterize it by high radiation efficiency when a low-loss dielectric material is chosen. This characteristic makes them very suitable for applications at very high frequencies, such as in the range from 30 GHz to 300 GHz. Traditional metallic antennas suffer from higher conductor losses when these higher frequencies are reached.

When using the correct excitation technique, any dielectric structure can become a radiator at a defined frequency, and for a given frequency, the size of the DRO is inversely proportional to the relative permittivity of the constitutive material. There has been research done with the lowest dielectric constant

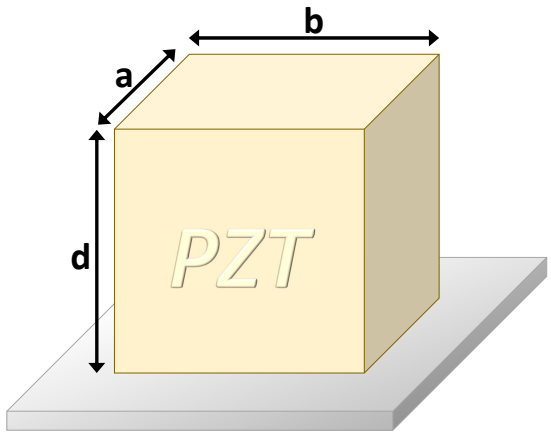

Figure 1.6: 3-Dimensional schematic of a square shaped dielectric.

material for DRA design where plastics with relative dielectric constant smaller than 3 were utilized for supershaped DRAs [59, 60].

The rectangular shaped three-dimension DRA shown in Figure 1.6 consists of a rectangular dielectric resonator with relative dielectric constant ϵ_r with three independent geometrical dimensions a, b, and d (see Figure 1.6); has an advantage having three dimensions to characterize it geometrically, this offers more design flexibility as compared to a cylindrical DRO. Furthermore, the rectangular DRO is characterized by low cross-polarization level as compared to the cylindrical DRO [61]. Using the dielectric wave guide model to analyze the rectangular DRA, while it is mounted on a ground plane, the TE modes are excited. The resonant frequency of the fundamental mode (TE_{111}) is calculated by the following equation:

$$f_0 = \frac{c}{2\pi\sqrt{\epsilon_r}}\sqrt{k_x^2 + k_y^2 + k_z^2} \tag{1.3}$$

$$k_x = \frac{m\pi}{a} \tag{1.4}$$

$$k_y = \frac{n\pi}{b} \tag{1.5}$$

$$k_z = \frac{p\pi}{d} \tag{1.6}$$

1.8 Polarization

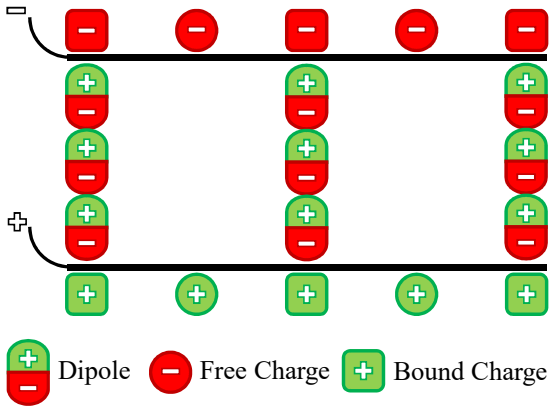

Figure 1.7: Schematic of a polarized dielectric.

Dielectric materials have the advantage to increase the storage capacity of a capacitor by neutralizing charges at the electrode surfaces which could have contribute to the external field. In Figure 1.7, we have the action of dipole chains which form under the influence of the applied field and bound countercharges with their free ends on metal surfaces. Utilizing the equations of capacitance:

$$Q = C_0 V \tag{1.7}$$

$$C = C_0 \frac{\epsilon'}{\epsilon_0} = C_0 \epsilon' \tag{1.8}$$

we can write the capacitor's voltage as follows:

$$V = \frac{Q}{\epsilon'} \cdot \frac{1}{C_0} \tag{1.9}$$

We can interpret this equation saying that only a fraction of the total charge 'Q', the free charge 'Q/ϵ'', contributes to the voltage whereas the remaining bound charge '$Q(1 - \frac{1}{\epsilon'})$', is neutralized by the polarization within the dielectric. The total charge 'Q' concentrated in the capacitor is distributed over the surface area of the metal electrodes 'A' with density 's':

$$Q = \int_A s \; dA \tag{1.10}$$

The true charge density 's' is represented by the vector '**D**', with the electric flux density in such that the surface charge density is equal to '**D**', which is the normal component. This can be shown as:

$$s \; da \equiv D \cos\alpha \; dA \equiv \mathbf{D} \cdot \mathbf{n} \; dA = D_n \; dA \tag{1.11}$$

When there is a positive value of the scalar (dot product) of the vector **D** and the unit vector **n** means that it is a positive charge. With this we can assign to the free charge density s/ϵ' vector **E** (electric field strength intensity) by defining:

$$\frac{s}{\epsilon'} \; dA \equiv \epsilon_0 \mathbf{E} \cdot \mathbf{n} \; dA = \epsilon_0 E_n \; dA \tag{1.12}$$

Then, adding to the bound charge density a vector **P** (polarization) as:

$$s(1 - \frac{1}{\epsilon'}) \; dA \equiv \mathbf{P} \cdot \mathbf{n} \; dA = P_n \; dA \tag{1.13}$$

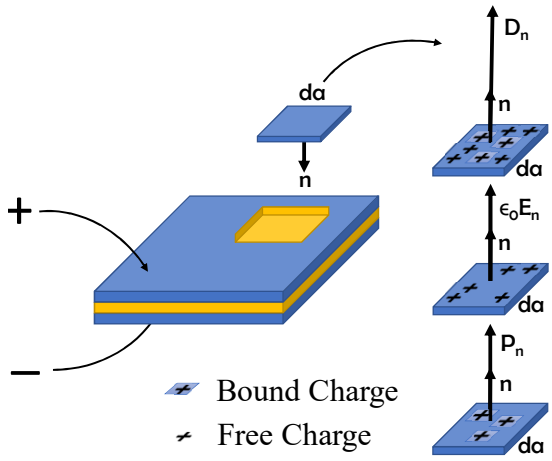

Figure 1.8: Schematic representation of total, free, and bound charge densities by field vectors.

As the Figure 1.8 represent how the total, free and bound charge densities are connected to the field vector. With Equations 1.11 and 1.12 we can show the relationship between the dielectric flux density and the field strength with:

$$\mathbf{D} = \epsilon' \mathbf{E} \tag{1.14}$$

Utilizing equations 1.11 up to 1.13 we can interrelate between the three field vectors as:

$$\mathbf{P} = \mathbf{D} - \epsilon_0 \mathbf{E} = (\epsilon' - \epsilon_0)\mathbf{E} \tag{1.15}$$

$$\mathbf{P} = \chi \epsilon_0 \mathbf{E} \tag{1.16}$$

Then, the factor is defined as:

$$\chi = \frac{\mathbf{P}}{\epsilon_0 \mathbf{E}} = \epsilon' - 1 = \frac{Bound\ Charge\ Density}{Free\ Charge\ Density} \tag{1.17}$$

With this, the factor is known as the electric susceptibility of the dielectric material. The electric flux density **D** and polarization **P** both have the dimension of "charge per unit area". The electric field **E**, on the other side, can be defined a different physical meaning, this is because the dimensions of the dielectric constant are yet to be chosen. Using this we can extend the concept of electric field in space by saying that an electric probe charge *Q'* placed on a electric field with intensity **E** is subjected to a force as:

$$\mathbf{F} = Q'\mathbf{E} \tag{1.18}$$

Then, the electric field strength **E** becomes equal in magnitude and direction to the force per unit charge that acts on the probe charge, with this the dielectric constant becomes as follows, with dimensions:

$$[\epsilon] = [\frac{Charge\ per\ unit\ area}{Force\ per\ unit\ area}] \tag{1.19}$$

If we have two charges of opposite strength polarity (± Q) separated by a distance *d*, it will represent a dipole with a moment:

$$\mu = Q\mathbf{d} \tag{1.20}$$

This is the electric dipole moment symbolized by a vector with magnitude $|\mu|$, which is pointing from the negative pole towards the positive pole. This can be observed in Figure 1.9

The polarization vector **P** then corresponds in magnitude to the surface charge density bound at the electrodes by the polarized dielectric, it points in the direction of the applied field. The polarization **P** is the same as the electric dipole moment per unit volume of the dielectric material.

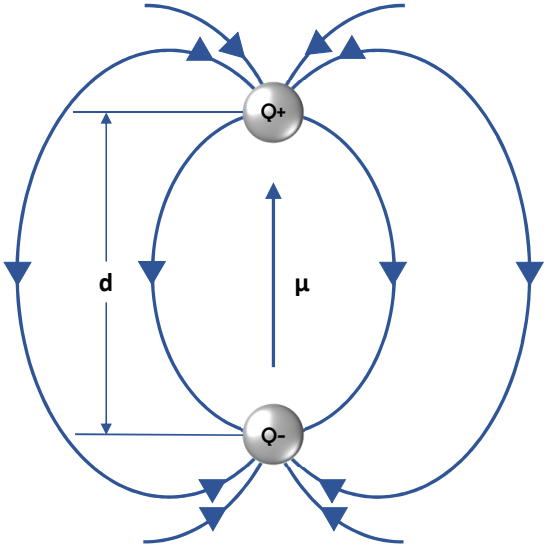

Figure 1.9: Electric dipole moment represented by Equation 1.20.

1.9 Relaxation

When talking about solid state resonance of electronic excitation and vibration, they do not occur because of individual particles, they fall to the electronic and vibrational states of the condensed matter. To turn molecules or molecular groups it's required to have space, and space is very scarce inside a solid. At the same time, the permanent dipole moments of molecular groups are very characteristic parts elemental in the formation of the condensed phases. These are built into their surroundings, which limits free rotation to impossible and the quantized rotation spectra disappears. The classical way in physics to show the dispersion formula of electrical, atomic, or molecular resonance in the gaseous state is as a LRC (Inductor-Resistance-Capacitor) circuit that is shunted by a capacitor. Here we consider that the condensed phases of the liquids and solids act as polar molecules rotating in a medium of dominating friction. Considering the RC circuit, the admittance is:

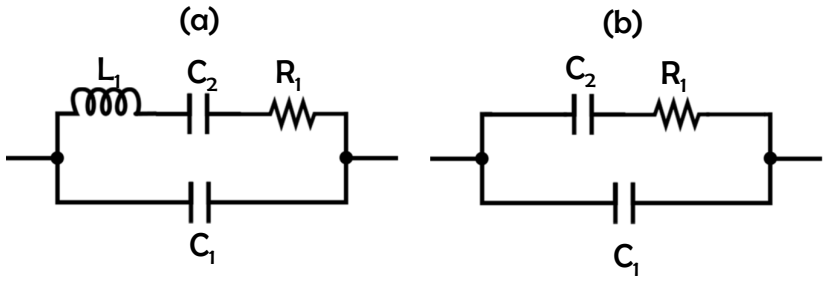

Figure 1.10: Equivalent circuits of a (a) free resonator molecule and a (b) rotator molecule in a medium of dominating friction.

$$Y = j\omega C_1 + \frac{1}{Z_2} \tag{1.21}$$

With $j{=}\sqrt{-1}$, ω is the angular frequency ($\omega{=}2\pi f$), and the impedance of capacitor 2 being:

$$Z_2 = R_2 + \frac{1}{j\omega C_2} \tag{1.22}$$

When the capacitor C_2 is charged to a voltage $\mathbf{V}_0$ and having the circuit shorted across the R_2 - C_2, then we have a transient:

$$\mathbf{V_2} = \mathbf{V_0} e^{-\frac{t}{R_2 C_2}} \tag{1.23}$$

With this we can observe the voltage dropping with a relaxation time $\tau = R_2 C_2$. With this we can follow the Debye relaxation, with the specific complex permittivity of the RC circuit being:

$$\epsilon* = \frac{C_1}{C_0} + \frac{C_2}{C_0}\frac{1}{1 + j\omega\tau} \tag{1.24}$$

Now we can introduce the specific permittivity for the "zero" frequency being:

$$\epsilon'_s = \frac{C_1}{C_0} + \frac{C_2}{C_0} \tag{1.25}$$

And having the "infinite" frequency we get:

$$\omega \gg \frac{2\pi}{\tau} \tag{1.26}$$

$$\epsilon'_\infty = \frac{C_1}{C_0} \tag{1.27}$$

And now we have the equation for the complex dielectric constant assuming the general formulation:

$$\epsilon* = \epsilon'_\infty + \frac{\epsilon'_s - \epsilon'_\infty}{1 + j\omega\tau} \tag{1.28}$$

Now with these equations we have a resonance spectrum of rotation that has been replaced by a relaxation spectrum.

Relaxation frequency is generally expressed as:

$$f_r = \frac{1}{2\pi RC} \tag{1.29}$$

$$RC = \tau \tag{1.30}$$

where τ is the relaxation time. The relaxation time due to the bulk effect is calculated using the relation:

$$\tau_b = R_b C_b \tag{1.31}$$

The values for R_b and C_b can be obtained from the fitting data of Equa-

tion 2.31 and 2.32.

1.10 Damping

Damping is a property of the materials that is very important for vibrational control. For electromechanical damping, the structure treatment is necessary to consider three parameters: damping, mass, and stiffness. These parameters are needed to design and optimize piezoelectric transducers and resonators by using numerical modeling since all of them have an effect in piezoelectric transducer dynamic response. Systems that, for the most part, dissipate energy by vibration are non-linear. In this case, it is necessary to develop models of ideal damping with fair and satisfactory approximation. There are several types of damping, which are: viscous damping (due to energy dissipation), structural damping (due to material properties), and friction damping (due to mechanical sliding between surfaces). Viscous damping occurs mostly in piezoelectric transducer vibration at low kHz range. Because of this, in this work, only viscous damping is explained and utilized.

1.10.1 Viscous Damping

When a mechanical system is oscillating in a fluid medium, such as air, gas, water and oil, the fluid resistance to body movement causes energy dissipation. The dissipated energy and its magnitude are dependent on many factors, such as: size, body shape, fluid viscosity, frequency vibration and body vibration velocity. With viscous damping, the damping forces can be expressed as:

$$F = c\dot{u} \tag{1.32}$$

where c is a proportionality constant and $\dot{u}$ is the body velocity. When the single mass-spring system is freely oscillating, the motion equation is:

$$m\ddot{u} + c\dot{u} + ku = 0 \tag{1.33}$$

where $\ddot{u}$ is the body's acceleration, m is the mass and k is the modal stiffness. Solving equation 1.33 for u, we obtain:

$$u = \left[A \exp\left(i\sqrt{\frac{k}{m} - \left(\frac{c}{2m}\right)^2} t \right) + B \exp\left(-i\sqrt{\frac{k}{m} - \left(\frac{c}{2m}\right)^2} t \right) \right] \exp\left(-\frac{c}{2m} t \right) \tag{1.34}$$

where A and B are arbitrary constants that are dependent on motion starting. Analysis of influence of stiffness, mass and damping, in the resonance frequency ω_r of the system, can be obtained from exponential radical of equation 1.34, giving:

$$\omega = \sqrt{\frac{k}{m} - \left(\frac{c}{2m}\right)^2} t \tag{1.35}$$

Each term contributes in the response curve of the piezoelectric and non-piezoelectric material. In terms of resonance frequency, by decreasing the mass, the resonance frequency increases; by increasing stiffness, the resonance frequency increases; and by increasing the damping, the resonance frequency decreases by little and there occurs an amplitude displacement.

The damping behavior of a damped system is dependent on numerical values in equation 1.35. Considering the resonance frequency expression of $\omega = k/m$, the critical damping (c_c) can be obtained:

$$\left(\frac{c_c}{2m}\right)^2 = \frac{k}{m} \tag{1.36}$$

$$c_c = 2m\omega_n \tag{1.37}$$

A very important parameter used to describe the damping properties is the mechanical damping coefficient:

$$\zeta = \frac{c}{c_c} = \frac{c}{2m\omega_n} \tag{1.38}$$

The relationship between natural resonance frequency, of a non-damped system, and resonance frequency of a damped system is obtained by equations 1.35 and 1.38:

$$\omega_r = \omega_n\sqrt{1-\zeta^2} \tag{1.39}$$

Then we have the Rayleigh equation, which is the common way to describe the damping coefficient:

$$c = \alpha m + \beta k \tag{1.40}$$

where α is the mass multiplication factor and β is the stiffness multiplication factor. With this, different physical damping can be modeled by determining α and β values. The relationships of these values are:

- Non-damped ($\alpha = 0$ and $\beta = 0$)
- Viscous damping ($\alpha = 0$ and $\beta > 0$)
- Damping proportional to the mass ($\alpha > 0$ and $\beta = 0$)

- Rayleigh damping ($\alpha > 0$ and $\beta > 0$)

The values for α and β are dependent on energy dissipation characteristics of the structure. Usually, piezoelectric vibrations occur with viscous damping. This means that $\alpha = 0$, and β can be determined by known values of ζ and ω_r, which represent structural mechanical damping. When a structure is under an harmonic excitation, it can be modeled as subjected to viscous damping with coefficient:

$$\beta = \frac{1}{\omega Q_m} \tag{1.41}$$

with Q_m being the mechanical quality factor. Q_m can be experimentally determined through electrical impedance spectroscopy analysis by resonance and anti-resonance frequencies of mode shape r.

Resonators that are sinusoidally driven that present a high Q factor will resonate with greater amplitudes, at the resonant frequency, and in turn have a smaller range of frequencies around their resonant frequency. This range of frequencies that the oscillator resonates is called the bandwidth. This helps in radio receiver application where a high Q tuned circuit may be more difficult to tune but in turn it would have more selectivity, this means that it will do a better job at filtering out signals from different frequencies (or stations) that are close in the spectrum. These high Q resonators oscillate with a smaller range of frequencies and are more stable.

The idea of the parameter Q was originated by K. S. Johnson, who worked at Western Electric Company. He evaluated the quality of inductor coils and utilized the letter Q as a symbol since at that time all other letters of the alphabet were taken. Later came the association of the word "Quality" and "Quality Factor"

with Q as the abbreviation. [62–64]

For resonant devices. there are two common definitions for Q. these are not equal at smaller values and approximate to each other at higher Q factors. This means that the resonator becomes less damped. One of these definitions is a ratio between the frequency to bandwidth of the resonator:

$$Q = \frac{f_r}{\Delta f} = \frac{\omega_r}{\Delta \omega} \tag{1.42}$$

where f_r is the resonant frequency, $\Delta\ f$ is the resonance width measured as "full width at half maximum" (FWHM), which means the bandwidth over which the power of vibrations is greater than half the power at the resonant frequency. $\omega_r = 2\pi\ f_r$ is the angular resonant frequency and $\Delta\ \omega$ is the angular half power bandwidth. This term represents Q as the reciprocal of fractional bandwidth. The Q factor determines the qualitative behavior of damped oscillators and can be interpreted in three ways: low Q factor ($Q<\frac{1}{2}$), high Q factor ($Q>\frac{1}{2}$), and intermediate Q factor ($Q=\frac{1}{2}$). This information can be obtained from the peak in the imaginary part of the impedance as shown in Figure 1.11. This peak has its highest Y value at 15.9 kHz, defining the value for f_r shown as the red line in the figure, and a value for FWHM of 55509.9, being $\Delta\ f$ and shown as the blue line in the Figure1.11. This example is for PZT deposited by SPL, with a film thickness of 2 μm.

A low Q factor is a resonant system that is overdamped. This system barely oscillates, when displaced from its equilibrium steady state output it returns to it by an exponential decay as it approaches the steady state asymptotically. The damping coefficient can be determined utilizing Equation 1.41, with information obtained by the imaginary peak of the impedance as shown in Figure 1.11 [65].

Following the value of the Q factor, we can determine if the oscillating system

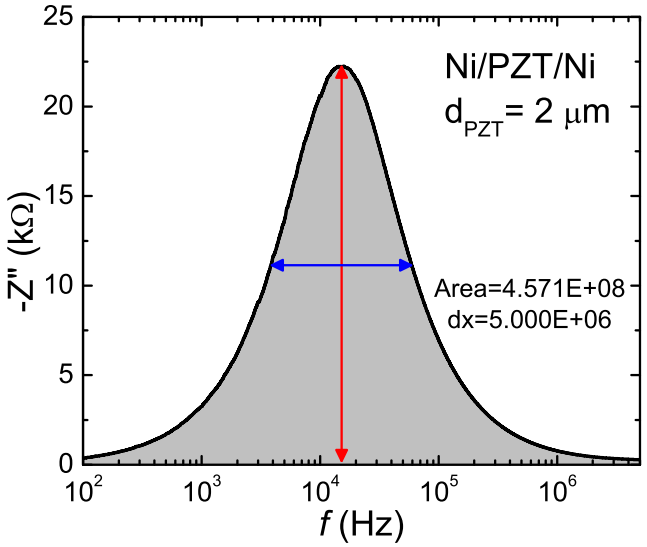

Figure 1.11: Imaginary part (Z") of the impedance of a sample plotted to find the peak center frequency (in red), and Full Width at Half Maximum (FWHM in blue) value for the determination of the Q factor and damping coefficient.

is either damped or not, and if it is damped, whether it's over or underdamped. The following equation is utilized to determine the damping ratio:

$$\zeta = \frac{1}{2Q_m} \tag{1.43}$$

If the value of $\zeta = 0$, then it is and undamped simple harmonic oscillating system. If $0 \leq \zeta < 1$, then it is referred to an underdamped system. When $\zeta > 1$, the system is overdamped. And a system is called "critically" damped when $\zeta = 1$. This is the border between the over and underdamped cases.

References

[1] Pimenov, A., Mukhin, A., Ivanov, V. et al. Possible evidence for electromagnons in multiferroic manganites. Nature Phys 2, 97100 (2006)

[2] G. Lawes, A. P. Ramirez, C. M. Varma, and M. A. Subramanian, "Magnetodielectric Effects from Spin Fluctuations in Isostructural Ferromagnetic and Antiferromagnetic Systems", Phys. Rev. Lett. 91, 257208-1-4 (2003)

[3] H. Palneedi, D. Maurya, L.D. Geng, H.-C. Song, G.-T. Hwang, M. Peddigari, V. Annapureddy, K. Song, Y.S. Oh, S.-C. Yang, Y.U. Wang, S. Priya, J. Ryu, Enhanced Self-Biased Magnetoelectric Coupling in Laser-Annealed Pb(Zr,Ti)O 3 Thick Film Deposited on Ni Foil, ACS Appl. Mater. Interfaces. **10** (2018)

[4] Schmid, H. Multiferroic magnetoelectrics. Ferroelectrics **162**, 317338 (1994)

[5] Fiebig, M. Revival of the magnetoelectric effect. J. Phys. D **38**, R123R152 (2005)

[6] Ramesh, R., Spaldin, N. A. Multiferroics: progress and prospects in thin films. Nat. Mater. **6**, 2129 (2007)

[7] Wang, Y., Hu, J., Lin, Y., Nan, C.-W. Multiferroic magnetoelectric composite nanostructures. NPG Asia Mater. **2**, 6168 (2010)

[8] Pyatakov, A. P., Zvezdin, A. K. Magnetoelectric and multiferroic media. Phys.-Uspekhi **55**, 557581 (2012)

[9] Tokura, Y., Seki, S., Nagaosa, N. Multiferroics of spin origin. Rep. Prog. Phys. **77**, 076501 (2014)

[10] Dong, S., Liu, J.-M., Cheong, S. W., Ren, Z. Multiferroic materials and magnetoelectric physics: symmetry, entanglement, excitation, and topology. Adv. Phys. **64**, 519626 (2015)

[11] Fiebig, M., Lottermoser, T., Meier, D., Trassin, M. The evolution of multiferroics. Nat. Rev. Mater. **1**, 16046 (2016)

[12] Hill, N. A. Why are there so few magnetic ferroelectrics? J. Phys. Chem. B **104**, 66946709 (2000)

[13] Vaz, C. Magnetoelectric coupling effects in multiferroic complex oxide composite structures. Adv. Mater. **22**, 29002918 (2010)

[14] W. Eerenstein, N. D. Mathur and J. F. Scott, Nature **442**, 759 (2006)

[15] H. Ba, M. Gajek, M. Bibes and A. Barthlmy, J. Phys.:Condens. Matter **20**, 434221 (2008)

[16] D. Khomskii, Physics **2**, 20 (2009)

[17] T. Kimura, Nature **426**, 55 (2003)

[18] N. Hur, Nature **429**, 392 (2004)

[19] S. J. Gong and Q. Jiang, Phys. Lett. A **333**, 124 (2004)

[20] A. M. J. G.van Run, D. R. Terrell, J. H. Scholing, J. Mater. Sci. **9**, 1710 (1974)

[21] J. Ryu, A. Vasquez Carazo, , K. Uchino, H.-E. Kim, Jpn. J. Appl. Phys. **40**, 4948 (2001)

[22] N. Cai, C.-W. Nan, J. Zhai, Y. Lin, . Appl. Phys. Lett.**84**, 3516 (2004)

[23] G. Srinivasanet al., Phys. Rev. B **65**, 134402 (2002)

[24] J. F. Scott, Nature Mater. **6**, 256 (2007)

[25] A.J. Moulson and J.M. Herbert, Electroceramics : Materials, Properties and Application Chapman and Hall (1990).

[26] Mundy, J. et al. Atomically engineered ferroic layers yield a room temperature magnetoelectric multiferroic. Nature **537**, 523527 (2016)

[27] Yadav, A. K. et al. Observation of polar vortices in oxide superlattices. Nature **530**, 198201 (2016)

[28] A. R. Von Hippel, Dielectric Materials and Applications, MIT Press and John Wiley & Sons inc., (1954)

[29] A.K. Jonscher, Dielectric relaxation in solids, J. Phys. D. Appl. Phys. **32**, R57-R70 (1999)

[30] H. Schmid 1994 Ferroelectrics **161** 1 (1994)

[31] Narendra Babu, A. Siddeshwar, K. Srinivas, S. V. Suryanarayana, T. Bhimasankaram. Journal of Materials Sience August, Vol. 44, Issue 15, 3948-3951 (2009).

[32] W.H. Shepherd, Electrical Characteristics of Ferroelectric PZT Thin Films for DRAM Applications, IEEE Trans. Electron Devices. **39**, 2044-2049 (1992)

[33] I. Zutic, J. Fabian, S. Das Sarma, Spintronics: Fundamentals and applications, Rev. Mod. Phys. **76**, 323-410 (2004) .

[34] S.A. Wolf, D.D. Awschalom, R.A. Buhrman, J.M. Daughton, S. von Molnr, M.L. Roukes, A.Y. Chtchelkanova, D.M. Treger, Spintronics: a spin-based electronics vision for the future., Science. **294**, 148895 (2001)

[35] Rashba, E. I., Complex impedance of a spin injecting junction, Appl. Phys. Lett. **80**, 23292331 (2002)

[36] M. Oestreich, M. Brender, J. Hubner, D. H. W. W. Ruhle, T. H. P. J. Klar, W. Heimbrodt, M. Lampalzer, K. Voltz, and W. Stolz, Spin injection, spin transport and spin coherence, Semicond. Sci. Technol. **17**, 285297 (2002)

[37] R. Parsons, Band-to-band optical pumping in solids and polarized photoluminescence, Phys. Rev. Lett. **23**, 1152 1154 (1968)

[38] A. I. Ekimov, and V. I. Safarov, Optical orientation of carriers in interband transitions in semiconductors, Pisma Zh. Eksp. Teor. Fiz. 12, 293297 [JETP Lett. 12, 198201 (1970)]

[39] D. Z. Garbuzov, A. I. Ekimov, and V. I. Safarov, Measurement of the lifetime and of the spin-relaxation time of electrons in semiconductors by the optical-orientation method, Pisma Zh. Eksp. Teor. Fiz. 13,3640 [JETP Lett. 13,2426 (1971)]

[40] F.Meier, and B. P. Zakharchenya, Eds., Optical Orientation (North-Holland, New York)(1984)

[41] J. Grindlay,In An Introduction to the Phenomenological Theory of Ferroelectricity, **26** United Kingdom:Pergamon.(1970)

[42] M.E. Lines, A.M. Glass, Principles and Applications of Ferroelectrics and Related Materials. New York:Oxford university press. (1977)

[43] T. Mitsui, I. Tatsuzaki, E. Nakamura, An Introduction to the Physics of Ferroelectrics. **1** Gordon & Breach Science Pub. (1976)

[44] V.Y. Shur, Fast polarization reversal process: Evolution of ferroelectric domain structure in thin films. Ferroelectric Thin Films: Synthesis and Basic Properties **10** 153192 (1996)

[45] Y. Ishibashi, Y. Takagi, Note on ferroelectric domain switching. Journal of the Physical Society of Japan **31**(2), 506510 (1971)

[46] M. W. Hooker, Properties of PZT-Based Piezoelectric Ceramics Between -150 and 250C, NASA/CR-1998-208708 (1998)

[47] J. Meija, T.B. Coplen, M. Berglund, W.A. Brand, P. De Bièvre, M. Gröning, N.E. Holden, J. Irrgeher, R.D. Loss, T. Walczyk, T. Prohaska, Atomic weights of the elements (IUPAC Technical Report), Pure Appl. Chem. **88** 265291 (2016)

[48] R. M. Bozorth, Ferromagnetism, IEEE Press, New York (1951)

[49] Chikazumi, Sōshin. Physics of ferromagnetism. English edition prepared with the assistance of C.D. Graham, Jr (2nd ed.). Oxford: Oxford University Press. p. 118. (2009)

[50] Cullity, B.D.; Graham, C.D. "6. Ferrimagnetism". Introduction to Magnetic Materials. John Wiley & Sons. (2011)

[51] Y. Xu, Ferroelectric Materials and Their Applications. The Netherlands: Elsevier Science Publishers B.V. (1938)

[52] W. Känzig, Ferroelectrics and antiferroelectrics. In: Seitz, F., .T., Das, T.P.,

Turnbull, D., Hahn, E.L.(Eds.), Solid State Physics 4. Academic Press, p.5. ISBN 0126077045. (1957)

[53] M. Dawber, P. Chandra, P.B. Littlewood, J.F. Scott, Depolarization corrections to the coercive field in thin-film ferroelectrics. Journal of Physics: Condensed Matter **15** (24), 393 (2003)

[54] Datta, S., and B. Das, Electronic analog of the electro- optic modulator, Appl. Phys. Lett. **56**, 665667 (1990)

[55] D. Kivelson, P. Madden, Theory of dielectric relaxation, Molecular Physics: An International Journal at the Interface Between Chemistry and Physics, **30:6**, 1749-1780 (1975)

[56] D.A. Pan, Y. Bai, W.Y. Chu, L.J. Qiao, Ni-PZT-Ni trilayered magnetoelectric composites synthesized by electro-deposition, J. Phys. Condens. Matter. **20** , 0-4 (2008)

[57] V.M. Laletin, N. Paddubnaya, G. Srinivasan, C.P. De Vreugd, M.I. Bichurin, V.M. Petrov, D.A. Filippov, Frequency and field dependence of magnetoelectric interactions in layered ferromagnetic transition metal-piezoelectric lead zirconate titanate, Appl. Phys. Lett. **87**, 1-3 (2005)

[58] K. M. Luk and K. W. Leung, Eds., Dielectric Resonant Antenna, Research Studies Press, (2003)

[59] M. Simeoni, R. Cicchetti, A. Yarovoy, and D. Caratelli, Plasticbased supershaped dielectric resonator antennas for wide-band applications, IEEE Transactions on Antennas and Propagation, vol. 59, no. 12, pp. 48204825, (2011)

[60] M. Simeoni, R. Cicchetti, A. Yarovoy, and D. Caratelli, Supershaped dielectric resonator antennas, in Proceedings of the IEEE Antennas and Propagation Society International Symposium, pp.14, June (2009)

[61] J.-I. Moon and S.-O. Park, Dielectric resonator antenna for dual-band PCS/IMT-2000, Electronics Letters, vol. 36, no. 12, pp. 10021003, (2000)

[62] Green, Estill I. (October 1955). "The Story of Q". American Scientist. 43: 584594.

[63] B. Jeffreys, Q.Jl R. astr. Soc. (1985) 26, 5152

[64] Paschotta, Rdiger. Encyclopedia of Laser Physics and Technology, Vol. 1: A-M. Wiley-VCH. p. 580. (2008)

[65] G. Nader, E.C.N. Silva, J. Adamowski. Effective Damping Value of Piezoelectric Transducer Determined by Experimental Techniques and Numerical Analysis. 1. (2004)

Chapter 2

Experimental Techniques

In this present chapter, the experimental techniques are summarized along with the technical discussions on the experimental setups, issues, and concerns in different growth and characterization techniques. Even though several growth techniques are available to grow the ferromagnetic/ferroelectric/ferromagnetic ($F_M/F_E/F_M$) capacitors, sputtering for the ferromagnetic contacts was used since it's the simplest and most widely used method. Solid state reaction for the synthesis of $Pb[Zr_xTi_{1-x}]O_3$, with spray pyrolysis (SPL) for the deposition was used as an economic and interesting growth alternative. The current project has a focus on the understanding of the interactions of the magnetic and ferroelectric coupling between lead zirconate titanate and three selected ferromagnetic elements: iron, cobalt, and nickel.

There were two sets of lead zirconate titanate (PZT) samples, the first substrates were commercial-ready products that had predetermined sizes and thicknesses, the second were samples that were made by Spray Pyrolysis onto Ni and Co/Fe sputtered Cu laminate substrates. The first set of PZT samples were of two dimensions, first of h_{PZT}=1.00 cm, w_{PZT}=1.00 cm, and d_{PZT}=1.00 mm and second was of h_{PZT}=3.00 mm, w_{PZT}=1.00 cm, and d_{PZT}=200 μm. The third set were of Ni and Cu laminate sheet cut to h_{PZT}=1.00 cm and w_{PZT}=1.00 cm; onto this PZT was deposited via Spray Pyrolysis with an outcome thickness between d_{PZT}=1.4 μm up to 7 μm. The PZT used during SPL was synthesized by solid-state reaction technique, and with XRD measurements determined if the material had the correct crystallographic structure. The most important information is

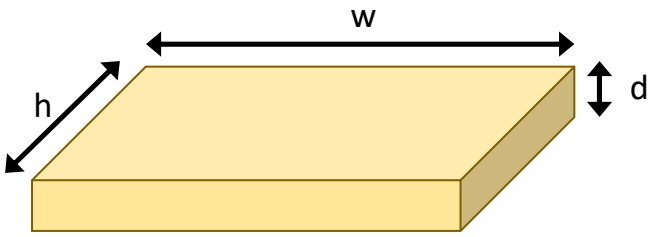

Figure 2.1: Diagram dimensions of the PZT substrate (or film) and the specified label with the thickness being 'd', and the area of the sample being 'h' x 'w'.

the thickness of the PZT samples, during the experimentation the sets were divided, measured and compared because of their thicknesses. The ferromagnetic materials that were sputtered onto the samples were iron, cobalt and nickel, with Silver working as reference for a non-ferromagnet and simple capacitor. All the processes involved during the deposition of materials and measurements of the finished sample are going to be finely detailed in this chapter where we talk about the physics and the history behind each process.

Capacitors are the basis to most, if not all, electronics. It is a simple structure that by minimum structural changes we can obtain many devices with different utilities. The basic shape of a capacitor, as shown in Figure 2.20, is a great starting point to obtain and measure the properties of a desired material and its coupling interaction with the charge plates.

Thin film transistors (TFT) are a special type of metal-oxide-semiconductor field-effect transistors (MOSFET) and organic field-effect transistors (OFET) that are made by depositing thin films of a semiconductor layer, a dielectric insulating layer and metallic contacts over a non conductive substrate. This structure has a similarity to that of a capacitor but more complex. Transistors are an integral part of electronics, for example, the best known application of TFTs are in LCDs. Where transistors are embedded within the panel itself. This

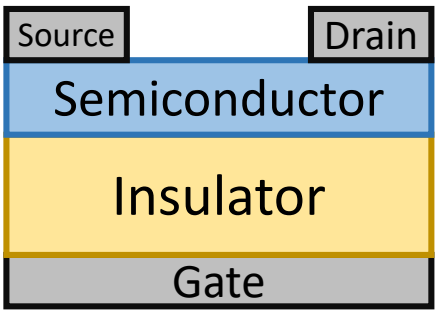

Figure 2.2: Schematic of the thin film transistor used in organic effect transistors.

reduces the crosstalk between pixels and improves image stability. As shown in Figure 2.2, the structure is of a complex capacitor, where it includes a bottom contact layer, known as "gate", and two separate top contact layers known as "source" and "drain". With this, the capacitor structure is the best to measure and characterize materials, either for the insulating layer, the metallic contacts, and their coupling interaction. Furthermore, adding one more layer of information, beside charge carrier, the metallic contact plates can be of a magnetic material, or one that is affected by the presence of a magnetic field. This can further the utility and the affecting inputs of the desired end product.

2.1 Growth Techniques

2.1.1 Solid-State Reaction Technique

PZT is a widely studied material and has different ways to synthesize. One of the most common is by solid-state reaction method. This process is characterized that the beginning and end products are solid materials, specifically powders.

Lead zirconate titanate has a general stoichiometric formula as: $Pb[Zr_xTi_{1-x}]O_3$, where 'x' can be adjusted for a specific concentration. The best

concentration studied with high piezoelectric effect used is: $Pb_{1.2}Zr_{0.52}Ti_{0.48}O_3$. This is also known as Navy Type II (PZT-5A), since it was made by the US Navy.

Table 2.1: Important physical and structural properties of Lead (II) Oxide, Zirconium (IV) Oxide, and Titanium (IV) Oxide [1–6].

Material	Lead (II) Oxide	Zirconium (IV) Oxide	Titanium (IV) Oxide
Chemical Formula	PbO	ZrO_2	TiO_2
Molar Mass	223.2 g/mol	123.22 g/mol	79.87 g/mol
Physical State at 20° C	Solid	Solid	Solid
Density	9.53 g/cm^3	5.68 g/cm^3	4.23 g/cm^3
Melting Point	1161 K (888° C)	2988 K (2715° C)	2116 K (1843° C)
Boiling Point	1750 K (1477° C)	4570 K (4300° C)	3245 K (2972° C)
Appareance	red or yellow powder	white powder	white powder
Crystal Structure	Tetragonal, tP4	Monoclinic	Tetragonal
Purity	99.9%	99.7%	99.9%

The total end quantity of PZT desired was 20 grams, with this we needed to synthesize PZT from its precursors individually. The precursors required where Lead (II) Oxide (PbO), Zirconium (IV) Oxide (ZrO_2), and Titanium (IV) Oxide (TiO_2).

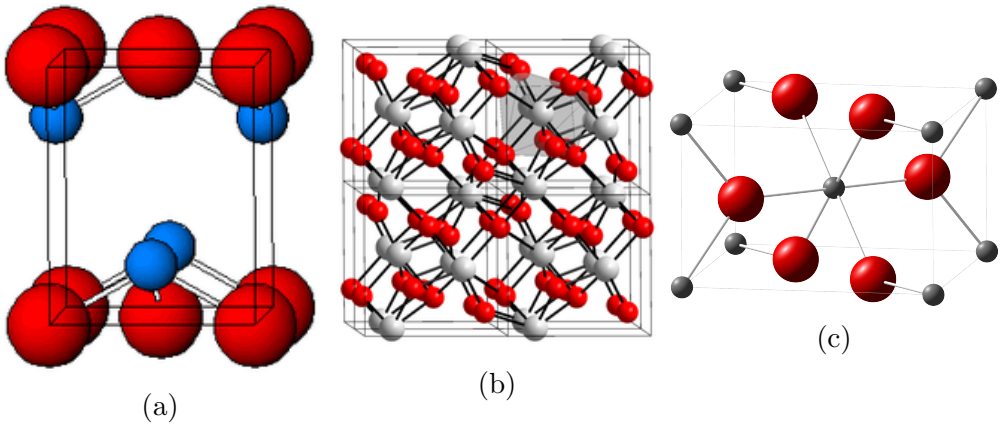

(a) (b) (c)

Figure 2.3: Crystal structure diagram of (a) PbO, (b) ZrO_2, and (c) TiO_2.

PbO, known as well as lead monoxide, is an inorganic compound that occur naturally as two types of polymorphs: litharge and massicot. Litharge has a

tetragonal crystal structure, while massicot has an orthorhombic crystal structure. Both polymorph structures share a pyramidal four-coordinate lead center. As a tetragonal, the four leadoxygen bonds have the same length, whereas in the orthorhombic two are shorter that the other. PbO usually has a coloration between yellow to red, depending on its crystalline structure [1, 2]. Important physical and structural properties of these precursors are listed in Table 2.1 with their crystalline structure diagrams in Figure 2.3.

ZrO_2 is also known as zirconia, is a white crystalline oxide that occurs naturally from monoclinic mineral baddeleyite. Three phases of TiO_2 are known depending on the temperature. Monoclinic is present below 1170° C, tetragonal between 1170° C and 2370° C, and cubic when is above 2370° C. Compared to TiO_2, which has six-coordinated titanium in all phases, ZrO_2 as monoclinic consists of seven-coordinated zirconium centers, where the difference is due to the larger size of the zirconium atom relative to the titanium atom [3, 4].

TiO_2 is a naturally occurring mineral extracted from rutile, anatase, and two high pressure forms known as akaogiite, and brookite. These last two are the main ore source of TiO_2 in the world, followed by rutile [5, 6].

The balanced chemical formula for PZT is then: $Pb^{+2}_{1.2}Zr^{+4}_{0.52}Ti^{+4}_{0.48}O^{-2}_{3}$. Since Lead is a volatile compound at high temperatures and tends to evaporate, adding extra PbO compensates this problem, and that is why there is a higher percentage of Pb to start with. With the purity of the material in mind, the starting mass of materials required is:

$$\frac{1.2PbO}{PZT} * 20g * \frac{100\%}{X} = 14.4823g \tag{2.1}$$

$$\frac{0.52ZrO_2}{PZT} * 20g * \frac{100\%}{X} = 3.4715g \tag{2.2}$$

Figure 2.4: PZT powder on agate mortar and pestle.

$$\frac{0.48TiO_2}{PZT} * 20g * \frac{100\%}{X} = 2.07294g \tag{2.3}$$

with "PZT" the total amount of the end product of lead zirconate titanate (20 grams) and 'X' being the purity percentage of the material. The powder where then put on the furnace to calcinate at 850° C for 10 hours. When the powders are done the calcination process, the now solid mix is ground and put on agate milling jars with isopropanol for approximately 12 hours with pauses every hour and change in rotation. The milled powder is then dried and ground on a agate mortar/pestle, as shown in Figure 2.4. Then the powder is sieved on a 45 μm mesh, to have it a fine as possible. This fine powder is then done a XRD measurement to determine that the correct phase is achieved. The first XRD performed is shown in Figure 2.5a. Since there is a presence of a peak for the pyrochlore phase (at 29 degrees) too high, the sample had to be milled, calcined, ground, and sieved again with the difference that the calcination process

was done at 875° C This is taken again to the XRD for another read. The difference between the pyrochlore and the perovskite peak was determined to be within limits, as shown in Figure 2.5b. In section 2.2.1, X-Ray Diffraction as a characterization method is further explained.

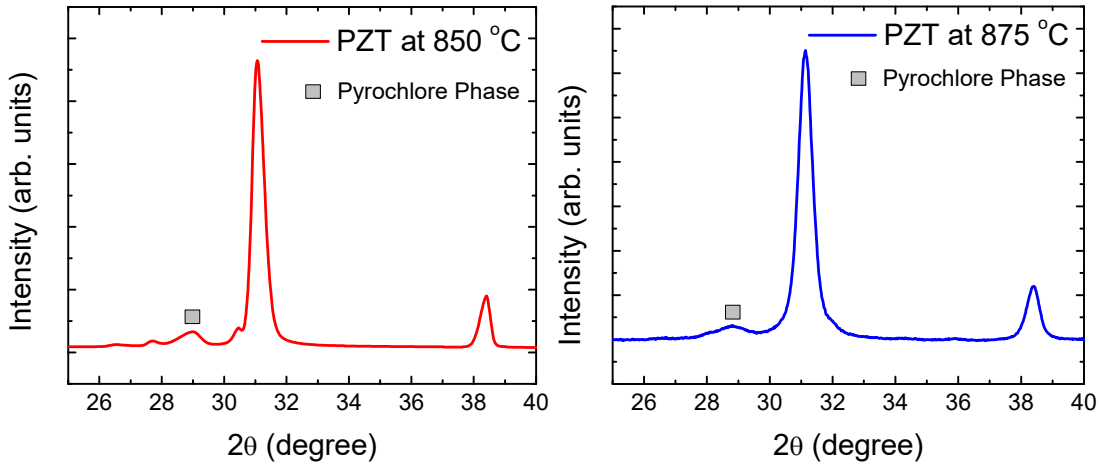

Figure 2.5: XRD measurements of PZT calcined at (a) 850° C and (b) 875° C where the pyrochlore phase is shown at 29 degrees.

2.1.2 Thin Film Growth by Sputtering

There is a high demand for the deposition of thin films, their composition, and utility. The two main deposition techniques that are widely available are: physical deposition and chemical deposition. Both techniques have their respective advantages depending on the deposited material desired and the end product. Sputtering is a physical deposition technique where material of a specific target can be deposited on a desired substrate. This process involves microscopic particles that are ejected from the surface after it is bombarded by energized particles of a plasma or gas. There are two ways to run Sputtering voltage sources, which are Direct Current (DC) and Radio Frequency (RF) Sputtering. DC Sputtering is one of the simplest sputtering processes and it involves a high potential bias

between two electrodes, where one of them contains the target and the other the substrate in a ionized gas chamber. RF Sputtering implements the same architecture as DC with the added alternating of the electrical potential source within the system at radio frequencies, this helps to avoid a charge buildup on certain types of target materials, which can create arcs by the plasma that make droplets of material which creates issues in quality control on the thin films. The implementation of the RF system can avoid the complete stop of the sputtering of atoms which terminates the deposition process [7].

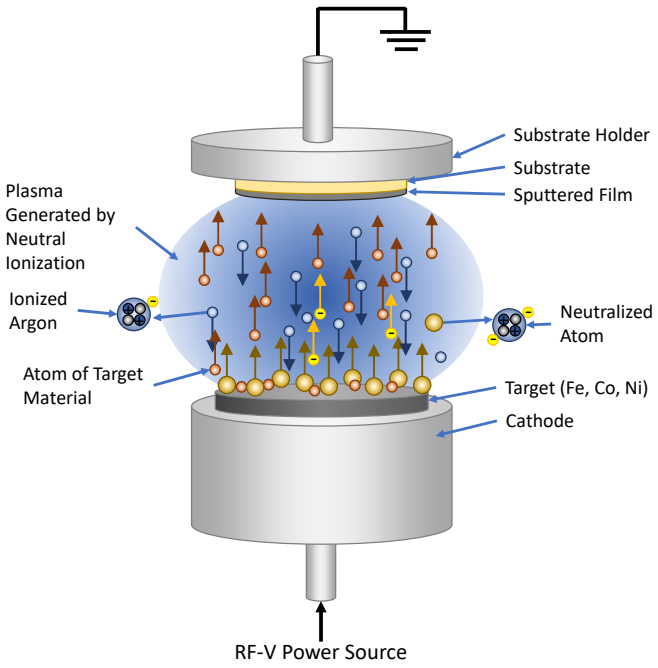

Figure 2.6: Diagram of the RF sputtering deposition process.

DC Sputtering, as the most traditional of the two, is a very cost-effective method of applying metallic coatings upon the desired substrates, which are electrical conductors, one of the most commonly used is gold. On the other hand, DC Sputtering has a limitation with dielectric target materials, which are non-conducting insulating materials that can be polarized by an applied field. Some

of the common dielectric coating materials used in the semiconductor industry include Aluminum Oxide, Silicon Oxide and Tantalum Oxide. This system works as well with ferromagnetic target materials.

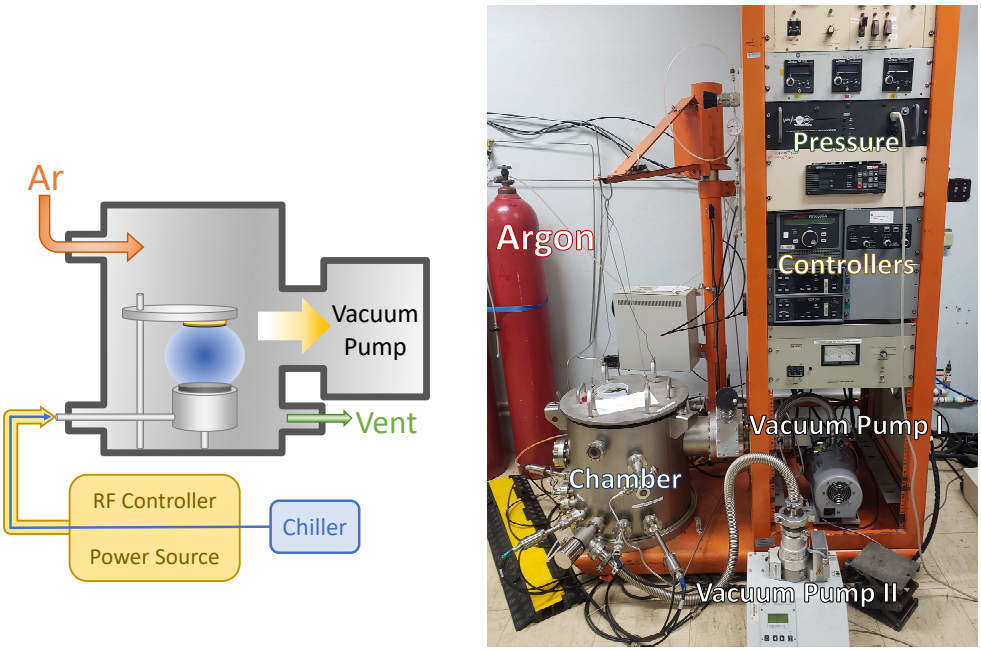

(a) (b)

Figure 2.7: (a) Diagram of the sputtering system and its components (b) Sputtering system at Device Physics laboratory of UPR.

Similarly to DC Sputtering, the RF Sputtering system runs an energetic wave through an inert gas, in this case Argon, within a vacuum chamber; this ionizes the gas. The target material or cathode which is to become the thin film coating is bombarded by these high energy ions of Argon where they are directed towards the target, which hits the atoms and sputter these off as a very fine spray that covers the substrate coating it in the process. If there is a mask between the target and substrate, the coating that has been deposited on the substrate will take the shape of this mask and coat in desired shapes. RF Magnetron sputtering uses magnets behind the negative cathode to trap electrons

over the negatively charged target material, so they are not free to bombard the substrate, allowing for faster deposition rates. Figure 2.6 shows a diagram of how this process occurs as well as the full diagram of the sputtering system available at Device Physics laboratory of University of Puerto Rico, PR USA shown in Figure 2.7. The system is composed by a turbo pump as main vacuum system, and for deposition process vacuum a smaller turbo pump is utilized (Names needed). The RF controllers are from Advanced Energy with the RFX600A and Tunner, as shown in Figure 2.9. Figure 2.8a shows the plasma as seen from the viewport of the In-House Sputtering system as deposition is happening as well as the inside of the sputtering chamber and its components in Figure 2.8b.

If DC sputtering was used with these materials, over time, the positive ions produced that will accumulate on the surface of the target face will give it a positive charge at the surface. This build up will reach a point where the charge can lead to a complete secession of sputtering atoms being discharged for coating and thus terminates the sputtering process. With the addition of the alternating electrical potential by RF Sputtering, the surface of the target material can be cleaned of this charge buildup with each cycle. On the positive cycle electrons are attracted to the target material or cathode giving it a negative bias. On the negative portion of the cycle - which is occurring at the radio frequency of 13.56 MHz used internationally for RF power supply equipment - ion bombardment of the target to be sputtered continues [8].

In this sense, RF Sputtering offers several advantages over DC Sputtering depending upon the specific application, target, and substrates. With RF Sputtering, the plasmas tend to defuse throughout the entire chamber, unlike concentrating around the cathode or target material as with DC Sputtering. On the other hand, RF Sputtering can sustain a plasma throughout the chamber at

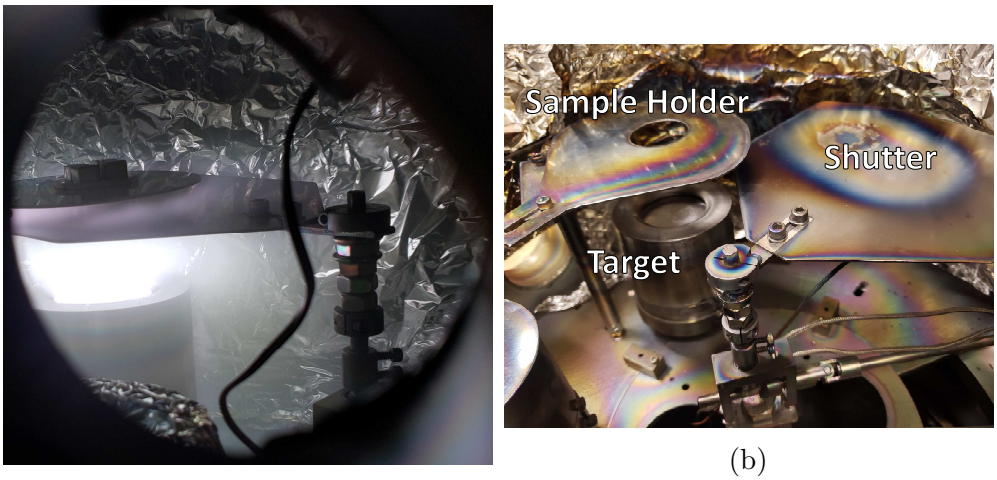

(a) (b)

Figure 2.8: Pictures of (a) Plasma made by RF Sputtering during deposition and (b) inside of the sputtering system.

lower pressures (1-15 mTorr). The result is having fewer ionized gas collisions, this equals to waving a more efficient line-of-site deposition of the coating material. In Figure 2.10 two samples with deposited material are shown, with (a) being cobalt (Co) deposited on a 10 cm X 10 cm X 1 mm PZT substrate and (b) is nickel (Ni) deposited on a Spray Pyrolysed PZT on a nickel laminate. The target to substrate distance was 56 mm.

For the purpose of this project, the settings of deposition for the sputtering are presented in Table 2.2.

2.1.3 Spray Pyrolysis

Today in modern technology, there is a huge widespread of applications that require the presence of thin films. The methods utilized for the deposition of thin films, as stated before, can be divided into two groups: physical or chemical deposition. And further on, chemical deposition techniques can be divided further in two, gas phase and liquid phase. Spray pyrolysis (SPS) falls as a liquid

Figure 2.9: Sputtering system pressure gauges and controllers.

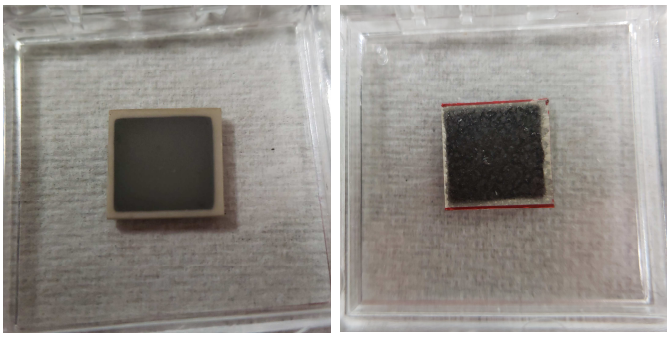

(a) (b)

Figure 2.10: Pictures of (a) RF Sputtered cobalt on 10cm X 10cm X 1mm PZT substrate and (b) nickel sputtered on nickel laminate/PZT SPL deposited substrate.

Table 2.2: Deposition parameters for the three ferromagnetic contacts (Fe, Co, Ni) by RF sputtering.

Material	Iron (Fe)	Cobalt (Co)	Nickel (Ni)
Target Purity	99.9%	99.95%	99.995%
Target Dimensions	2"x0.250"	2"x0.125"	2"x0.250"
Deposition Pressure With Ar	6.0 x 10^{-2}	6.0 x 10^{-2}	6.0 x 10^{-2}
Plasma Power	180W	200W	200W
Deposition Time	2hrs	2hrs	1hr 30min

phase chemical deposition technique. SPL is a deposition process that has high consideration in research to prepare thin and thick films, ceramic coatings, and powders. What differentiates SPL from other film deposition techniques is that spray pyrolysis is a very simple and relatively cost-effective deposition method, considering the cost of equipment and materials. It is a very simple technique for the application in film deposition and doesn't require high-quality substrates or chemicals which lowers the cost significantly. SPL has been used for the deposition of dense films, porous films, and for powder production as even multilayered films can be easily deposited. Spray pyrolysis has been used for several decades in the glass industry and in solar cell production [9, 10].

SPL technique was first introduced in 1966 by Chamberlin and Skarman and was for the growth of cadmium sulfide (CdS) for solar cell applications [11]. Since then, various reviews concerning the use of spray pyrolysis techniques have been published. Tomar and Garcia have discussed the preparation and the properties of sprayed films as well as their application in solar cells, antireflection coatings, and gas sensors [12]. Albin and Risbud presented a review of the equipment, processing parameters, and optoelectronic materials deposited by the spray pyrolysis technique [13]. Pamplin has published a review of spraying solar cell materials as well as a bibliography of references on the spray pyrolysis

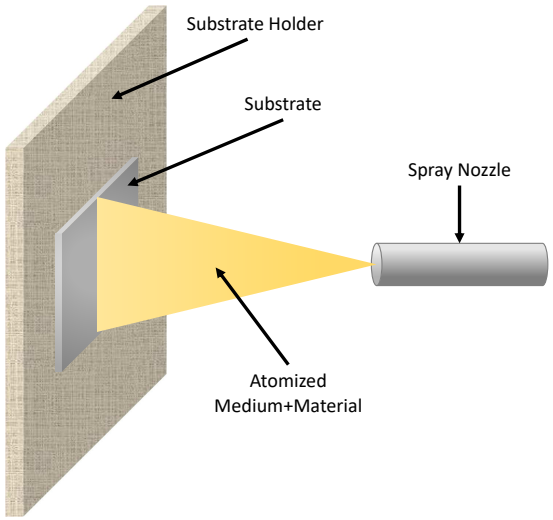

Figure 2.11: Schematic of Spray Pyrolysis deposition process.

technique [14]. Recently, thin metal oxide and chalcogenide films deposited by spray pyrolysis and different atomization techniques were reviewed by Patil [15]. Bohac and Gauckler have discussed the mechanism of chemical spray deposition and presented some examples of sprayed Yttria-stabilized zirconia (YSZ) films [16].

SPL deposition technique is encompassed by simple steps:

1. Atomization of the precursor solution

2. Spreading on the substrate

3. Drying and decomposition of the precursor medium

With this, you have left the desired material deposited on your substrate. This is the main reason to why SPL is very interesting in terms of cost and time efficiency. In Figure 2.11 it is shown the basic composition of the deposition by SPL.

Figure 2.12: Nickel laminate of 0.05 mm thick.

2.1.3.1 Substrate Preparation

The three ferromagnetic materials used in this project, as stated before, are iron, cobalt, and nickel. For the SPL process we need substrates to grow our PZT material. A nickel laminate was obtained commercially, it had a thickness of 0.05 mm and is shown in Figure 2.12. For iron and cobalt, the laminates were not available, and an alternate process was derived. Using a copper laminate as substrate and contact, followed by a sputtering of the desired ferromagnetic material, we obtain the shape of previous samples. This structure is shown in Figure 2.13a. The substrate laminates (Cu and Ni) must be thoroughly cleaned by etching and degreasing agents, so the surface is clean, not oxidized, and with no moisture or grease. This helps the sputtered material to adhere properly. After the substrates are ready, where the nickel laminate is clean, and the Cu laminate has the desired ferromagnet sputtered on, we can follow to the deposi-

tion of PZT by Spray Pyrolysis on top of this substrates.

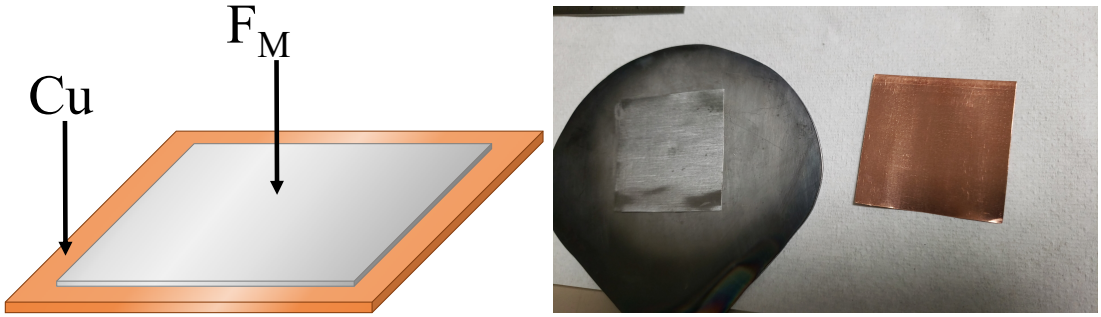

(a) (b)

Figure 2.13: (a) Structure of ferromagnetic material sputtered on a copper laminate substrate and (b) (Left) iron deposited on (Right) copper substrate before deposition.

2.1.3.2 Deposition process by spray

To make the paint required to deposit PZT onto our substrate, we need a binder that will carry the PZT particles along a liquid to be sprayed. The medium used to bind the PZT powder is Polyvinylpyrrolidone (PVP). PVP is a water soluble polymer made from N-vinylpyrrolidone monomers. This polymer

Figure 2.14: Polyvinylpyrrolidone (PVP) powder.

is soluble on isopropanol, which it is utilized in the making of the paint, which degrades and evaporates at fairly low temperatures ($> 100°$ C). The paint will consist of three ingredients: PZT (our material), PVP (the medium), and isopropanol (solvent). The ratio of PVP per solvent is of about 5%. Since PVP has a density of 1.2 g/cm^3, for 30 ml of total paint, we utilize 1.8 g of PVP diluted on isopropanol. To this base we add the PZT powder that has been finely ground and sieved on a 45 μm mesh. The mixture is then put on a magnetic mixer, so the PZT is distributed evenly. We need to have in mind that the isopropanol evaporates rapidly and that the PZT/PVP emulsion can separate itself rapidly as well. The paint is transferred to an air brush (see Figure 2.15a) that has a fine distributing nozzle tip. The air brush is preset to the desired air pressure, mixture opening, and spray rate beforehand to be consistent with every spray pass. Depending on the thickness desired, the number of passes are determined with a delay between passes to let the sprayed material to dry. Figure 2.15b shows an image of the airbrush depositing PZT paint on to the substrate. A heat gun can be used to fasten the drying process. Two samples were made of different thicknesses done by spraying longer on a "thicker" sample. Once the desired thickness is achieved the sample is left to fully dry. This can be done by letting it to dry in ambient or by furnace (or hot plate) at low temperatures ($\approx 150°$ C). After the paint has fully cured, some profilometer measurements are done to determine the thickness of the layer. Followed by this, the samples can be cut to a desired shape, in our case it was cut to 10 cm x 10 cm so that it can fit in the Sputtering's sample holder. The sputtering sample holder can carry up to 4 samples (another holder can carry up to 2 samples). Later the top ferromagnetic contact layer is sputtered on top of the deposited PZT. With this we obtain the desired structure of F_M/PZT/F_M spin capacitor to be studied.

The end product can be observed in Figure 2.10b in Chapter 2.1.2. This sample is now ready to be subjected to dielectric measurements as done the same with previous samples.

(a) (b)

Figure 2.15: (a) Air brush system utilized to spray the PZT paint onto substrates (b) Deposition of PZT by SPL on to a ferromagnetic material sputtered on copper.

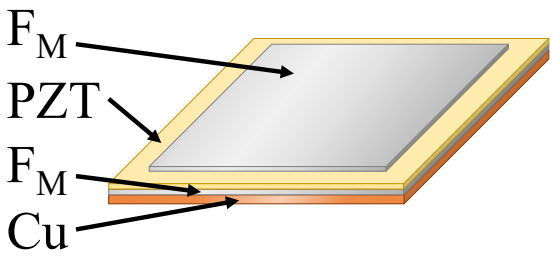

Figure 2.16: Full structure of finished sample with copper as substrate/contact, ferromagnetic material sputtered, PZT layer applied by SPL, and top ferromagnetic material sputtered.

2.2 Characterization Techniques

2.2.1 X-Ray Diffraction

X-Ray Diffraction (XRD) is an important analytical technique primarily used for phase identification of a crystalline material. This technique provides information about crystal structure, lattice parameter, orientation of the thin films and strain and particle size of the crystalline structures. There are two processes that occurs when the X-ray beam hits an atom, the first is that the beam is absorbed and ejects an electron from the atom, of the beam can be scattered. The primary beam utilized is generated by a cathode ray tube with a heated filament which produces electrons, then these are accelerated toward a target by an applied potential difference and bombarding the target material with electrons. This beam is an electromagnetic wave with an electric vector that varies sinusoidally with time and perpendicular to the propagation of the beam itself. The electric field applies a force on the electrons of the atom which produces an acceleration of the electrons, this makes a radiation. This radiation spreads in all directions from the atom, it has the same frequency as the primary beam, and it is referred as the scattering radiation.

From theoretical and experimental research, it is known that there are two kinds of scattering; unmodified scattering (which has same wavelength) and modified scattering known as Compton (with a longer wavelength). Using a crystal as example, this gives an unmodified scattering. The unmodified scattering from an atom can be calculated with first considering that each electron a spread out diffused cloud of negative charge with a density ρ. The ratio of charge in a volume dV to the charge of one electron is ρ dV. Now for each electron is:

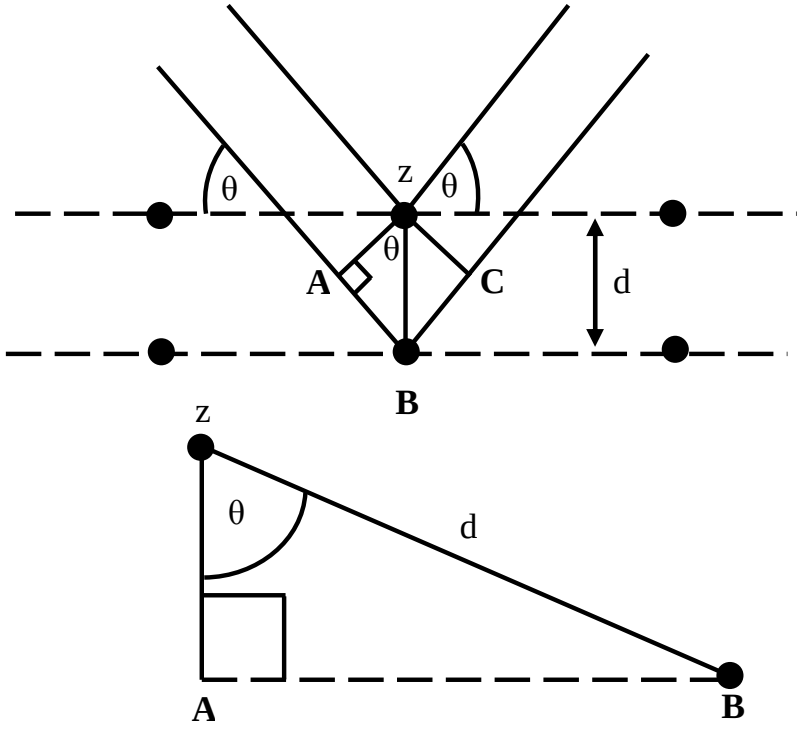

Figure 2.17: Schematic of X-ray diffraction by a solid.

$$\int \rho dV = 1. \tag{2.4}$$

To obtain the total amplitude of the unmodified scattering for one electron, we must integrate over the whole volume that the electron occupies, doing this we make proper allowance for the phase of the contribution from each element of ρ dV. Followed, we have the quantity represented by the integral f_e as the scattering factor.

$$f_e = \int e^{(2\pi \mathrm{i}/\lambda)(\mathrm{s}-\mathrm{s}_0)^{\mathrm{r}}} \rho dV. \tag{2.5}$$

As can be seen, f_e is the ratio of the amplitude from one electron with unmodified scattering to the amplitude scattered by an electron according to the classical theory. In other words, f_e is the amplitude of unmodified scattering per electron and it is expressed in units of electron. Even though we know that the charge distribution for each electron in the atom is spherical, but for closed groups of inner electrons, spherical symmetry exists, and with this we can work with the combined charge distribution for the electron of a closed group.

The most important principle in X-ray diffraction is the Bragg's law. Bragg's diffraction occurs when electromagnetic radiation or subatomic particle waves with wavelength comparable to the atomic spacings, are incident upon a crystalline sample, scattered by the atoms in the system and undergo constructive interference in accordance with Bragg's law.

To consider the necessary conditions for Bragg's law, we must assume that the phases of the beams coincide when the incident angle equals and reflecting angle (cf. Figure 4.1) The rays of the incident beam are always in phase and parallel up to the point at which the top beam strikes the top layer at atom z. The second beam continues to the next layer where it is scattered by atom B. The second beam must travel the extra distance AB + BC if the two beams are to continue travelling adjacent and parallel. This extra distance must be an integral (n) multiple of the wavelength (λ) for the phases of the two beams to be the same:

$$n\lambda = AB + BC. \tag{2.6}$$

As we recognize that d is the hypotenuse of the right triangle AB_z, we can

use trigonometry to relate d and θ to the distance (AB + BC). The distance AB is opposite θ so we have:

$$AB = d \sin\theta. \tag{2.7}$$

And because AB=BC then we have that equation 2.7 becomes:

$$n\lambda = 2AB. \tag{2.8}$$

Then, substituting the equation 2.7 in equation 2.8 we have:

$$n\lambda = 2d \ \sin\theta \tag{2.9}$$

This is known as Bragg's law, and which can be used to understand the diffraction pattern. Since this example only uses two rows of atoms, the transition from constructive to destructive interference as θ changes is gradual. However, if interference from many rows occurs, then the constructive interference peaks become very sharp with mostly destructive interference in between. This sharpening of the peaks as the number of rows increases is very similar to the sharpening of the diffraction peaks from a diffraction grating as the number of slits increases. With this, a diffraction pattern is obtained from the measurements of the intensity of scattered waves as a function of the scattering angle. The very strong intensities that are seen are known as Bragg peaks and these are obtained in the diffraction pattern when scattered waves satisfy the Bragg's law [38].

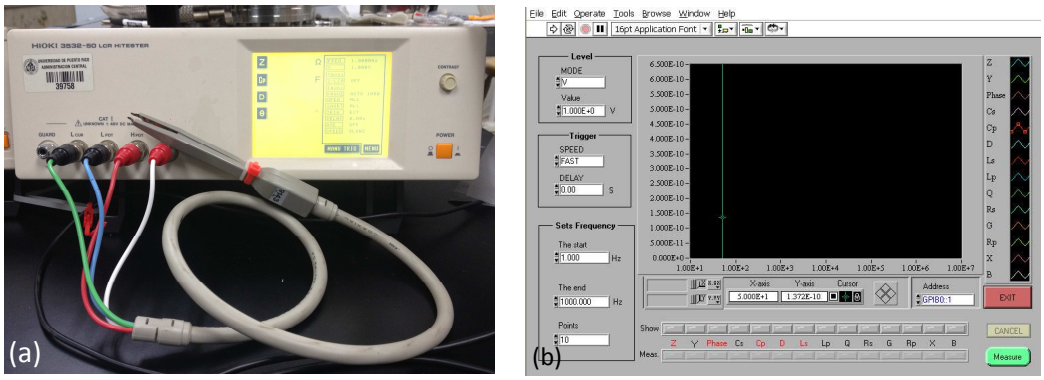

Figure 2.18: (a) HIOKI LCR meter (b) LABVIEW program used for electric and dielectric measurements.

2.2.2 Dielectric Measurements

The samples were measured using the HIOKI 3532-50 LCR HiTESTER from the HIOKI E.E. Corporation with tweezers probe as shown in Figure 2.18. The HIOKI 3532-50 LCR HiTESTER is an impedance meter which uses a touch panel as a user interface and has PC connectivity through GP-IB. The equipment has a frequency range of 42 Hz up to 5 MHz at high resolution. The resolution is three-digits for not more than 100 Hz, and four-digit resolution for not more than 5 MHz. It has a test frequency accuracy of $\pm$ 0.005% or less. The values measured were capacitance, impedance (with real and imaginary parts divided), dielectric loss, and phase angle. It performs all the measurements simultaneously. The sample were mounted on the tweezers, as shown in the diagram of Figure 2.19a and as well subjected to magnetic fields [17].

The dielectric permittivity measurements were obtained from the capacitance measurement. As we know, the HIOKI 3532-50 LCR HiTESTER measures overall capacitance of the sample, where we want to obtain the dielectric permittivity of the sample. For this we have to use the relation with Equation 2.10

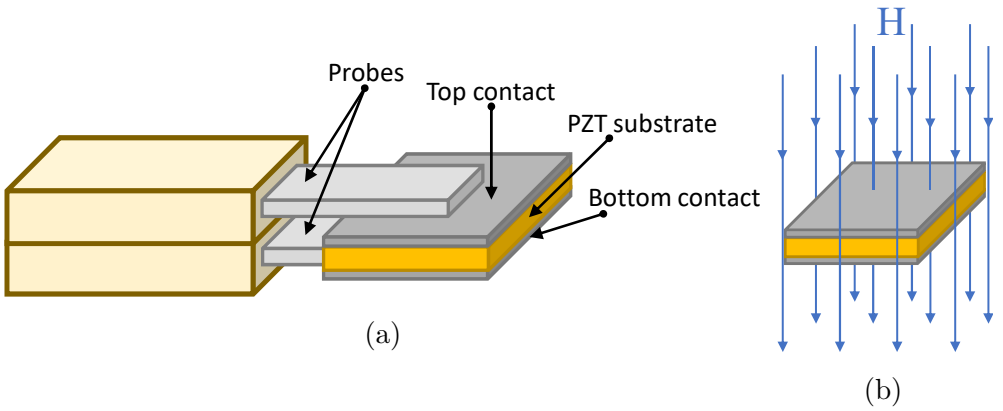

Figure 2.19: (a) Schematic of dielectric measurement using parallel plate capacitor configurations and (b) the capacitor inside an applied magnetic field.

and solving for κ' we have:

$$\kappa' = \frac{C}{C_0} \tag{2.10}$$

Considering that the capacitance of a capacitor with an area 'A' and a plate separation of 'd', with the separation being vacuum, we have:

$$C_0 = \frac{\epsilon_0 A}{d} \tag{2.11}$$

Inserting Equation 2.11 into Equation 2.10, we have the dielectric permittivity of the material with respect of the measured capacitance 'C', the area 'A', and space between plates 'd' obtaining:

$$\kappa' = C\frac{d}{\epsilon_0 A} \tag{2.12}$$

These are all obtainable values, with the dielectric constant of vacuum being ϵ_0=8.854×10^{-12} F/m, the capacitance is obtained from the HIOKI 3532-50 LCR HiTESTER capacitance output, the distance between plates is obtained from the sample size values and the area obtained by measuring the sputtered area on the

sample.

Dielectric materials have been studied extensively because of their applications in electronic devices, data, and energy storage. Some of the applications for which dielectric materials are being studied and utilized include: dielectric resonators, protective industrial coatings, cooling, and insulator for capacitors and other materials [18]. The most basic shape of a capacitor is two metal plates divided by either space (air or vacuum), or a non-conductive insulating material; as shown in Figure 2.20. This insulating material can be such as paper or plastic between the plates. Such material, called a dielectric, can be used to maintain a physical separation of the plates. There are two types of dielectrics. The first type is polar dielectrics, which are dielectrics that have permanent electric dipole moments. The orientation of polar molecules is random in the absence of an external field. When an external electric field $\mathbf{E_0}$ is present, a torque is set up and causes the molecules to align with $\mathbf{E_0}$. However, the alignment is not complete due to random thermal motion. The aligned molecules then generate an electric field that is opposite to the applied field but smaller in magnitude. The second type of dielectrics is the non-polar dielectrics, which are dielectrics that do not possess permanent electric dipole moment. Electric dipole moments can be induced by placing the materials in an externally applied electric field.

There are certain properties for a dielectric material within a capacitor which are of interest to determine the compatibility of the dielectric for certain applications and its value for it as a viable solution to certain utilities within those applications. The properties that where specially measured and studied in detail where basic frequency dependent measurements for dielectrics in capacitors, such as: dielectric permittivity, phase angle, impedance, and loss coefficient ($\tan(\delta)$). Each property will be discussed further in this chapter and the importance of

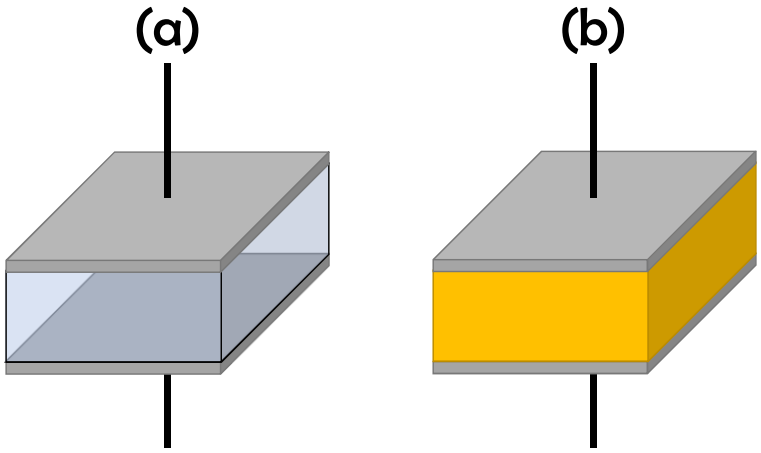

Figure 2.20: Basic capacitor structure with (a) free space between plates and (b) a dielectric material between plates.

their behavior with frequency dependency.

2.2.2.1 Dielectric Permittivity

The definition for dielectric constant relates to the permittivity of the material itself. The symbol commonly use is the Greek letter ϵ, with ϵ_0 being the dielectric permittivity constant in vacuum, which has a value of $8.854\text{x}10^{-12}$ F/m. This is the lowest value possible. The permittivity tells us how the polarization of a material responds when a field it's applied. The dielectric permittivity corresponds to the ratio of the permittivity of the dielectric material to that of the permittivity of vacuum. This means that the greater the polarization that the material can achieve with in an applied field of a certain magnitude, then greater the dielectric constant will be. Which means that greater the dielectric permittivity of the material will give us a better ability to store energy inside the capacitor, in other words, better capacitance [19]. Analyzing a simple capacitor that is connected to a sinusoidal voltage source (AC source) we have:

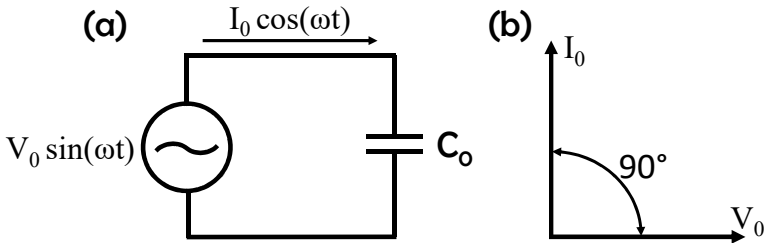

Figure 2.21: The current-voltage relationship of an ideal capacitor.

$$\mathbf{V} = \mathbf{V}_0 e^{j\omega t} \tag{2.13}$$

Having an angular frequency of $\omega = 2\pi\nu$, when the capacitor has a vacuum as the separation between the plates [Figure 2.20(a)], then it will store a charge $Q = C_0\mathbf{V}$, and draw a charging current as:

$$I_c = \frac{dQ}{dt} = j\omega C_0 \mathbf{V} \tag{2.14}$$

This current, to be a true capacitor, leads the voltage by a temporal phase of 90°. In Figure 2.21 we can visualize this as vectors. C_0 is the capacitance in vacuum of the capacitor. When the capacitor has a material, other than vacuum, then the capacitance increases to:

$$C = C_0 \frac{\epsilon'}{\epsilon_0} = C_0 \kappa' \tag{2.15}$$

Here we designate ϵ' as the real dielectric permittivity or dielectric constant of the dielectric and ϵ_0 of vacuum. Their ratio is κ', which is the relative dielectric constant of the material. Utilizing the relative permittivity $\epsilon^* = \epsilon' - j\epsilon''$, we can calculate the electric modulus, where we have [20]:

$$M^* = M' + jM'' = \frac{1}{\epsilon^*} \tag{2.16}$$

With this we simplify the modulus in terms of the dielectric permittivity:

$$M^* = \frac{1}{\epsilon^*} = \frac{1}{\epsilon' - j\epsilon''} \cdot \frac{1}{1} = \frac{1}{\epsilon' - j\epsilon''} \cdot \frac{\epsilon' + j\epsilon''}{\epsilon' + j\epsilon''} = \frac{\epsilon' + j\epsilon''}{\epsilon'^2 + \epsilon''^2} \tag{2.17}$$

This gives us the complex modulus in terms of the dielectric permittivity with the real and imaginary parts as:

$$M^* = \frac{\epsilon'}{\epsilon'^2 + \epsilon''^2} + j\frac{\epsilon''}{\epsilon'^2 + \epsilon''^2} = M' + jM'' \tag{2.18}$$

With the complex modulus formula, we can conveniently use this tool as an alternative for impedance spectroscopy with some additional advantages compared to what we can find with complex impedance spectroscopy, which helps in determining, analyzing, and interpreting the dynamical aspects of electrical transport phenomena. This tool provides an insight into the electrical processes characterized by the smallest capacitance of the material. To truly analyze and interpret the experimental data, it is important to have a model equivalent circuit which will provide a realistic representation of the electrical properties of the sample. The complex modulus representation help suppress the unwanted effects of extrinsic relaxation, which is often used while analyzing the dynamic conductivities of ionic conducting glasses and in the analysis of dielectric data of ionic conductors [21]. The advantage of adopting complex electrical modulus spectra is that it can discriminate against electrode polarization and grain-boundary conduction process [22, 23].

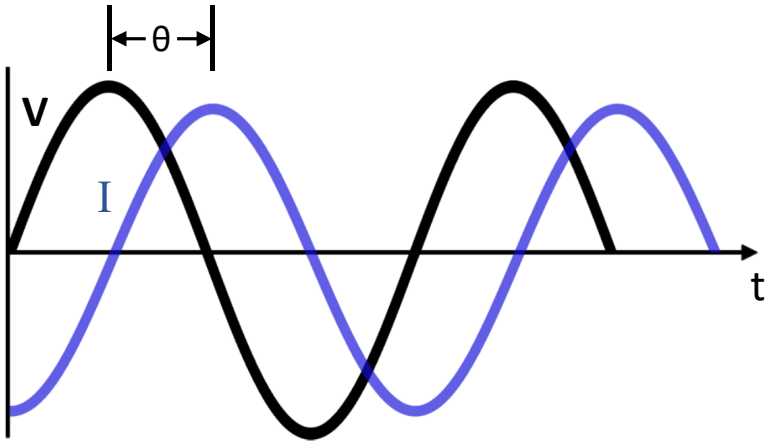

Figure 2.22: Phase angle shift between the voltage and current.

2.2.2.2 Phase Angle

As it was observed in Figure 2.21(b), when capacitors, and similar to inductors, are connected to a sinusoidal voltage source, the current and voltage crests don't peak at the same time. There is a fraction of a temporal phase difference between the peaks of the voltage and current. This is expressed in degrees and is referred to a phase difference. This phase angle is $\leq$ 90 degrees. Normally, the point of reference is the angle by which the voltage leads the current. This translates to having a negative phase angle for circuits with the presence of a capacitor since the current leads the voltage. The phase angle becomes positive when the circuit system has the presence of an inductor, where the voltage leads the current. This is visualized in Figure 2.22.

2.2.2.3 Dielectric Loss and Quality Factor

Alongside the charging current component I_c, we have a loss current component (I_l=$G\mathbf{V}$) in phase with the voltage. G represents the conductance of the dielectric. Then, the total current of the capacitor becomes:

$$I = I_c + I_l = (j\omega C + G)\mathbf{V} \tag{2.19}$$

This current is inclined a power factor angle $\theta < 90°$ against the applied voltage $\mathbf{V}$. This is the loss angle δ against the $+j$-axis. If we consider that the dielectric material acts upon the system as a circuit of a capacitor paralleled by a resistor (RC) then the frequency response of the circuit is expressed as the ratio of the charging current and loss current. In this case, we call the dissipation factor D, or as well as the loss tangent:

$$D = \tan\ \delta = \frac{I_l}{I_c} = \frac{1}{\omega RC} \tag{2.20}$$

This dielectric loss result from the inability in the polarization process with the molecules to follow the rate in which the oscillating applied field change. This comes with the relaxation time (τ) of the material. This is the time taken for the dipoles to return to its original orientation, in simple terms, the time for the material to relax after the applied field is gone or changed. If the relaxation time is smaller or comparable to the rate of oscillating electric field, then there would be no or minimum loss. Then, if the rate of change of the electric field oscillates faster than the relaxation time of the material, then the polarization cannot occur completely and can't follow the oscillating frequency resulting in a energy absorption and dissipated as heat.

Important relations that we can have from the loss coefficient are as well:

$$\tan\ \delta = \frac{\epsilon''}{\epsilon'} = \frac{M''}{M'} = \frac{Z'}{Z''} = \frac{Y''}{Y'} \tag{2.21}$$

The dielectric loss tangent ($\tan\ \delta$) of a material denotes quantitatively dissipation of the electrical energy due to different physical processes such as electrical

conduction, dielectric relaxation, dielectric resonance, and loss from non-linear processes [4]. Origin of dielectric losses can also be considered as being related to delay between the electric field and the electric displacement vectors [5]. The total dielectric loss is the sum of intrinsic and extrinsic losses. Intrinsic dielectric losses are the losses in the perfect crystals which depend on the crystal structure and can be described by the interaction of the phonon system with the ac electric field. The ac electric field alters the equilibrium of the phonon system, and the subsequent relaxation is associated with energy dissipation [68]. The phonon frequency is much higher than the microwave frequency. Hence the low frequency dielectric relaxation in the ideal lattice should be of an harmonic origin. As a result, energy of the field dissipates heat, and the sample gets heated up. The intrinsic dielectric losses depend on the crystal symmetry, ac field frequency and temperature. These intrinsic losses fix the lower limit of losses in defect-free single crystals or ideal pure materials. Extrinsic losses are associated with imperfections in the crystal lattice such as impurities, microstructural defects, grain boundaries, porosity, microcracks, orderdisorder, random crystallite orientation, dislocations, vacancies, dopant atoms etc. The extrinsic losses are caused by lattice defects and therefore can be in principle eliminated or reduced to the minimum by proper material processing. The losses due to different types of defects show different frequency and temperature dependence. The crystals belonging to different symmetry groups have very different temperature and frequency dependencies of dielectric loss [6]. Manufacturers of dielectric ceramics often use the name quality factor for the reciprocal of the tan δ. One should carefully distinguish this quantity from the Q-factor of a resonator which is defined as:

$$Q = 2\pi \frac{maximum\ energy\ stored\ per\ cycle}{average\ energy\ dissipated\ per\ cycle} \tag{2.22}$$

The term quality factor is more commonly associated with microwave resonators. Quality factor, or Q, is a measure of the power loss of a microwave system. For the microwave resonator, losses can be of four types: (a) dielectric, (b) conduction, (c) radiation, and (d) external [1]. The dielectric Q_d, conduction Q_c and radiation Q_r quality factors are given by:

$$Q_d = 2\pi \frac{W_1}{P_d \tau} = \frac{\omega_0 W_1}{P_d},\ Q_c = \frac{\omega_0 W_1}{P_c},\ Q_r = \frac{\omega_0 W_1}{P_r} \tag{2.23}$$

where W_1 is the total stored electric energy in the resonator, ω_0 is the angular resonant frequency, Pd, Pc and Pr represent the power dissipated in the dielectric, conductor and radiation respectively and:

$$\tau = \frac{2\pi}{\omega_0} \tag{2.24}$$

The unloaded quality factor Q_u is related to other Q-factors by:

$$\frac{1}{Q_u} = \frac{1}{Q_d} + \frac{1}{Q_c} + \frac{1}{Q_r} \tag{2.25}$$

where $1/Q_d$ is dielectric loss, $1/Q_c$ the loss due to conductivity of the metallic plates and $1/Q_r$ is the loss due to radiation. Most resonant cavities are completely shielded, so there is no radiation effect, and that term can be ignored.

In practice, external losses ($1/Q_{ext}$) arise due to coupling. To introduce an electromagnetic field in the resonator, microwave conducting probes are brought close to it (typically within millimeters of each other) the higher the dielectric constant of the resonator, the closer the probe must be to it. The electromag-

netic fields around them induce electromagnetic fields in the dielectric ceramic, and so they are coupled; however, the presence of conducting probes in the electromagnetic field lines of the resonator leads to additional loss. The total, or loaded Q-factor, is defined as [1]:

$$\frac{1}{Q_L} = \frac{1}{Q_d} + \frac{1}{Q_c} + \frac{1}{Q_r} + \frac{1}{Q_{ext}} \tag{2.26}$$

where $1/Q_L$ is the total loss of the system and $1/Q_{ext}$ is the loss due to external coupling.

Q_L is determined experimentally from the shape of the resonance peak, as illustrated in Figure 2.23. Loaded quality factor refers to a resonator coupled with external circuit and its relationship with unloaded quality factor depends on the coupling coefficients. A peak occurs in the transmitted signal amplitude at the resonant frequency, and the peak has a finite width. The bandwidth is defined as the width of resonance curve at half power points (Full Width Half Maximum). Then the peak frequency f is divided by FWHM, which is the Q_L:

$$Q_L = \frac{f}{\Delta f} \tag{2.27}$$

The resonator bandwidth is inversely proportional to the Q-factor. Thus, high Q resonators have narrow bandwidth. If the coupling is low (coupling coefficients ¡¡ 1), then the unloaded Q-factor is approximately equal to the loaded Q-factor. In practice, resonators are often used with adjustable couplings which allow such approximation without the need for measuring coupling coefficients. If conduction, radiation, and external losses are negligible, then QL=$1/\tan\delta$. If all conduction, radiation, and external losses are negligible, then the loaded Q-factor depends on dielectric losses in the resonant structure.

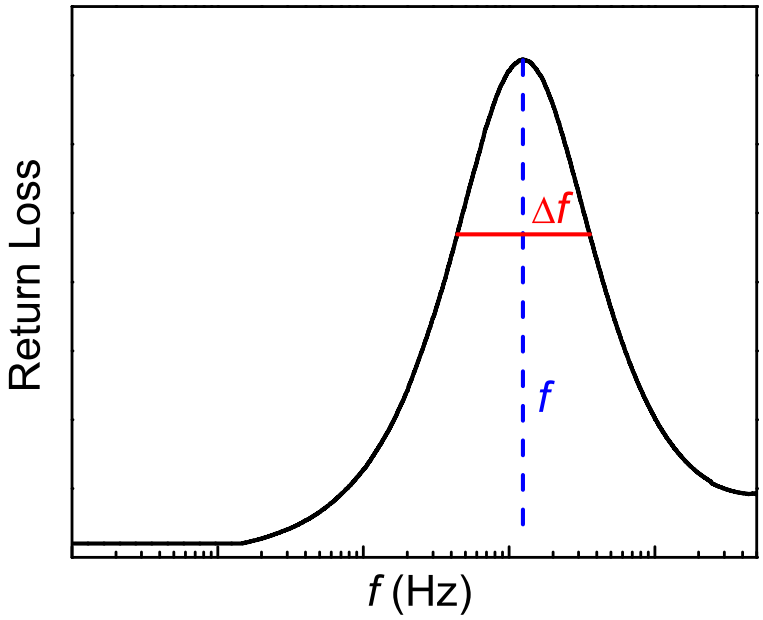

Figure 2.23: Resonant peak and associated parameters.

The coupling losses ($1/Q_{ext}$) are usually determined experimentally and is given by:

$$\frac{1}{Q_u} = \frac{1}{Q_d} + \frac{1}{Q_c} + \frac{1}{Q_r} = \frac{1/Q_L}{1 + \beta c_1 + \beta c_2} \tag{2.28}$$

where βc_1 and βc_2 are coupling coefficients for a resonator with two coupling ports. The radiation losses are negligible for a closed cavity. It should be mentioned here that the inverse of dielectric loss tangent which is commonly named as Q-factor due to dielectric losses is in most cases different from the Q-factor due to dielectric losses of a dielectric resonator (Q_d).

2.2.2.4 Impedance

Circuits that are based on Direct Current (DC) sources, can be described only by the resistor elements within. Capacitors on a DC circuit are basically

open connections, as an infinite value resistor, and an inductor is simply a short connection which acts as a resistor of zero value. When we enter to AC circuits, when an element opposes the current flow, the measure of this is called impedance. We have again the play between the current-voltage ratio with frequency dependance. The impedance must be expressed as a complex quantity, meaning it has a real and imaginary part as:

$$Z = R + jX \tag{2.29}$$

The real part of the impedance is the resistance (R) and the imaginary part is the reactance (X). Here the resistance is always positive, where the reactance can be either positive or negative. Where the resistance dissipates power as heat, the reactance stores energy as an electric or magnetic field. In a capacitor, as observed in Figure 2.22, representing the fact that in a capacitor the current leads the voltage by 90°, then the impedance can be represented as:

$$Z_C = -j\frac{1}{\omega C} \tag{2.30}$$

Here Z_C is the impedance of the capacitor, ω is the angular frequency, where $\omega = 2\pi f$, and f is the frequency of the signal. The capacitance of the capacitor is C. With this we can observe that the resistance of an ideal capacitor should have a value of zero, the reactance is negative for all frequency. The effective impedance of a capacitor is dependent on the frequency, and for an ideal capacitor, it should decrease with frequency.

Furthermore, if we utilize the complex impedance spectroscopy, where we use both real and imaginary parts of the total impedance, we have a powerful tool for characterizing many of the electrical properties of materials and the in-

terfaces with the conducting electrodes. This method can be used to investigate the dynamics of bound or mobile charges in the bulk or the interfacial regions of any kind of solid or liquid material, including insulators (dielectrics). With the complex impedance spectroscopy, we can find an equivalent circuit based on impedance and electric modulus spectra which provides an idea of the physical processes that occur inside the sample. Most of the known ceramics contain grains and grain-boundary regions, this has very different physical properties individually. These regions can be observed within the impedance and modulus spectra. The electrical properties of the present material system have been investigated using this complex impedance spectroscopy technique.

Impedance spectroscopy is normally characterized by the measurement and analysis of most (or all) of the common impedance related functions: Z, Y, M, ϵ, and the plotting of these functions in the complex plane. The plotting of these measurements can be very insightful in interpreting the small-signal AC response of the interaction between the electrode and material system that is being investigated. Historically, the use of Z and Y in the analysis of the response in electrical circuits that are made up of ideal elements (R, L, and C) goes further back to the early days of the discipline of electrical engineering. One of the greatest milestones for the analysis of real systems was the introduction of ϵ' and ϵ" for dielectric systems in the complex plane by Cole and Cole in 1941. It's now known as the Cole-Cole plot, which is an adaptation at the dielectric constant level of the circle diagram of electrical engineering. This has been exemplified by the Smith-Chart impedance diagram [24–27]. Complex plane plot has sometimes been called Nyquist diagrams, but this is an inaccurate naming, however, since Nyquist diagrams refer to transfer function (three or four terminal) response, while conventional complex plane diagrams only two terminal

input of admittance and impedance. Impedance spectroscopy has gained raise as a popular analytical tool in materials research and development, this since it involves a relatively simple electrical measurement that can be easily automated and these results can be correlated with many complex materials variables: from mass transport, rates of chemical reactions, corrosion, and dielectric properties, to defects, microstructure, and compositional influences on the conductance of solids. Using impedance spectroscopy, one can predict aspects in the performance of chemical sensors and fuel cells. This has been used extensively in the investigation of membrane behavior in living cells. It is a useful empirical quality control procedure, yet it can contribute to the interpretation of fundamental electrochemical and electronic processes [28] .

The impedance of a material contains two components: the real and imaginary parts. Both combined gives the main impedance values recorded by an impedance meter. The interaction between these two tells us many informational values like the relaxation processes of the material. The real part is the resistive property of the material (Z'), and the imaginary being the reactive part (Z"). Further information of the impedance real and imaginary parts and their equations and relations can be found in Chapter 2.2.2.4. The impedance can be represented on an Argand diagram, as shown in Figure 2.24, which is the basis for a Nyquist plot. The Argand diagram show the relation between the real and imaginary part with the phase angle between them. The Nyquist plot is what is commonly used to represent the real and imaginary parts of the impedance as one. This can tell information of the internal equivalent circuit of the material. An impedance measurement for a single frequency is a single plot point on a Nyquist plot, this is called a Debye type relaxation. The full impedance spectrum is therefore a series of points, where each point is a different frequency.

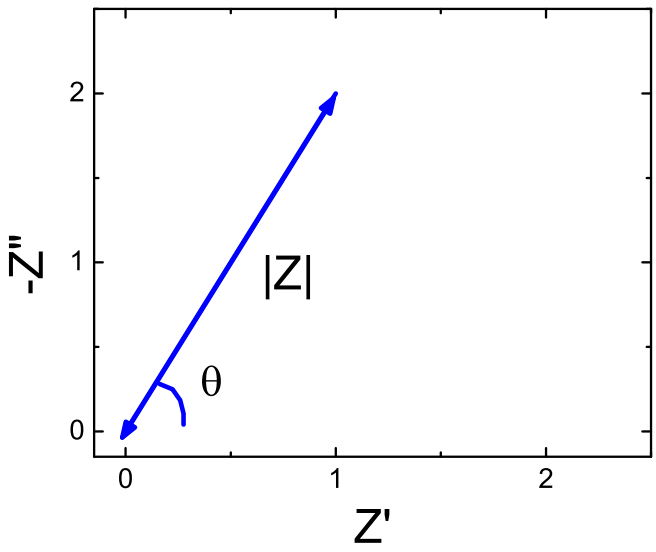

Figure 2.24: Argand diagram of real (Z') vs imaginary (Z") parts of impedance (Z).

For a Nyquist plot, as shown in Figure 2.26, the plot on the Y-axis is negative and each point on the plot is the impedance ant one frequency. The low frequency data are on the right side of the plot and higher frequencies at the left. Figure 2.26 is a 3D visual representation of the Nyquist plot, with how the real (red), imaginary (green) are combined with the frequency to form the distinctive semicircle (blue) Nyquist diagram. The Nyquist plot On these plots, the impedance can be represented as a vector of length |Z| and the angle between this vector and the X-axis is what it's called the "phase angle". Further information on phase angle can be found in Chapter 2.2.2.2. The Nyquist Plot in Figure 2.26 can be a result from the electrical circuit, or combination of Figure 2.25a. The semicircle is characteristic of a single "time constant". Electrochemical impedance plots often contain several semicircles. Often only a portion of a semicircle is seen. When a perfect semicircle is present, this is called a Debye

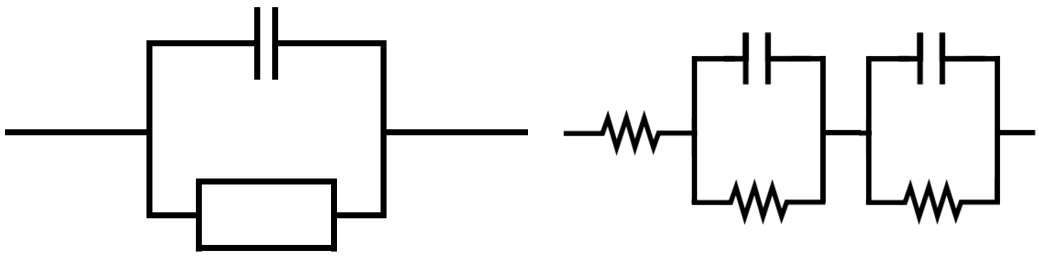

(a) (b)

Figure 2.25: Diagrams of a) Simple equivalent circuit with one time constant and b) sum of two equivalent circuits in series of paralleled capacitance and resistance with a contact resistance in front.

type relaxation, but this almost never happens often [29, 30].

Having in mind that the impedance measured of any material is of the complex type, the imaginary part of the impedance offers many degrees of information that are intrinsic to the material. For materials that have a Nyquist plot where the shape of the semicircle has indications of being the sum of two or more semicircles, we can imply that is a sum of the circuit shown in Figure 2.25a and be as shown in 2.25b. This can be the combined interaction of both the grains and the boundaries of the material. In this case, where we have both grain and grain boundary interaction. we can express the real (Z') and imaginary (Z") parts of the total impedance (|Z|) of the equivalent circuit in Figure 2.25b as:

$$Z' = \frac{R_g}{\left[1 + (\omega R_g C_g)^2\right]} + \frac{R_{gb}}{\left[1 + (\omega R_{gb} C_{gb})^2\right]} \tag{2.31}$$

$$Z" = R_g \left[\frac{\omega R_g C_g}{1 + (\omega R_g C_g)^2}\right] + R_{gb} \left[\frac{\omega R_{gb} C_{gb}}{1 + (\omega R_{gb} C_{gb})^2}\right] \tag{2.32}$$

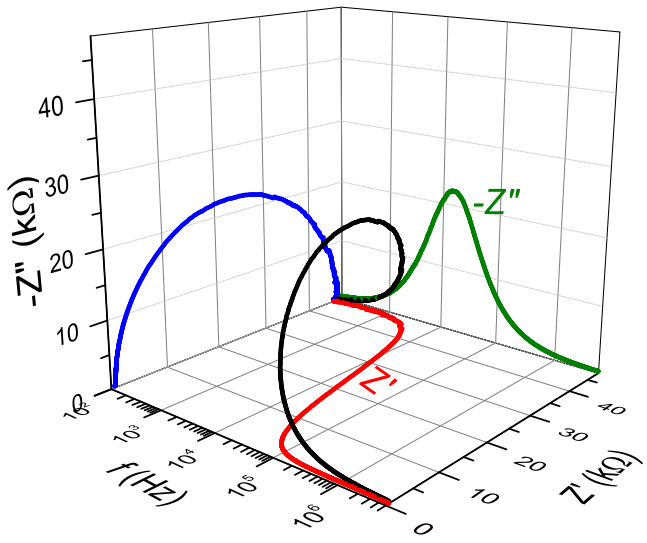

Figure 2.26: 3D plot representing a Nyquist diagram with the interaction of the frequency (Hz)(x axis) vs real (Z') (y axis) vs imaginary (Z")(z axis) parts of the impedance (Z) for a sample Ni/PZT/Ni with d_{PZT}= 7 μm.

where R_g and R_{gb} are the grain and grain boundary resistances, and C_g and C_{gb} are the grain and grain boundary capacitances respectively [3, 4, 33]. The peaks of semicircles occur at different frequencies, which suggests the existence of distributed relaxation time in the material. Using the finite element method, we calculated the impedance of the heterostructure exhibiting higher resistive grain boundaries with microstructures and grain boundary properties deviating from the simple brick layer model. Detours around highly resistive regions (e.g. due to high grain boundary density or enhanced grain boundary resistivity) can play an important role and lead to grain-boundary semicircles depending on bulk properties and even to additional semicircles [34].

Utilizing an electrochemical impedance spectroscopy (EIS) spectrum analyzer (EISSA) software, the equivalent circuit can be simulated and fitted on

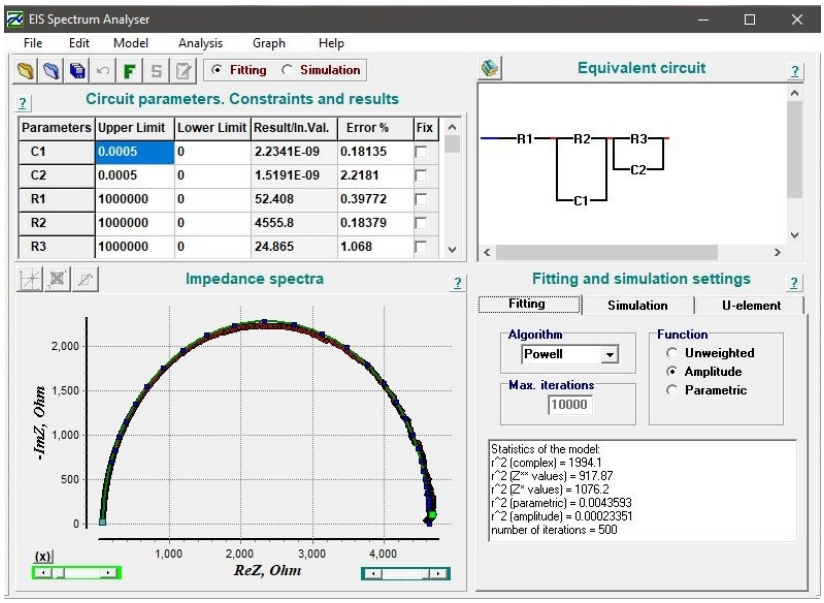

Figure 2.27: Electrochemical impedance spectroscopy analyzer software with a fit for a specified reference circuit.

to the experimental measurements of the Nyquist plot. This program gives the advantage that you can create almost any type of circuit and test its fitting. Figure 2.27 show the windows version of the EIS spectrum analyzer software with an equivalent circuit, the fit (in green), and the respective values of the elements within the circuit [35].

2.2.3 Magnetic Measurements

To understand the magnetodielectric (MD) coupling, measurements of magnetocapacitance (MC) and magnetoimpedance (MI) of the samples were done at room temperature. An intrinsic magnetoresitance (MR) has been observed to enhance the MD effect from inhomogeneities. Within ceramics, the MR is mainly dominated by the spin-polarized tunneling across the grain boundaries [36, 37] . To be able to rule out the MR related MD coupling effect, frequency dependent

MC and MI are measured at room temperature. The change percentage in MC was measured with and without the presence of a magnetic field as:

$$MC(H) = [C(H) - C(0)] = C(0) \tag{2.33}$$

$$MI(H) = [Z(H) - Z(0)] = Z(0) \tag{2.34}$$

where *C(H)* and *Z(H)* are the capacitance and impedance with a magnetic field 'H' present and *C(0)* and *Z(0)* are the capacitance and impedance without a magnetic field present.

The magnetic element of new materials has come to a very important level, since with the same composite material can be "tuned" with just applying a magnetic presence into it. This gives a material that can be switched depending on the presence and strength of this external field, and as well, this material can act as a sensor due to magnetic presence. With this in mind, we need to have a magnetic element present in the material studied, and since this is a Multiferroic, we have two components present: the ferroelectric and the ferromagnetic. Both are coupled and when one is affected the other is too. The three main ferroelectric elements present in nature are iron (Fe), cobalt (Co), and nickel (Ni). These elements are highly affected by magnetic presence, and coupled with our ferroelectric (Lead Zirconate Titanate) we want to know how and how much does the magnetic element coupled interacts with the total outcome of the composite. With this in mind, we place the samples inside a magnetic field that we can control and measure all the data points at different magnetic field strengths to determine the interaction of the magnetic-ferroelectric coupling. On Figure **??**, we observe a sample being held by the tweezer attachment of the HIOKI Hi-

Tester, which does the dielectric measurements, inside the electromagnet that has a maximum magnetic field capacity up to 2 Tesla (T). The measurements were carried out in a up and down magnetic field starting from 0 T (no magnetic presence) up to 2 T, and back down to 0 T with increments of 0.25 T.

References

[1] Wells, A. F. Structural Inorganic Chemistry (5th ed.), Oxford: Clarendon Press, ISBN 0-19-855370-6 (1984)

[2] Turova, N.Y. "9.4 Germanium, tin, lead alkoxides". The Chemistry of Metal Alkoxides. Springer. p. 115. ISBN 978-0-7923-7521-0 (2002)

[3] R. Stevens. Introduction to Zirconia. Magnesium Elektron Publication No 113 (1986)

[4] Greenwood, N. N.; & Earnshaw, A. Chemistry of the Elements (2nd Edn.), Oxford:Butterworth-Heinemann. ISBN 0-7506-3365-4 (1997)

[5] El, Goresy; Chen, M; Dubrovinsky, L; Gillet, P; Graup, G . "An ultradense polymorph of rutile with seven-coordinated titanium from the Ries crater". Science. 293 (5534): 146770. (2001)

[6] El Goresy, Ahmed; Chen, Ming; Gillet, Philippe; Dubrovinsky, Leonid; Graup, GNther; Ahuja, Rajeev . "A natural shock-induced dense polymorph of rutile with -PbO2 structure in the suevite from the Ries crater in Germany". Earth and Planetary Science Letters. 192 (4): 485. (2001)

[7] J.E. Mahan, Physical Vapor Deposition of Thin Film, John Wiley & Sons, Inc. (2000)

[8] D.L.Smith, "Thin-Film Deposition: Principles Practice", McGrawHill (1995)

[9] J.M. Mochel, US Patent 2,564,707 (1951)

[10] J.E. Hill and R.R. Chamberlin, US Patent 3,148,084 (1964)

[11] R. R. Chamberlin, J. S. Skarman. Chemical spray deposition process for inorganic films. Journal of the Electrochemical Society, **113**(1):86-89, (1966)

[12] M.S. Tomar and F.J. Garcia,Progress in Crystal Growth andCharacterization of Materials,4(3), 221 (1981).

[13] D.S. Albin, S.H. Risbud. Advanced Ceramic Materials, 2(3A), 243 (1987)

[14] B.R. Pamplin. Progress in Crystal Growth and Characterizationof Materials, 1(4), 395 (1979)

[15] P.S. Patil, Mater. Chem. Phys.,59(3), 185 (1999)

[16] P. Bohac, L.J. Gauckler, in Oxygen Ion and Mixed Conductors and their Technological Applications, Kluwer Academic Publishers, Dor-drecht, p. 271. (2000)

[17] HIOKI Instruction Manual, Hioki E.E. Corporation (2008)

[18] A. R. von Hippel, S. O. Morgan, Dielectric Materials and Applications. Journal of The Electrochemical Society. **102** 68C (1955)

[19] A. R. Von Hippel, Dielectric Materials and Applications, MIT Press and John Wiley & Sons inc. (1954)

[20] A.K. Roy, K. Prasad, A. Prasad, Electrical Conduction in $(Na_{0.5}Bi_{0.5})_{1-x}Ba_xTiO_3$(0=x=1) Ceramic by Complex Impedance/Modulus Spectroscopy, ISRN Ceram. **2013** 112 (2013)

[21] N. G. McCrum, B. E. Read, and G. Williams, Anelastic and Dielectric Effects in Polymeric Solids, John Wiley & Sons, New York, NY, USA, (1967)

[22] C. T. Moynihan, Analysis of electrical relaxation in glasses and melts with large concentrations of mobile ions, Journal of Non-Crystalline Solids, vol. 172174, no. 2, pp. 13951407, (1994)

[23] C. T. Moynihan, L. P. Boesch, and N. L. Laberge, Decay function for the electric field relaxation in vitreous ionic conductors, Physics and Chemistry of Glasses, vol. 14, no. 6, pp. 122125, (1973)

[24] K. S. Cole and R. H. Cole. Dispersion and Absorption in Dielectrics. I. Alternating-Current Characteristics, J. Chem. Phys. 9, 341351. (1941)

[25] C. W. Carter. Impedance of Networks Containing Resistances and Two Reactances, Bell Sys. Tech. J. 4, 387401. (1925)

[26] P. H. Smith. Transmission Line Calculator, Electronics 12, 2931. (1939)

[27] P. H. Smith. An Improved Transmission Line Calculator, Electronics 17, 130133, 318325. (1944)

[28] E. Barsoukov, J. R. Macdonald. Impedance Spectroscopy Theory, Experiment, and Applications. John Wiley & Sons, Inc. (2005)

[29] Sen S, Choudhary RNP, Pramanik P. Structural and electrical properties of Ca2+ modified PZT electroceramics. Physica B. 2007;387:5662.

[30] Behera B, Nayak P, Choudhary RNP. Impedance spectroscopy study of NaBa2V5O15 ceramic. J Alloy Compd. 2007;436:226232.

[31] Swagatika Dash, R. Padhee, Piyush R. Das & R.N.P. Choudhary, Dielectric and impedance spectroscopy of (Bi0.5Li0.5)(Fe0.5Nb0.5)O3 multiferroics, Phase Transitions, 87:3, 223-235 (2014)

[32] Jonscher AK. The universal dielectric response. Nature. 1977;267:673679.

[33] Jorcin JB, Orazem ME, Pebre N, Tribollet B. CPE analysis by local electrochemical impedance spectroscopy. Electrochim Acta. 2006;51:14731479.

[34] J. Fleig, J. Maier, The impedance of ceramics with highly resistive grain boundaries: validity and limits of the brick layer model, Journal of the European Ceramic Society, Volume 19, Issues 67, (1999)

[35] Bondarenko A. S., Ragoisha G. A. In Progress in Chemometrics Research, Pomerantsev A. L., Ed.; Nova Science Publishers: New York, pp. 89102 (2005)

[36] Catalan G. Appl. Phys. Lett. 88102902 (2006)

[37] Tang J, Feng L, and Wiemann J A. Appl. Phys. Lett. 74 2522 (1999)

[38] B. E. Warren. *X-Ray Diffraction*, Courier Corporation, (1969)

Chapter 3

Fe/PZT/Fe Multiferroic Heterostructures

This chapter will discuss all the capacitor samples that has iron as the ferromagnetic layer. The measurements discussed will include the dielectric properties, impedance spectroscopy, and magnetic properties. These samples have the shape of Fe/PZT/Fe, Fe/PZT/Ag, and Ag/PZT/Ag as reference. The chapter is divided in two parts, where the first is the bulk samples that include thicknesses of d_{PZT}=1.00 mm and d_{PZT}=200 μm; and the second part of the chapter being the thin samples which include thicknesses of d_{PZT}=1.4 μm and d_{PZT}=2 μm. Dielectric measurements show that all samples share ferroelectric behavior. The bulk samples are commercially available PZT substrates of which iron was sputtered on top and bottom to make a simple capacitor shape. Impedance spectroscopy show that these samples do not exhibit a peak in the imaginary part of the impedance, since these are too thick and the resonance frequency is overly damped and into the lower frequencies, which are out of the measured range. The imaginary peak is then extrapolated by the fitting of the circuit equation 2.32. The phase angle of the d_{PZT}=1.00 mm samples show that it acts as a capacitor at lower frequencies until it reaches a resonant frequency, whereas the Fe/PZT/Fe d_{PZT}=200 μm samples show that it starts as almost a resistor, since it is close to 0°and has high dissipation visible in the loss coefficient measurements, meaning that there is leakage current. This is evident since the sample is 5 times thinner. Furthermore, the thin samples where both SPL deposited PZT samples, show

the same behavior where the phase starts close to 0°at lower frequencies, and falls to almost -90°. The dielectric behavior is apparent in these samples as well, showing very similar shape as the bulk but at a lower magnitude.

3.1 Experimental Details

PZT substrates of d_{PZT}=1.00 mm with area of 1.00 cm x 1.00 cm and d_{PZT}=200 μm with an area of 3.00mm x 1.00mm were obtained and deposited ferromagnetic iron contacts on top and bottom by sputtering, giving them simple capacitor shape with ferromagnetic/ferroelectric/ferromagnetic configuration as shown in Figure 3.1a. These are the bulk samples. Furthermore, thinner samples were made using Spray Pyrolysis to deposit PZT onto a copper laminate that had a top layer of iron deposited to make the bottom contact, and after the SPL deposited PZT, a top iron contact was deposited to achieve the same capacitor structure as the bulk samples, so the measuring devices and methods are equal.

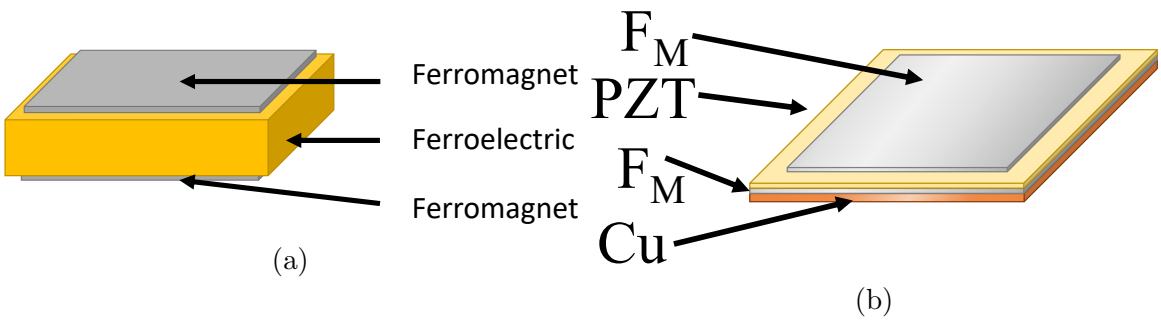

Figure 3.1: Simple capacitor structure of a) $F_M/F_E/F_M$ samples and b) thin films on top os a Cu foil.

The thin samples were put through a AFM/Profilometer to determine their thickness. The measured average thickness of two selected samples were of 1.4 μm and the other of 2 μm. The thickness achieved is approx. 100 times thinner than the commercially obtained samples of 200 μm. Following suit as with the samples

done before, the SPL deposited Fe/PZT/Fe samples were subjected to the same measurements and conditions. Dielectric measurements were done for both bulk and thin samples in the range of 100 Hz to 5 GHz with a magnetic field presence from 0 T up to 2 T and back down.

3.2 Results and Discussion

3.2.1 Bulk Samples

Various frequency dependent dielectric measurements were carried out for the samples containing the ferromagnetic material of iron. Six samples were made that consist of three different capacitor configurations (Fe/PZT/Fe, Fe/PZT/Ag, and Ag/PZT/Ag as reference), with two different substrate thicknesses (d_{PZT}=1.00 mm and d_{PZT}=200 μm). The dielectric measurements done where: capacitance (which in turn can be translated to dielectric permittivity), phase angle, impedance, loss coefficient, loaded Quality Factor, magnetocapacitance, and magnetoimpedance (which is dependent on magnetic fields). The range of frequencies used where from 100 Hz up to 5 MHz. The magnetocapacitance measurements where done with an external applied magnetic field with maximum strength of 2 T. With the complex impedance information, divided by its real and imaginary components, the reference circuit was calculated for those samples using a Nyquist plot that show a clear peak in the imaginary part.

3.2.1.1 Dielectric Permittivity

The dielectric permittivity measurements are of great importance to understand the ranges and values at which the material behaves. This gives us the ability of the material to act as a capacitor and how much capacitance can it

withhold, and at which range of frequencies we have either no major changes or high fluctuations. The samples where subjected to capacitance measurements for the frequency range of 100 Hz up to 5 MHz. As well, the samples where introduced to a magnetic field for a range from 0 T up to 2 T and back down to 0 T, this gives us the relationship in the ferroelectric and ferromagnetic coupling and the reminiscence of it. To obtain the dielectric permittivity of each sample, their capacitance measurement was multiplied by a factor containing the information of the ferromagnetic contact area, thickness of the PZT layer and dielectric constant of vacuum.

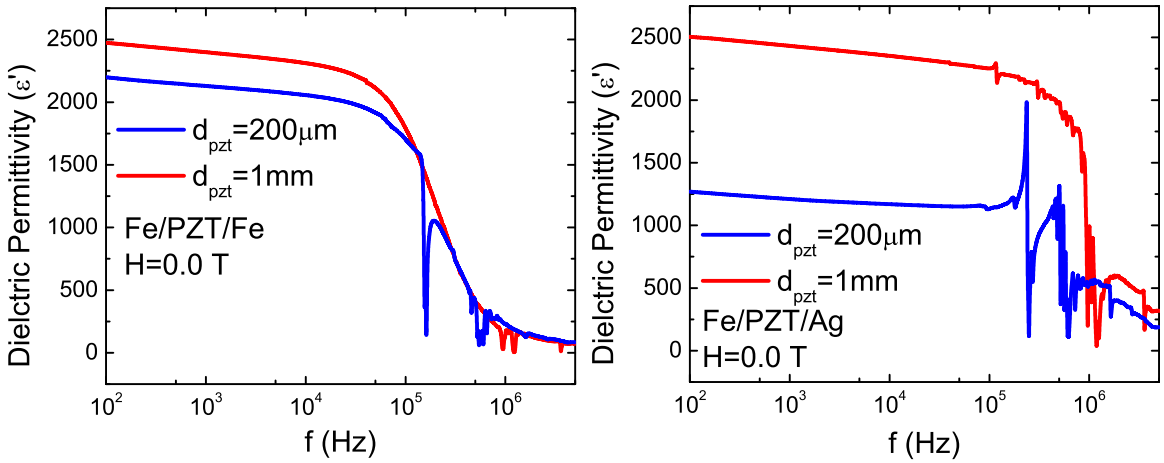

Figure 3.2: Dielectric permittivity of (a) 1mm PZT and 200μm with Fe/PZT/Fe configuration and (b) 1mm PZT and 200μm with Fe/PZT/Ag at 0T and room temperature.

Figure 3.2a show the frequency variation of dielectric permittivity for Fe/PZT/Fe with both 1 mm and 200 μm. We can observe the ability of the sample to store energy as a capacitor and its stability within the frequency range of 100 Hz up to 10 kHz. The dielectric permittivity of this range is within 2500 max down to ≈2000. This is a typical range for dielectric constant values for bulk ceramics. The samples decay at an approximate rate of 0.002 ϵ/Hz. At higher

frequencies than 10kHz, we find that there is a more erratic behavior, meaning that the samples loose stability and reach a resonant frequency range. For the sample of Fe/PZT/Fe d_{PZT}=1 mm, it is observable the drop in dielectric permittivity starting at ≈40kHz, same with the d_{PZT}=200 μm sample. This is typical ferroelectric behavior. These samples show inverse peaks at certain frequencies within the frequency range of 140 kHz up to 4 MHz. These are moments where the leakage current is very high. At 160kHz, the Fe/PZT/Fe 200 μm sample show a large inverse peak, which is two peaks close together and can be better observed in Figure 3.3b. This is followed by a set of peaks in the range of 450kHz to 890kHz.

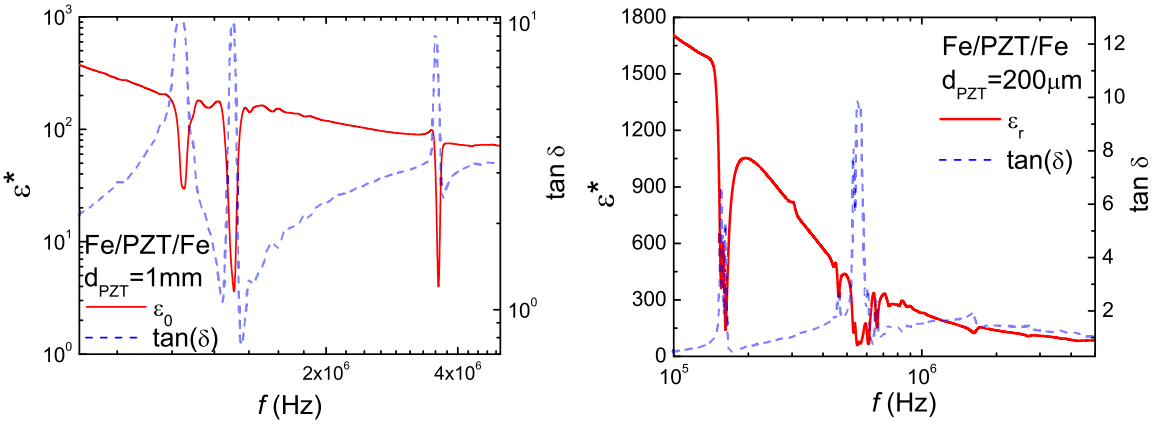

Figure 3.3: Comparison of the dielectric permittivity with loss coefficient of Fe/PZT/Fe for (a) d_{PZT}= 1.00 mm and (b) d_{PZT}=200μm at 0T and room temperature.

Figures 3.3 and 5.4 show the relationship of the dielectric permittivity with the loss coefficient. Since the loss coefficient is directly related to the capacitance, we can note that where there is a spike in the dielectric permittivity, there is an inverse spike in the loss coefficient, and the opposite is equal, where there are peaks in the loss coefficient, there are inverse peaks in the dielectric permittivity. This tells that where the capacitance drops, there is a loss, or a leakage of current.

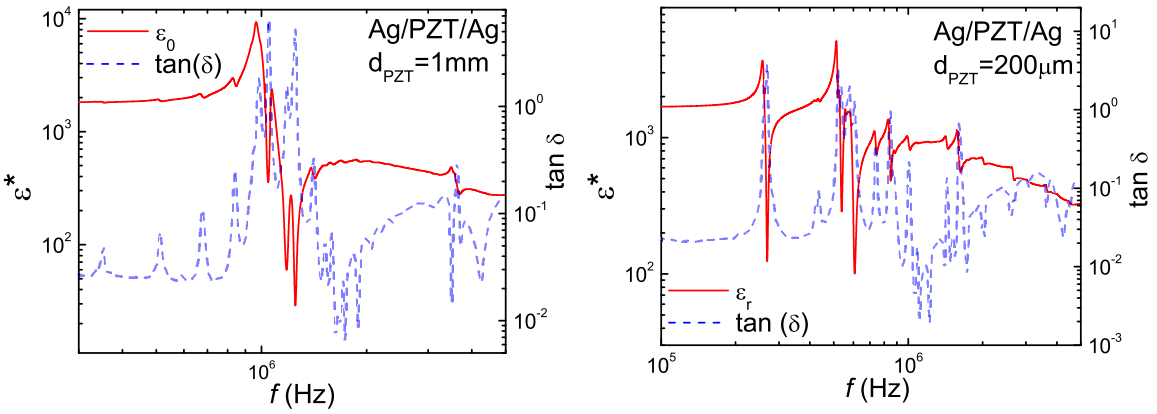

Figure 3.4: Comparison of the dielectric permittivity with loss coefficient of Ag/PZT/Ag for (a) d_{PZT}= 1.00 mm and (b) d_{PZT}=200μm at 0T and room temperature.

In an ideal resonator, the power dissipation is zero, whereas in a 'lossy' resonator, due to piezoelectric coupling, the power dissipation becomes large at resonance.

Table 3.1: Frequency of resonance and relaxation peaks in the imaginary part of Fe/PZT/Fe.

Fe/PZT/Fe	**d_{PZT}=1.00mm**	**d_{PZT}=200μm**
$\boldsymbol{f}_{peak}$	202kHz	4.2kHz
τ	4.94x10^{-6}s	2.38x10^{-4}s
Max ϵ"	1043	2062

Dividing the dielectric permittivity by its complex components, being the real and imaginary parts, we can observe if there are relaxations and/or resonances present in the frequency range. This is obtained utilizing the phase angle information. The dielectric permittivity is then multiplied by the cosine of the phase, for the real part, and the sine of the phase, for the imaginary part. For the d_{PZT}=1.00 mm sample, shown in Figure 3.5a, we observe that the real part closely resembles the whole complex dielectric permittivity, where there is one drop in magnitude, that is accompanied by a peak in the imaginary part.

This is evidence of a relaxation process. This relaxation occurs at the frequency ≈140 kHz, where the imaginary peak is highest. This frequency range correspond to the space-charge relaxation range, meaning that there is a relaxation of dipoles within the sample, until this frequency, where it stops. We can determine that it is a stop in space-charge polarization because it falls within the range of < 1 MHz. Followed, there are smaller resonance peaks at the range of 1 MHz and ≈3 MHz. The resonance peaks are identifiable by their shape. First the value increases quickly, then falls below unity, and eventually makes its way back up toward unity. Figure 3.7 is a Cole-Cole diagram of the d_{PZT}=1.00 mm sample, where the 'X' axis is the real part and 'Y' axis the imaginary part of the dielectric permittivity, of the relaxation process. Figure **??** is a three dimensional representation behind the Cole-Cole plots, here is possible to observe the frequency range of the shape. The highest most point of the semi-circle correspond to the peak in the imaginary part. At this point, its corresponding frequency determines the relaxation time τ. Table 3.1 show the frequency of the relaxation at the peak of the imaginary part, and the relaxation time 'τ'. This value is close to reported ones of the range of x^{-5}s [1].

The Figure 3.5b show the real and imaginary components of the dielectric permittivity for the 200 μm sample. This sample behaves differently than the 1.00 mm sample. The real part shows a fast decline from 100 Hz, up to ≈10 kHz, then rises into a resonance peak, where there is a sharp rise and fall, then return to unity. This top peak is at 148 kHz, and bottom at 161 kHz. in the middle we see the imaginary peak corresponding to this resonance at 158 kHz. The drop of the real part, and rise in the imaginary, suggests that there is a relaxation happening. Unfortunately, since the real/imaginary diagram show a very rare behavior, the Cole-Cole plot show a very erratic collection of curves. At least

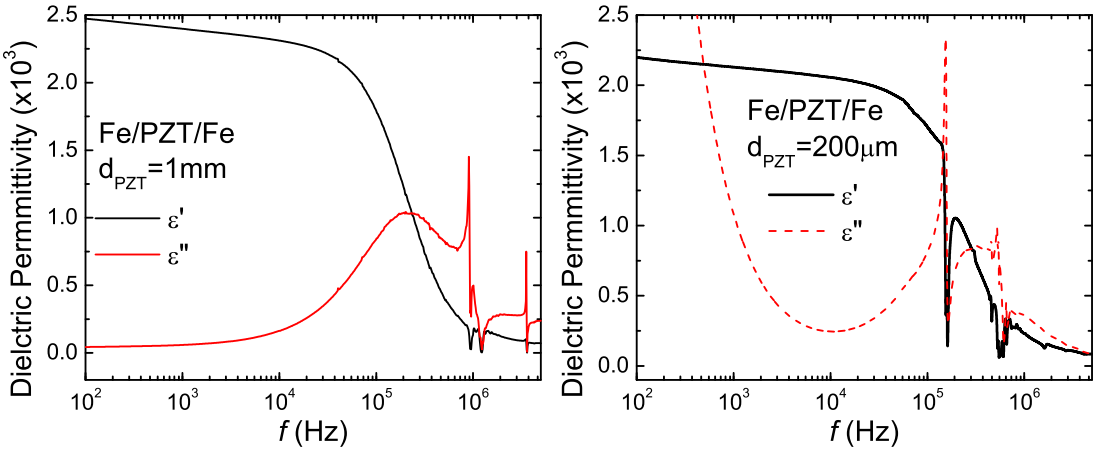

Figure 3.5: Complex dielectric permittivity comparison of (a) 1mm PZT and (b) 200μm of Fe/PZT/Fe with real and imaginary parts of the dielectric permittivity.

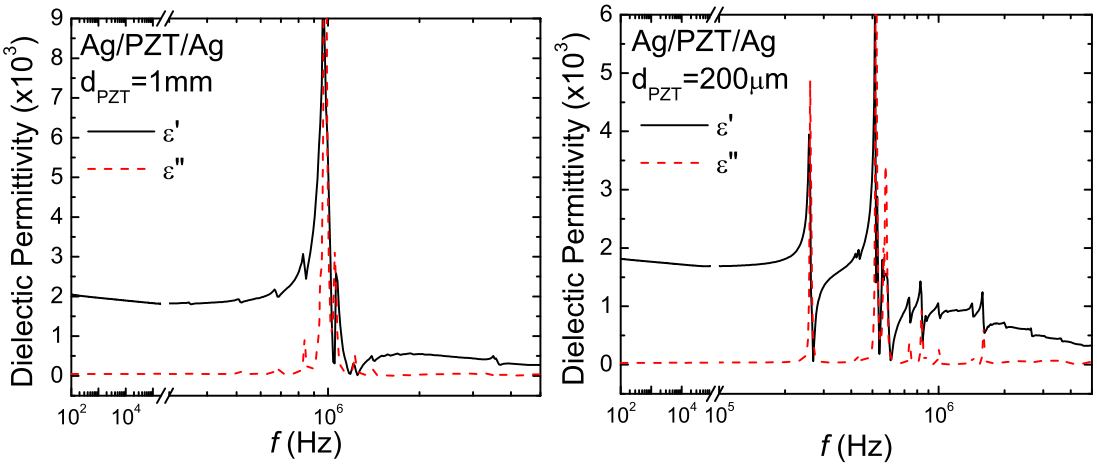

Figure 3.6: Complex dielectric permittivity comparison of (a) 1mm PZT and (b) 200μm of Ag/PZT/Ag with real and imaginary parts of the dielectric permittivity.

half a circle is observed, determining that there is relaxation, but due to the resonance, the signal becomes too erratic.

3.2.1.2 Phase Angle and Dielectric Loss

The angle of the phase demonstrates the relationship between the real and imaginary parts of the material and its electrical properties. This relation be-

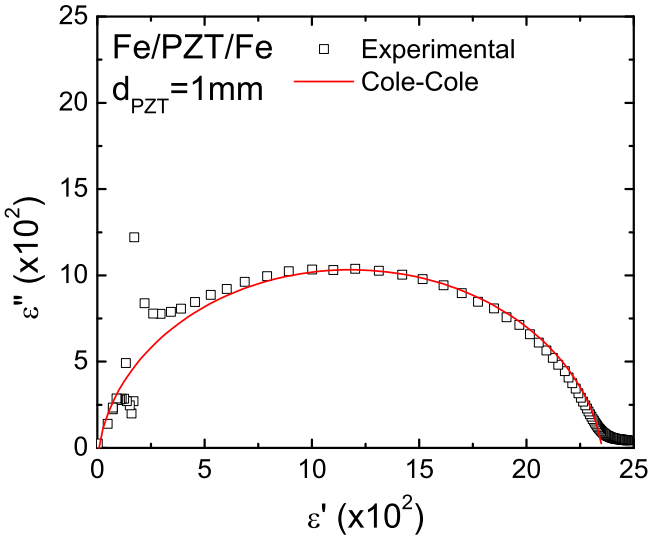

Figure 3.7: Cole-Cole diagram of 1mm PZT Fe/PZT/Fe with real and imaginary parts of the dielectric permittivity and their relationship with the frequency range.

tween the real and imaginary brings the relationship of the loss and storage properties. The phase is the ratio between real and imaginary, where the dielectric loss coefficients represent the electrical loss due to dissipation of energy. Figure **??** show the dielectric loss coefficient of both samples, Fe/PZT/Fe with both thicknesses (3.8) and Fe/PZT/Ag with both thicknesses (**??**). Fe/PZT/Fe with thickness of 1.00 mm show a rise in loss per rising frequency, but it is not linear, with a higher rate in rise after $\tilde{1}$MHz. On the other hand, the 200 μm sample starts with a loss of approximately 5, then lowers to $\tilde{0}$.12 at 10 kHz, and rise again to a sharp peak at 155kHz. The mean path is similar to the 1.00 mm sample, with the difference at low frequencies. This means that at 10 kHz, the 200 μm sample is at its lowest dissipation, or at its highest Q factor. Figure 3.9 show the Q-Factor spectroscopy of all Fe/PZT/Fe and Fe/PZT/Ag samples. Since Q is the inverse of the dissipation, we can see that where Q is highest, the dissipation is at its lowest.

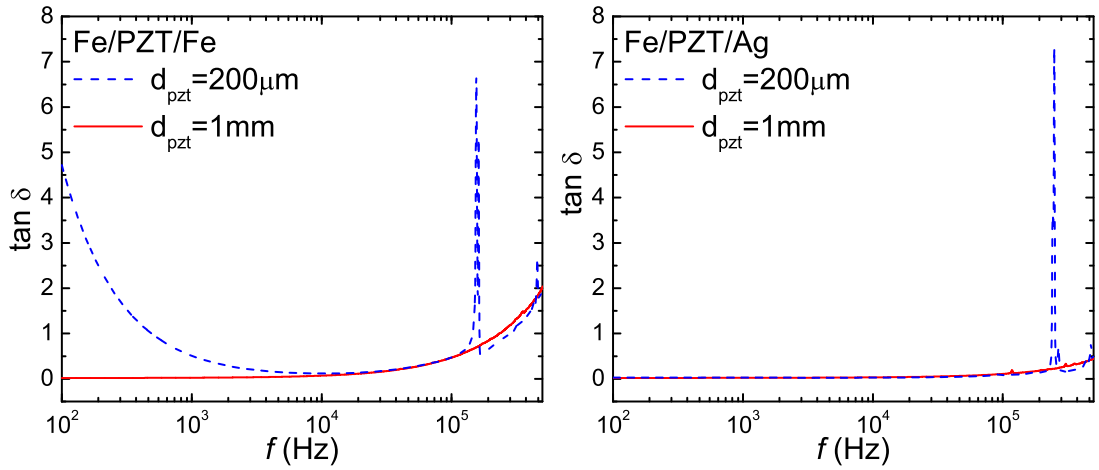

(a) (b)

Figure 3.8: Loss coefficient ($\tan(\delta)$) of (a) 1mm PZT and 200μm with Fe/PZT/Fe configuration and (b) 1mm PZT and 200μm with Fe/PZT/Ag at 0T and room temperature.

3.2.1.3 Impedance Spectroscopy

The impedance spectroscopy of the iron based samples were obtained by the measurements of complex impedance, which includes its real (resistance) and imaginary (reactance) parts. The imaginary part holds all the information necessary to study the samples, including resistance values for the equivalent circuitry of the samples. Figure 3.11 show the imaginary part of the impedance for sample Fe/PZT/Fe with PZT thickness of 1.00 mm (3.11a) and 200 μm (3.11b). Since these samples are very thick, the damping is very evident, moving its relaxation into the lower frequencies. Figure 3.11a show how the thickness affect so much compared to the thinner sample in Figure 3.11b that the peak fall outside of the measured spectrum. For the 200 μm sample we see that this peak is at the edge of the measured spectra. Utilizing Jonscher's dielectric response model mentioned in Section 2.2.2.4 and the equation [3, 4]:

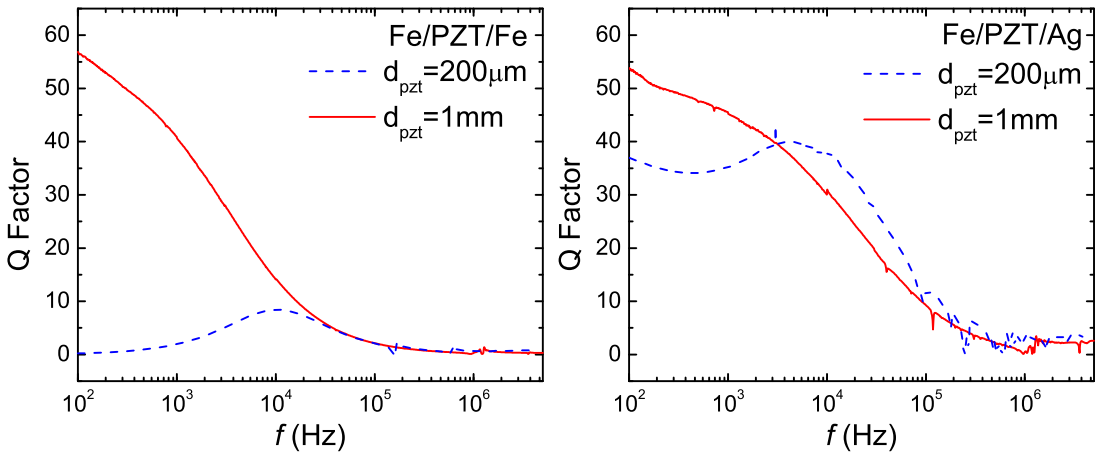

(a) (b)

Figure 3.9: Q-Factor of 1mm PZT and 200μm with (a) Co/PZT/Co and (b) Co/PZT/Ag configuration at 0T and room temperature.

$$Z" = R_g \left[\frac{\omega R_g C_g}{1 + (\omega R_g C_g)^2} \right] + R_{gb} \left[\frac{\omega R_{gb} C_{gb}}{1 + (\omega R_{gb} C_{gb})^2} \right] \tag{3.1}$$

We can extrapolate the peak. Figure 3.11 demonstrate the fit of the Jonscher model on top of the measured experimental data. This give the values for the resistance and capacitance for the equivalent circuit which can be represented as two systems of a resistance parallel to a capacitance which are in series, better illustrated in Figure 5.13. Table 3.2 show all the important information obtained from the Jonscher model fit, including the resistance and capacitance values of the equivalent circuit. These values can be corroborated utilizing a fitting program of the nyquist plots using the real and imaginary parts of the samples, but since these samples are big enough to have the peak outside of the range, the nyquist plot is not possible to build. Here we observe the resistances for the grain (R_g), and the grain boundary (R_{gb}) are acceptable physical values. The same can be observed for the measured and extrapolated data of the Fe/PZT/Ag samples, where in Figure 3.13 it is shown the plotted and fitted Jonscher model.

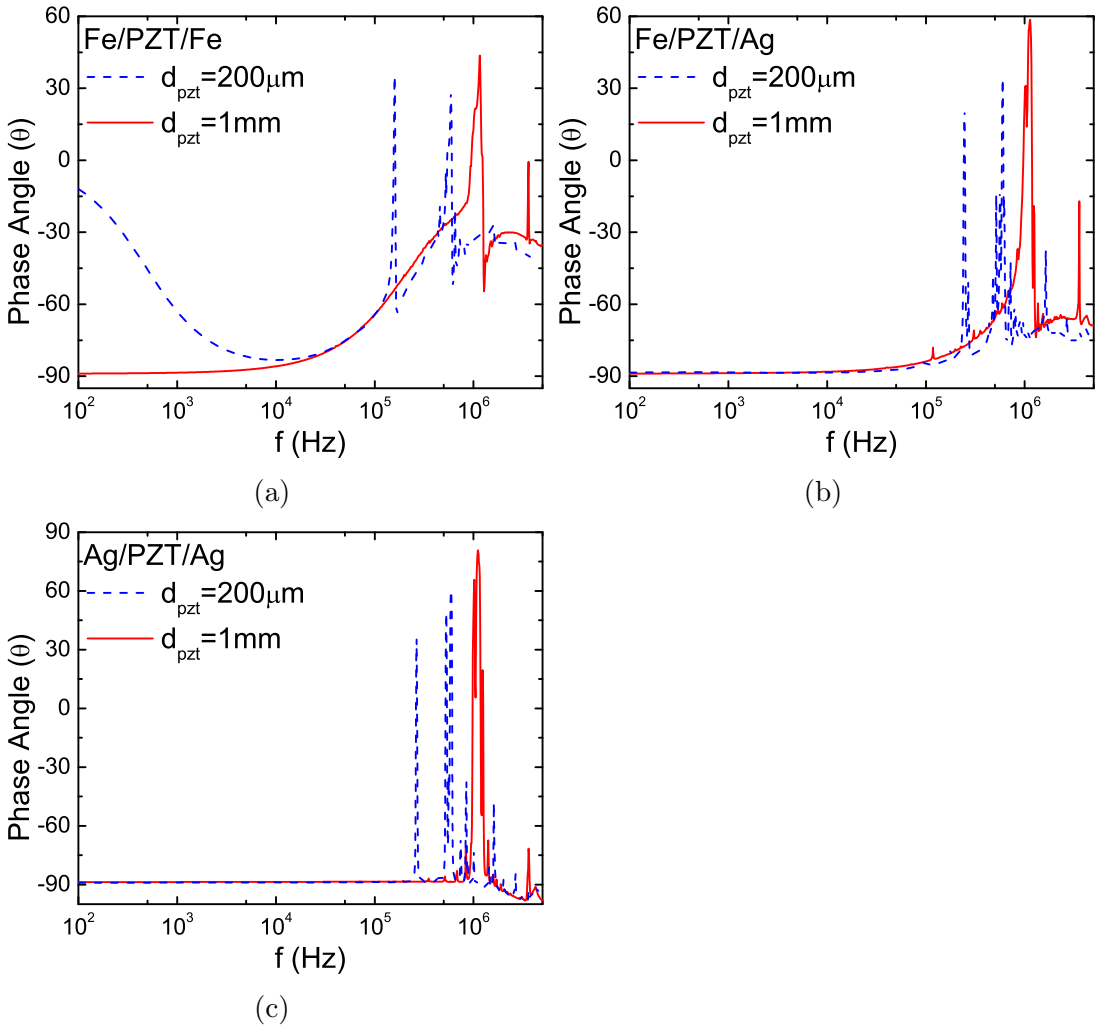

Figure 3.10: Phase Angle (θ) of (a) 1mm PZT and 200μm with Fe/PZT/Fe configuration, (b) 1mm PZT and 200μm with Fe/PZT/Ag, and (c) 1mm PZT and 200μm with Ag/PZT/Ag at 0T and room temperature.

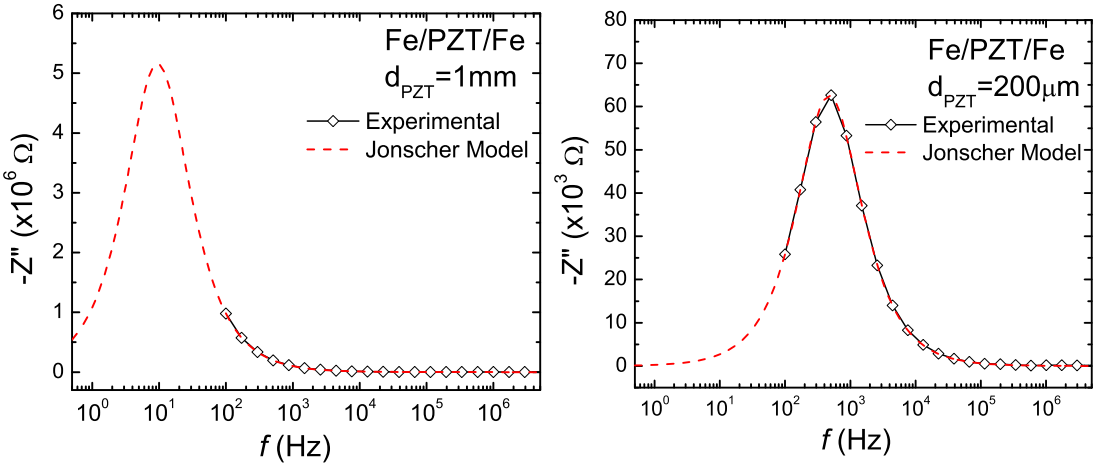

Figure 3.11: Frequency dependent reactance (Z") of Fe/PZT/Fe (a) d_{PZT}=1.00 mm and (b) d_{PZT}=200 μm.

Table 3.2: Important information from Z" utilizing Equation 5.1 for Fe/PZT/Fe and Fe/PZT/Ag.

Sample	$\mathbf{R}_g$ **(Ω)**	$\mathbf{R}_{gb}$ **(Ω)**	$\mathbf{C}_g$ **(F)**	$\mathbf{C}_{gb}$ **(F)**	$\boldsymbol{f}_{peak}$ **(Hz)**
Fe/PZT/Fe					
1.00 mm	5824	$1.04\text{x}10^{7}$	$4.66\text{x}10^{-8}$	$1.62\text{x}10^{-9}$	9.3
200 μm	20804	$1.07\text{x}10^{5}$	$1.03\text{x}10^{-8}$	$3.38\text{x}10^{-9}$	486
Fe/PZT/Ag					
1.00 mm	6074	$1.19\text{x}10^{7}$	$4.51\text{x}10^{-8}$	$1.58\text{x}10^{-9}$	8
200 μm	9781	$8.77\text{x}10^{6}$	$2.98\text{x}10^{-8}$	$1.50\text{x}10^{-9}$	13
Ag/PZT/Ag					
1.00 mm	5591	$6.56\text{x}10^{6}$	$4.51\text{x}10^{-8}$	$1.79\text{x}10^{-9}$	13
200 μm	5666	$1.16\text{x}10^{7}$	$4.68\text{x}10^{-8}$	$1.38\text{x}10^{-9}$	9.4

From Table 3.2, we can observe that the thickness and presence of the ferromagnetic layer affect the placement of the peak in the spectrum. It is evident that thicker the sample, greater the resistance, since the charge has to travel a greater distance. The thickness as well brings closer to lower frequencies the thicker the sample, and with greater presence of ferromagnets, the higher the frequency of the peak. We can observe the difference between Fe/PZT/Fe and

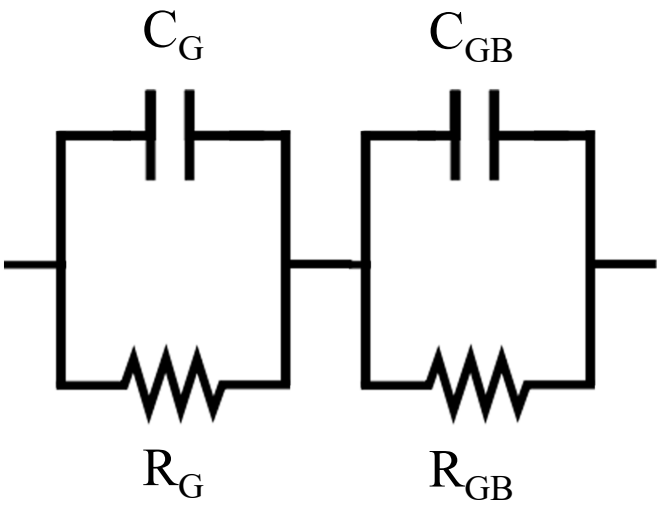

Figure 3.12: Equivalent circuit for samples with grain and grain boundary elements in series.

Fe/PZT/Ag. Ag/PZT/Ag is shown as well as a reference for a normal capacitor without the spin nature. The imaginary parts of the Ag/PZT/Ag samples are shown in Figure 5.16

Table 3.3: Information gathered by the imaginary part of the impedance (Z") including resonance frequency (f_r), resonance bandwidth (Δf), Quality factor (Q_m), damping coefficient (β), and damping ratio (ζ) of Fe/PZT/Fe with both thicknesses.

Sample	d_{PZT}	f_r **(Hz)**	Δf	Q_m	β	ζ
Fe/PZT/Fe	**1.4** μ**m**	63153	258091	0.245	1.03x10^{-5}	2.04
	2.0 μ**m**	58312	219864	0.265	1.03x10^{-5}	1.89

3.2.1.4 Magnetic Properties

In order to understand the magnetodielectric coupling, magnetocapacitance and magnetoimpedance of the heterostructures were measured at room temperature. The samples were subjected to varying magnetic field with a strength up to 2 T. At specific ranges, dielectric measurements were done and compared to

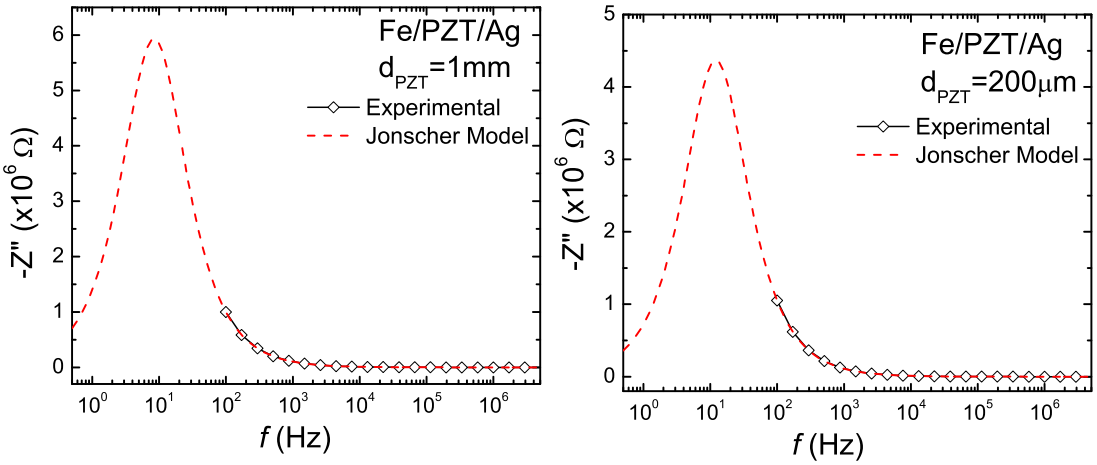

Figure 3.13: Frequency dependent reactance (Z'') of Fe/PZT/Ag (a) d$_{PZT}$=1.00 mm and (b) d$_{PZT}$=200 μm.

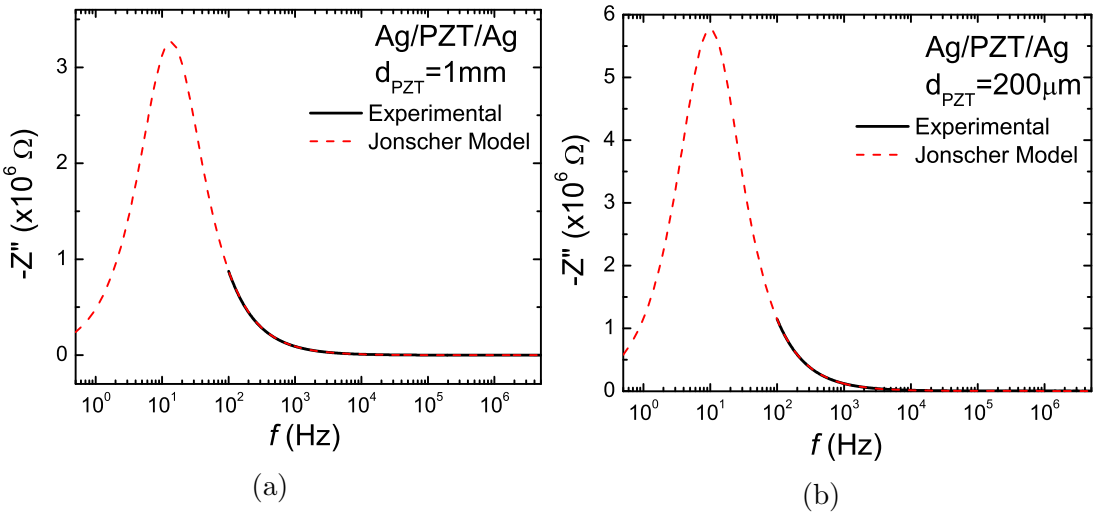

Figure 3.14: Frequency dependent reactance (Z'') of Ag/PZT/Ag (a) d$_{PZT}$=1.00 mm and (b) d$_{PZT}$=200 μm.

each other to determine a difference through the magnetic range. The magneto-capacitance was obtained using Equation 2.33. Similarly, all the magneto related measurements by percentage were calculated using the same equation.

Figure 3.15 show the magnetocapacitance for sample Fe/PZT/Fe with PZT thickness of 1.00 mm at specific frequencies in forward and reverse magnetic

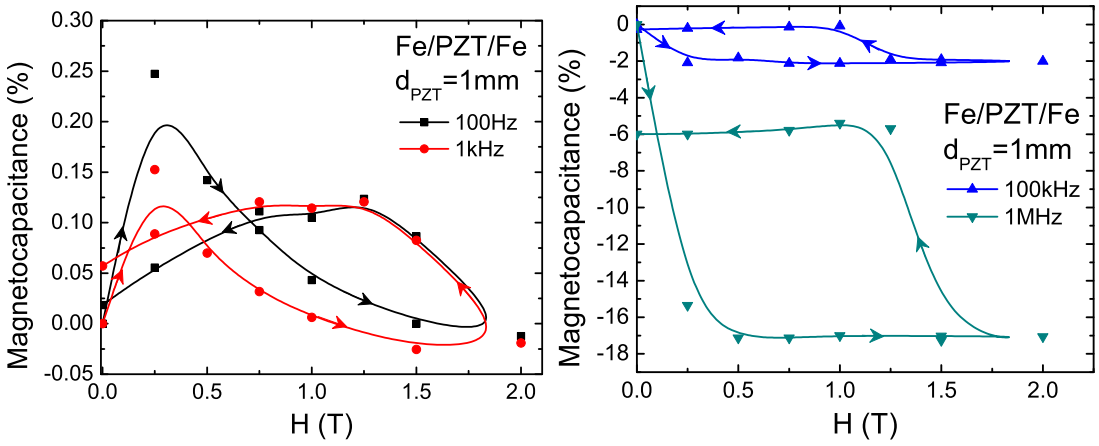

Figure 3.15: Magnetocapacitance of Fe/PZT/Fe with d_{PZT}=1.00 mm at frequencies (a) 100 Hz and 1 kHz, and (b) 100 kHz and 1 MHz.

field (0-2 T) sweeps. As can be seen in Figure 3.15a, the magnetocapacitance is very low for these frequencies (100 Hz and 1 kHz), only reaching a maximum of 0.15-0.25% and a remanent of 0.02-0.05%. On the other hand, the frequencies of 100 kHz and 1 MHz in Figure 3.15b show a higher result. For 100 kHz, it reaches 2% and almost no remanent value back at 0 T. At 1 MHz, it reaches a maximum of almost 18% and sustains a remanent of 6%. At this frequency, it is more noticeable since it is close to the relaxation frequency.

Figure 3.16 show the magnetocapacitance of sample Fe/PZT/Ag with PZT thickness of 1.00 mm in the same conditions as previous samples of Fe/PZT/Fe. In Figure 3.16a, it is observable that the magnetocapacitance reaches a maximum of approx -0.4% for both 100 Hz and 1 kHz, and -0.7% at 100 kHz. It is higher compared to the Fe/PZT/Fe sample. The remanent magnetocapacitance is at approximately the same as the maximum for each frequency. This means that the sample remains magnetized even after reducing the magnetic field applied. In Figure 3.16b, we observe that for 1 Mhz the magnetocapacitance is higher comparable with the lower frequencies, were it reaches up to almost -5% and has

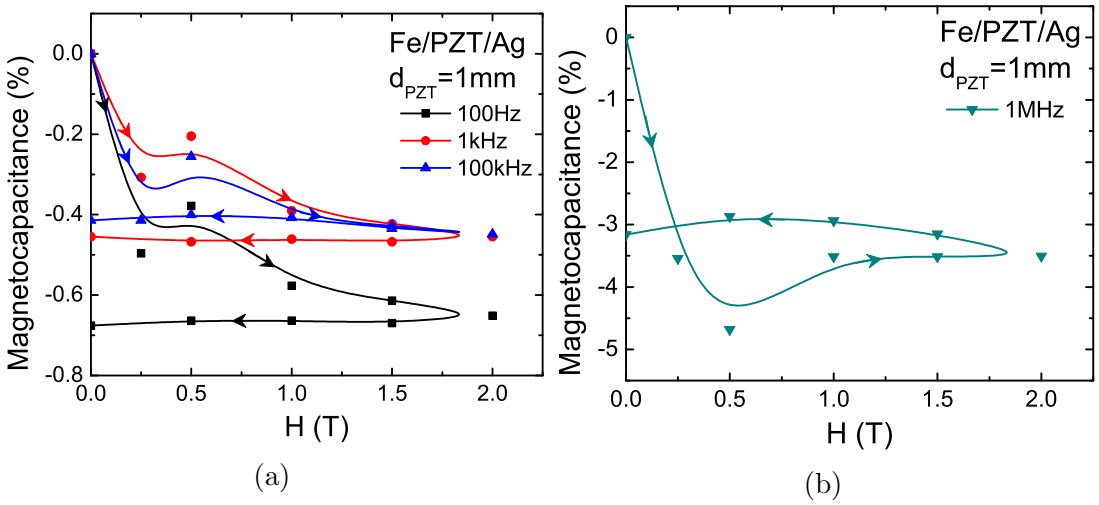

Figure 3.16: Magnetocapacitance of Fe/PZT/Ag with d_{PZT}=1.00 mm at frequencies (a) 100 Hz and 1 kHz, and (b) 100 kHz and 1 MHz.

a remanence of -3%. From

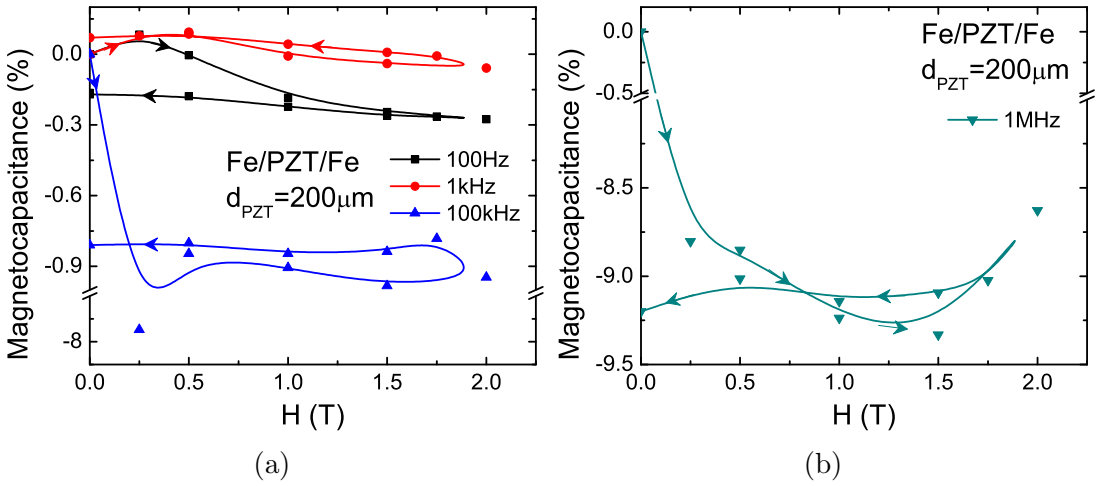

Figure 3.17: Magnetocapacitance of Fe/PZT/Fe with d_{PZT}=1.00 mm at frequencies (a) 100 Hz, 1 kHz, 100 kHz and (b) 1 MHz.

Figure 3.17 show the magnetocapacitance for sample Fe/PZT/Fe with PZT thickness of 200 μm at specific frequencies in forward and reverse magnetic field (0-2 T) sweeps. As can be seen in Figure 3.17a, the magnetocapacitance is very low for 100 Hz and 1 kHz, reaching a maximum of 0.07% and -0.16% respectively, were the remanent is close to the maximum. For 100 kHz, there is a big jump up

to almost -8% and then remaining between -0.8 to -0.9%. On the other hand, for 1 MHz in Figure 3.17b, a higher result is present. It reaches -9.3% and a sweep returning to a remanent value of -9.2%. Again, this is close to the relaxation frequency, where the sample has most activity.

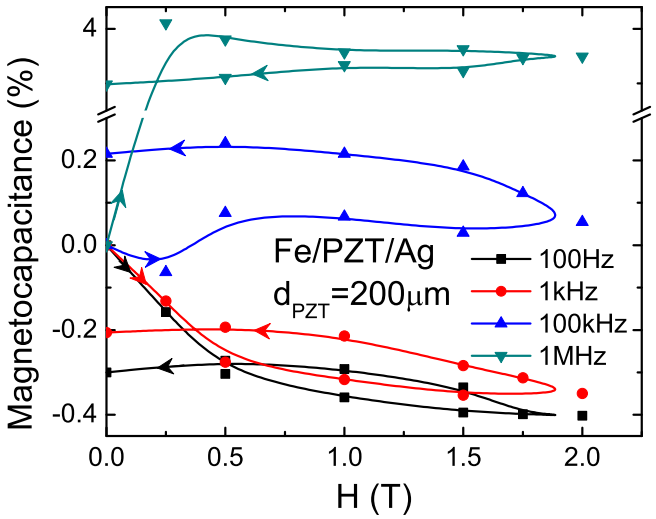

Figure 3.18: Magnetocapacitance of Fe/PZT/Ag with d_{PZT}=1.00 mm at frequencies (a) 100 Hz, 1 kHz, 100 kHz, and 1 MHz.

Figure 3.18 show the magnetocapacitance for sample Fe/PZT/Ag with PZT thickness of 200 μm at specific frequencies in forward and reverse magnetic field (0-2 T) sweeps. As can be seen, the magnetocapacitance is negative for 100 Hz and 1 kHz, reaching between -0.3% for 1 kHz and -0.4% for 100 Hz, were the remanent is at -0.3% for 100 Hz and -0.2% for 1 kHz. For the higher frequencies, we observe that it is of positive change. At 100 kHz it reaches 0.25% and remaining at close to 0.2%. For 1 MHz, as expected, it goes above at 4% and retains at 3.5%.

Comparing Fe/PZT/Fe and Fe/PZT/Ag, we observe that when the two conductive plates are magnetic, we have higher magnetocapacitance for the higher frequencies than when there is only one magnetic plate present. On the other

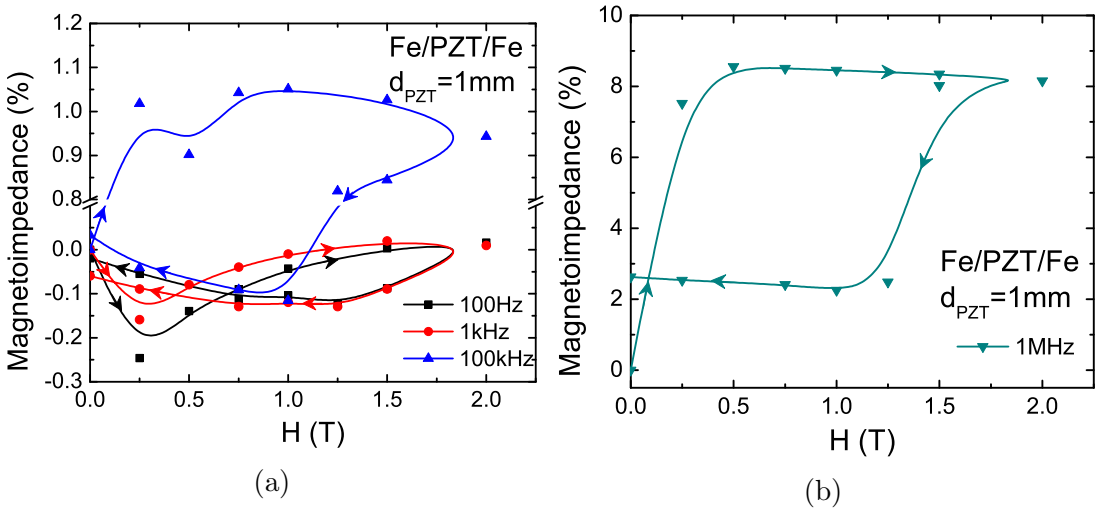

Figure 3.19: Magnetoimpedance of Fe/PZT/Fe with d_{PZT}=1.00 mm at frequencies (a) 100 Hz, 1 kHz, 100 kHz and, (b) 1 MHz.

hand, the thinner 200 μm sample has higher percent of magnetocapacitance at lower frequencies.

To establish the existence of magnetodielectric coupling, frequency dependent magnetoimpedance measurements were carried out at room temperature. As shown in Figures 3.19 and 3.20, we observe the magnetoimpedance of both samples Fe/PZT/Fe and Fe/PZT/Ag with PZT thickness of 1.00 mm. Both show decent magnetoimpedance for the frequency range of 1 MHz. This can indicate that there is a present magnetodielectric coupling, but not very large. Figure 3.19a show the frequency range of 100 Hz and 1 kHz for the Fe/PZT/Fe sample, having a similar pattern and very low magnetoimpedance percentage reaching in the negative 0.2-0.3% and returning to almost 0. Similar with 100 kHz, were this one reaches a higher positive 1.05% but returns to 0, meaning almost no remanent magnetic order. For the 1 MHz range, at Figure 3.19b, we see higher magnetoimpedance, reaching almost 9%, but falling back and having a remanence of almost 3%. For sample Fe/PZT/Ag, we see in Figure 3.20, were the highest magnetoimpedance is reached by 1 MHz range up to 2.6% and main-

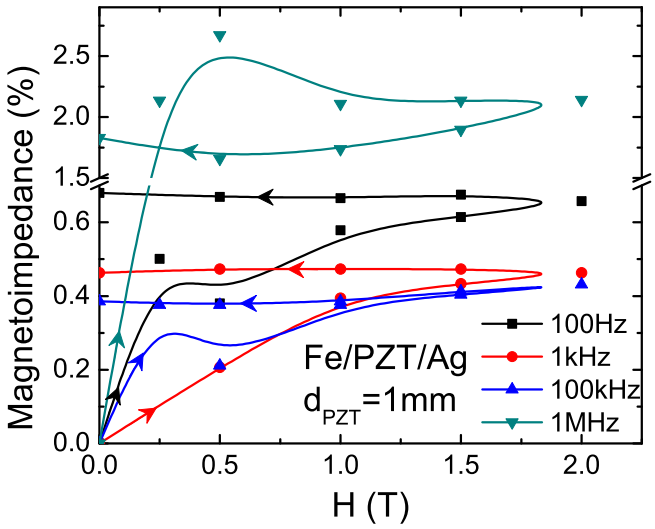

Figure 3.20: Magnetoimpedance of Fe/PZT/Ag with d_{PZT}=1.00 mm at frequencies 100 Hz, 1 kHz, 100 kHz, and 1 MHz.

taining remanent magnetization for all frequencies with 100 Hz being at 0.7%, 1 kHz at 0.46%, 100 kHz at almost 0.4% and 1 MHz at 1.8%.

Figure 3.21 show the magnetoimpedance of both samples Fe/PZT/Fe and Fe/PZT/Ag with PZT thickness of 200 μm. On Figure 3.21a show that, again, at the 1 MHz range we have higher magnetoimpedance, reaching above 5%. The remanent magnetization stays at that range as well. For the remaining lower frequencies, we see that the highest reaches 1.8% for 100 Hz, and 1 kHz and 100 kHz are lower between 0.5-0.3%. The show remanent magnetization at 0.5% for 100Hz, and approximately 0.17% for both 1 kHz and 100 kHz. Figure 3.21b show the magnetoimpedance of Fe/PZT/Ag sample, where the highest is obtained at 1 MHz for 2.7% and a remanent of 1.8%. At 100 Hz, the highest is the same as the remanent, being at 0.68%, at 100 kHz, having the same pattern, at 0.4%. For 1 kHz is different, rising and returning to a lower percentage for the remanent. The highest was 0.47% and the remanent at 0.27%. All the sam-

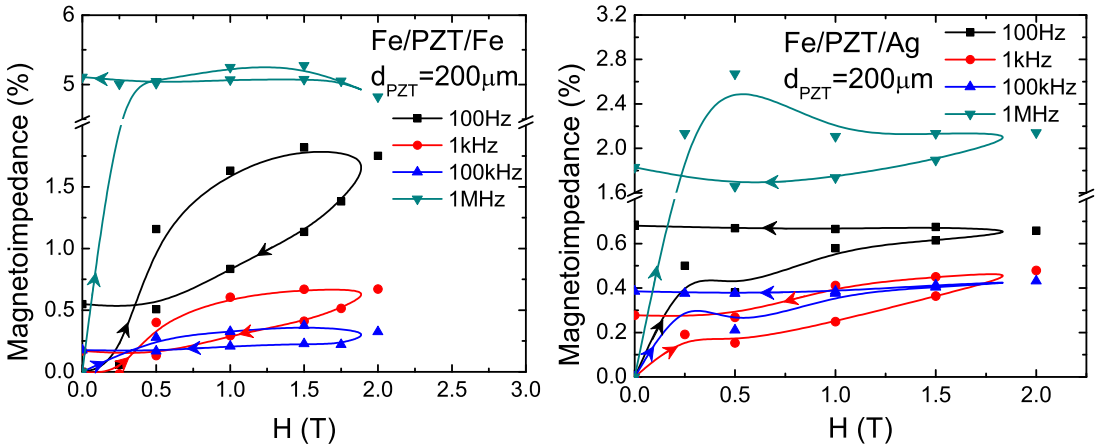

Figure 3.21: Magnetoimpedance of (a) Fe/PZT/Fe and (b) Fe/PZT/Ag with d_{PZT}=200 μm at frequencies 100 Hz, 1 kHz, 100 kHz and, 1 MHz.

ples show similarities that at higher frequencies there are bigger changes by the applied magnetic field. This information show that there is magnetodielectric coupling.

3.2.2 Thin Samples

These samples where put through a AFM/Profilometer to determine their thickness. The measured average thickness of two selected samples where of 1.4μm and the thicker one being of 2μm. The thickness achieved is "100" times thinner than the commercially obtained samples of 200μm. Following suit as with the samples done before, the SPL deposited Fe/PZT/Fe samples where subjected to the same measurements and conditions. Dielectric measurements where done in the range of 100Hz to 5GHz with a magnetic field presence from 0 T up to 2 T and back down.

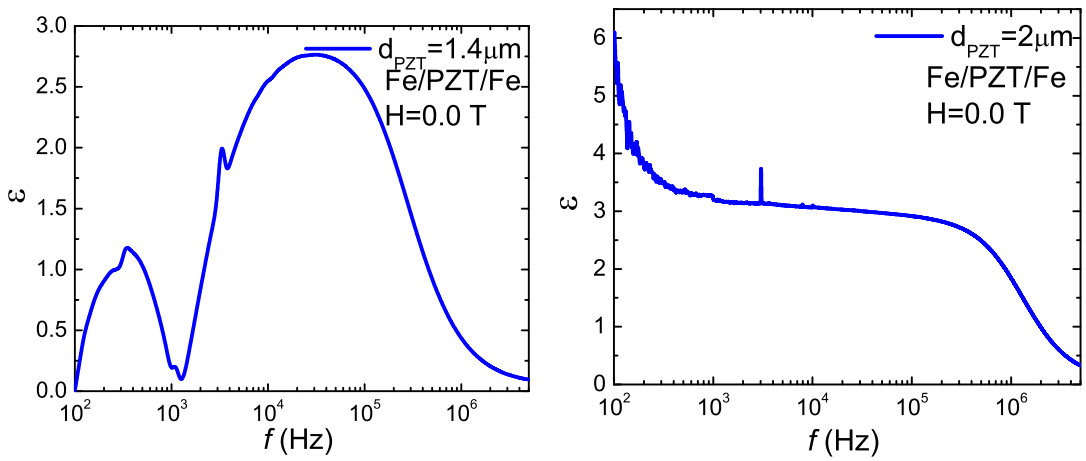

(a) (b)

Figure 3.22: (a) Dielectric permittivity of Fe/PZT/Fe with d_{PZT}=1.4μm and (b) Fe/PZT/Fe with d_{PZT}=2μm.

3.2.2.1 Dielectric Permittivity

From Figure 3.22a we can observe the dielectric response of the samples. It is interesting to note that the sample with thickness d_{PZT}=1.4μm has a very different behavior than others in the range of 100Hz to 33kHz. After this range, the sample behaves the same as others, even close to the same magnitude. This can be with respect to the roughness, how thin, and delicate the PZT layer is. The samples did not show a current short between the plates, which means that the top and bottom plates had no contact either through or alongside the edge of the layer. It was a true capacitor with an insulating layer in between. Despite the erratic behavior in the low frequency range, the diagrams for the real and complex dielectric permittivity show interesting results.

The sample with ferroelectric layer of thickness d_{PZT}=2.0μm show true dielectric behavior as a ferroelectric, this can be observed in Figure 3.22b. Here we can observe that where the curve has a fair flat area, has an average value of 3. The sample of thickness d_{PZT}=1.4μm has the range of 100Hz to 33kHz fairly

erratic, but the rest has very similar value as the sample of 2.0μm. Meaning that they share a similar dielectric permittivity intensity.

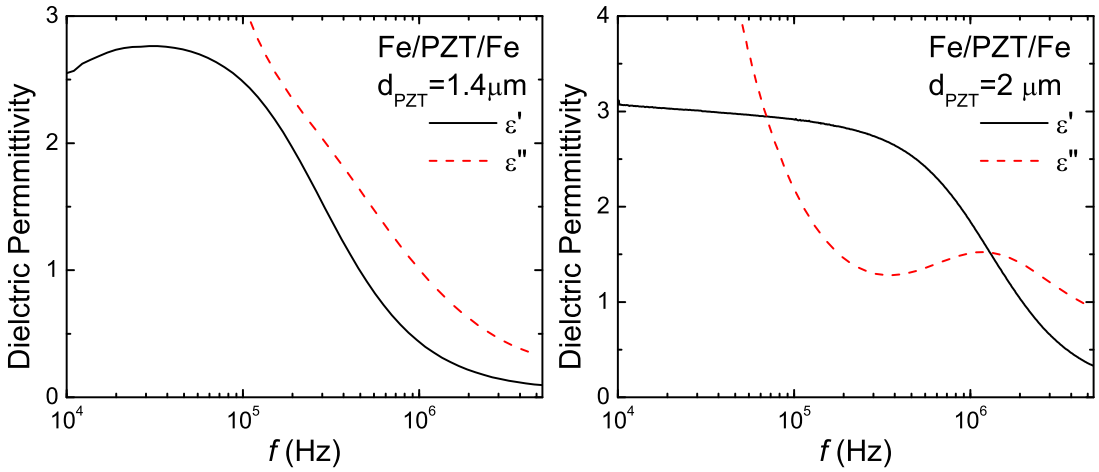

(a) (b)

Figure 3.23: Complex permittivity of Fe/PZT/Fe thin samples illustrating the real and imaginary parts.

Dividing the complex permittivity from its real and imaginary parts, we truly observe the dielectric response. Figure 3.23 demonstrates the behavior of the real and imaginary parts of both samples. The sample with PZT thickness of 1.4μm had interference at lower frequencies for the real part, but, at the frequency range of 18kHz, we see a drop. This is accompanied by a peak in the imaginary part, indicating that there is a relaxation process occurring. This relaxation occurs at the frequency 98kHz, with a bandwidth of 307kHz. Since the frequency range of the peak is between 34kHz and 1MHz it means that is dipolar relaxation. The 2μm sample is completely usable and we observe interesting behavior. The 2μm sample show that in the real part of the dielectric permittivity, that there are two drops. These determines that there are two relaxations. The relaxation can be determined from the imaginary part where we can observe one broad peak. Since the real part show two drops, it means that this peak in the imaginary part

is a composition of two peaks for each relaxation process. These peaks are in the same range for space-charge relaxation since it is <1 MHz. The peaks highest point determines the relaxation frequency and the frequency the relaxation time. These peaks are very close together, that is way it appears as if there is only one peak. This is more evident in other samples where the peak is broader, these will be explored in their chapters. From the Cole-Cole plot in Figure 3.24, we can obtain the relaxation time with the highest point of the semi-circle, this was τ=8.54x10^{-7} s.

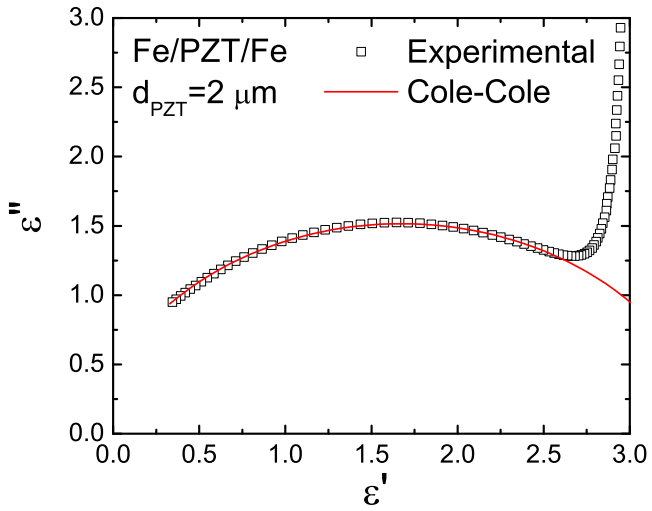

Figure 3.24: Cole-Cole diagram of 2 μm PZT Fe/PZT/Fe with real and imaginary parts of the dielectric permittivity and their relation with the frequency range.

3.2.2.2 Phase Angle and Dielectric Loss

From the phase angle information, we can determine how our capacitor can withstand the input frequency and voltage. A phase angle of 0°means that our material is behaving as a resistor. Both samples at low frequencies start as resistors, given that the bias voltage was of 1V, and that the sample is very thin, it behaves as a resistor, but at further frequencies it starts to shift towards the

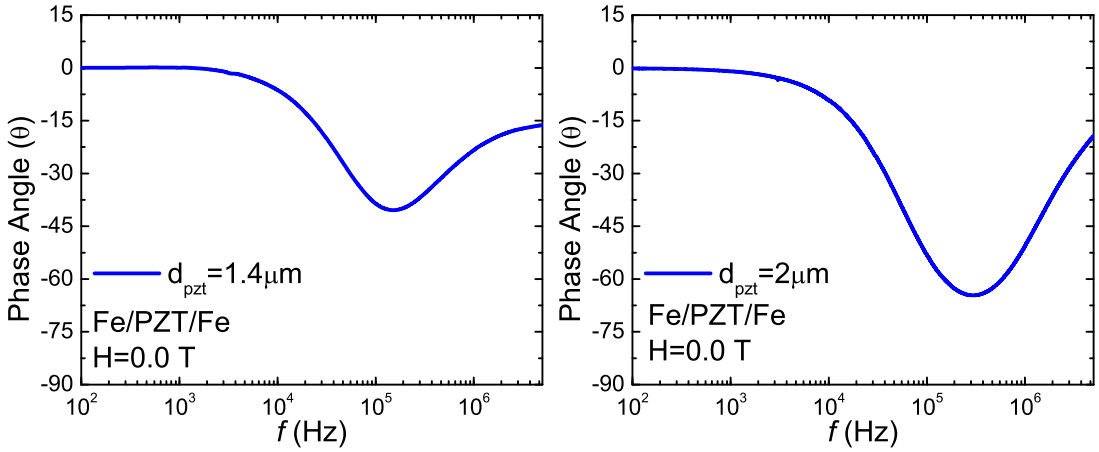

Figure 3.25: Phase angle of SPL deposited (a) d_{PZT}=1.4μm PZT thickness and (b) d_{PZT}=2μm with Fe/PZT/Fe configuration at 0T and room temperature in the frequency range of 100Hz to 5MHz.

negative side, reaching -40°. For it to be a full capacitor, it must reach -90°. This is shown in Figure 3.25. This means that it has high loss current, and this can be proved and observed further with the loss coefficient graph shown in Figure 3.26. Here we can observe that for both samples, from 100Hz to ∼6kHz, that there is high current loss. Where the phase angle approaches to the lower negative sides, towards -90°, we observe that the loss coefficient lowers closer to 0. Again, when we have lower, to no dissipation and current loss, we arrive to capacitors area, where there is energy storage. Still, these samples show some loss, since it never reaches 0 loss.

3.2.2.3 Impedance Spectroscopy

The impedance measurements offers a great spectrum of information of the samples, most data obtained are derived from the impedance of the sample. Here in Figure 3.27 we observe the sample's resistive behavior by impedance. Since these samples have a very thin thickness, we can see that there is a limit of

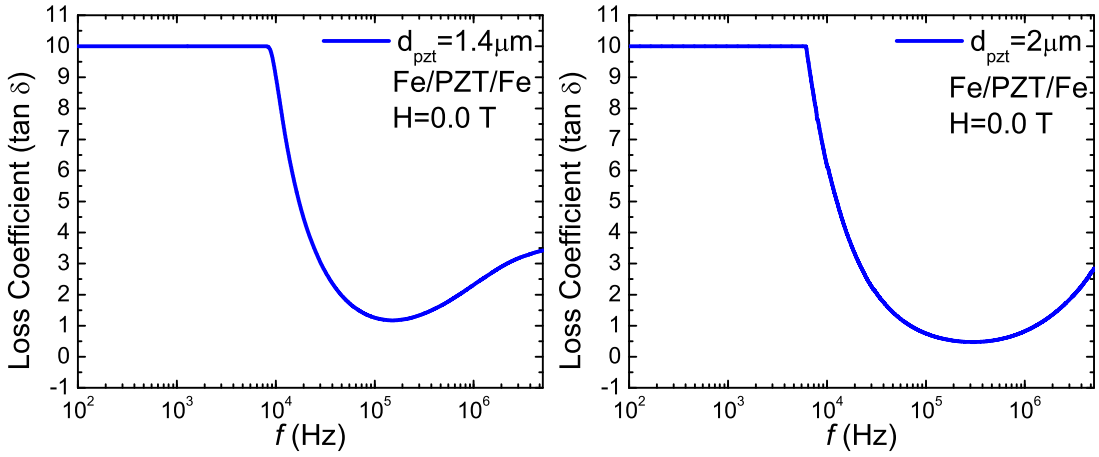

Figure 3.26: Loss Coefficient of SPL deposited (a) d_{PZT}=1.4μm PZT thickness and (b) d_{PZT}=2μm with Fe/PZT/Fe configuration at 0T and room temperature in the frequency range of 100Hz to 5MHz.

impedance on lower frequencies. This is where we see higher loss current. This is followed by normal exponential decay. The impedance is composed by both real and imaginary parts, these can be observed on Figure 3.27. Here on Figure 3.27a we see that the sample with thickness of 1.4μm, the real and imaginary parts do not intersect. This means that the relaxation does not have a strict Debye response. Where on the sample with thickness of 2μm (Figure 3.27b), we can observe that the real and imaginary part do intersect. It is important to note that the peak of the imaginary part is intersected close to the highest point and center by the real part slope. For a true Debye response, this occurs exactly in the center. Utilizing the Jonscher model we can obtain all the important information of the equivalent circuitry. This information is present in Table 3.4, where the resistance and capacitance of the grains and grain boundary is shown.

Figure 3.28 show the Nyquist plots for the samples Fe/PZT/Fe with thickness d_{PZT}=1.4 μm (3.28a), and d_{PZT}=2.0 μm (3.28b). These samples, since the imaginary peak is present within the measured spectra, we can obtain a Nyquist

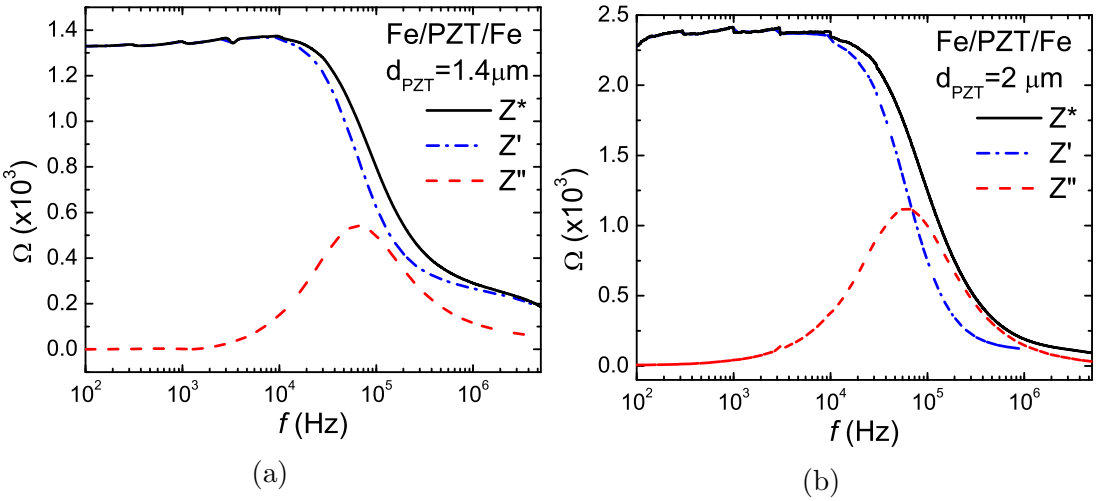

Figure 3.27: Complex impedance of SPL deposited (a) d_{PZT}=1.4μm PZT thickness and (b) d_{PZT}=2μm with Fe/PZT/Fe configuration at 0T and room temperature in the frequency range of 100Hz to 5MHz with the real (Z') and imaginary (Z") parts.

plot, which in turn enables us to simulate an equivalent circuit and fit to the experimental data. After simulating the circuit described in Figure 5.13, and within Figure 3.28, we obtain information and values for the circuit of the grain and grain boundary. This is corroborated with the Jonscher model with Equation 5.1, and obtain equal results. For both samples, we can observe that the semi-circle doesn't start at 0, this means that there is a starting resistance which can be attributed to the contacts between the sample and the measuring connection. For the 1.4μm sample, the connection barrier resistance is 180 Ω, and for the 2μm sample is 90.5 Ω. The solid line in Figure 3.28 shows simulated fit of equivalent circuit to the data using a an electrochemical impedance spectroscopy (EIS) spectrum analyser software [5].

3.2.2.4 Magnetic Properties

In order to understand the magnetodielectric coupling, magnetocapacitance and magnetoimpedance of the thin film heterostructures were measured at room

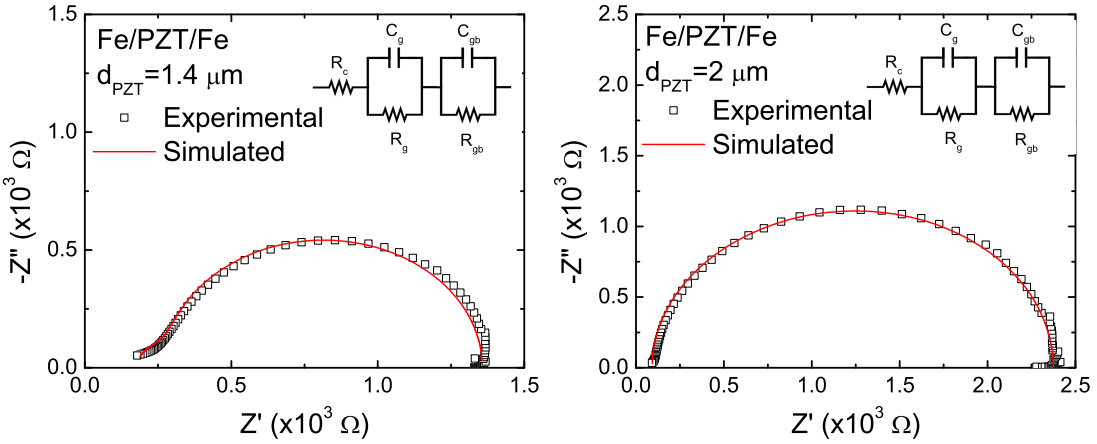

Figure 3.28: Real and imaginary parts from the impedance graphed in a Nyquist plot of SPL deposited (a) d_{PZT}=1.4μm PZT thickness and (b) d_{PZT}=2μm with Fe/PZT/Fe configuration at 0T and room temperature in the frequency range of 100Hz to 5MHz. The Jonscher model is fitted and the equivalent circuit presented.

Table 3.4: Important information from impedance spectroscopy utilizing Equation 5.1 and Nyquist plot for Fe/PZT/Fe thin film samples.

Sample	$\mathbf{R}_g$ **(Ω)**	$\mathbf{R}_{gb}$ **(Ω)**	$\mathbf{C}_g$ **(F)**	$\mathbf{C}_{gb}$ **(F)**	$\boldsymbol{f}_{peak}$ **(Hz)**
1.4 μm	1078	102.7	2.20x10^{-9}	1.01x10^{-9}	63153.3
2.0 μm	1928	361	1.49x10^{-9}	4.21x10^{-9}	58312.3

temperature. The samples were subjected to varying magnetic field with a strength up to 2 T. At specific ranges, dielectric measurements were done and compared to each other to determine a difference through the magnetic range. The magnetocapacitance was obtained using Equation 2.33. Similarly, all the magneto related measurements by percentage were calculated using the same equation.

Figure 3.29 show the magnetocapacitance for sample Fe/PZT/Fe with PZT thickness of 2.0 μm at specific frequencies in forward and reverse magnetic field (0-2 T) sweeps. As can be seen, the magnetocapacitance is significant. We

Table 3.5: Information gathered by the imaginary part of the impedance (Z") including resonance frequency (f_r), resonance bandwidth (Δf), Quality factor (Q_m), damping coefficient (β), and damping ratio (ζ) of Fe/PZT/Fe with both thicknesses.

Sample	d_{PZT}	f_r **(Hz)**	Δf	Q_m	β	ζ
Fe/PZT/Fe	**1.4 μm**	63153	258091	0.245	1.03x10^{-5}	2.04
	2.0 μm	58312	219864	0.265	1.03x10^{-5}	1.89

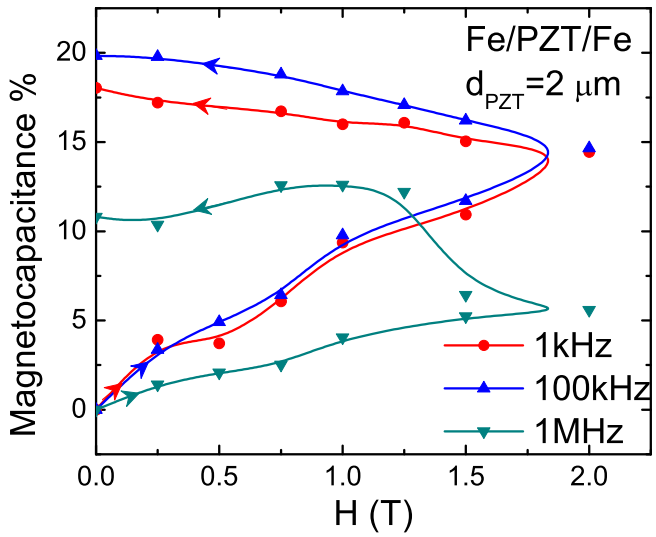

Figure 3.29: Magnetocapacitance of Fe/PZT/Fe with d_{PZT}=2.0 μm at frequencies 1 kHz, 100 kHz, and 1 MHz.

observe an increment up to almost 20%. What is interesting to note is that it has an increment on the whole sweep, leaving a remanent. This prove to be a very useful sample for device applications. Part of this can be explained since the ferroelectric layer, being a thin film, is significantly smaller than the ferromagnetic layers. In this case, the magnetic retention is permanent and visible.

To establish the existence of magnetodielectric coupling, frequency dependent magnetoimpedance measurements were carried out at room temperature.

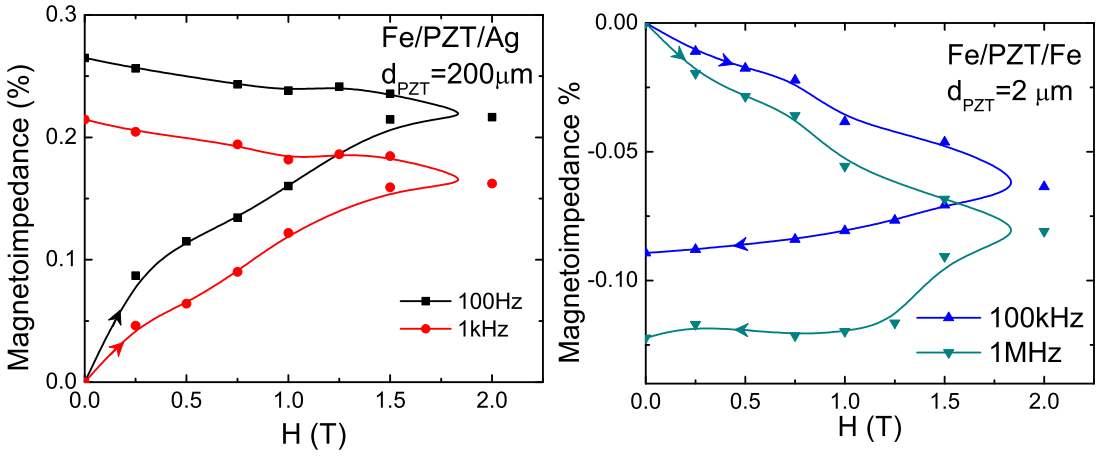

Figure 3.30: Magnetocapacitance of Fe/PZT/Fe with d_{PZT}=2.0 μm at frequencies (a) 100 Hz and 1 kHz, and (b) 100 kHz and 1 MHz.

As shown in Figure 3.30, we observe the magnetoimpedance of the thin film Fe/PZT/Fe sample divided between (3.30a) 100 Hz, 1 kHz, and (3.30b) for 100 kHz and 1 MHz. This separation is needed since for Figure 3.30a, we see a positive magnetoimpedance, and for Figure 3.30b, a negative magnetoimpedance. Similar to the behavior with the magnetocapacitance, the magnetoimpedance for all frequencies is fairly linear in their increments and decrease. For the lower frequencies we see a rise to 0.26% for 100 Hz and 0.21% for 1 kHz. In the higher frequencies we see that it is -0.09% for 100 kHz and -0.12% for 1 MHz. It is evident that there is a magnetodielectric coupling present. This samples show better this evidence, thanks to their linear increments and higher magnetic remanent values.

3.3 Summary

There are vast differences in magnitude when we compare the bulk samples (1.00 mm and 200 μm) with the thin film samples (1.4 μm and 2.0 μm). It is

evident that the thickness plays a huge factor, specially with the resistance and capacitance of the sample. The best result for magnetoelectric coupling can be observed for the thin film samples. this makes then good for device applications, specially the fact that they are made by spray pyrolysis, a very cost effective alternative for thin film growth.

References

[1] Yarmarkin, V. K., Teslenko, S. P., Dielectric relaxation in thin-film metalPZT-ferroelectricmetal structures, Phys. Solid State 40, 17381741 (1998)

[2] Swagatika Dash, R. Padhee, Piyush R. Das & R.N.P. Choudhary, Dielectric and impedance spectroscopy of (Bi0.5Li0.5)(Fe0.5Nb0.5)O3 multiferroics, Phase Transitions, 87:3, 223-235 (2014)

[3] Jonscher AK. The universal dielectric response. Nature. 1977;267:673679.

[4] Bondarenko A. S., Ragoisha G. A. In Progress in Chemometrics Research, Pomerantsev A. L., Ed.; Nova Science Publishers: New York, pp. 89102 (2005)

[5] Y. Zhou, D. Maurya, Y. Yan, G. Srinivasan, E. Quandt, S. Priya, Self-Biased Magnetoelectric Composites: An Overview and Future Perspectives. Energy Harvesting and Systems. 3. 10.1515 (2015)

[6] Jia Y, Zhou W, Ma K, Liu Y. Enhanced Magnetoelectric Effect in Permendur/Pb(Zr0.52Ti0.48)O3 Laminated Magnetostrictive/Piezoelectric Composite. Applied Sciences. 5(3):587-594. (2015)

Chapter 4

Co/PZT/Co Multiferroic Heterostructures

This chapter will discuss all the capacitor samples that has cobalt as the ferromagnetic layer. The measurements discussed will include the dielectric properties, impedance spectroscopy, and magnetic properties. These samples have the shape of Co/PZT/Co, Co/PZT/Ag, and Ag/PZT/Ag as reference. The chapter is divided in two parts, where the first is the bulk samples that include thicknesses of d_{PZT}=1.00 mm and d_{PZT}=200 μm; and the second part of the chapter being the thin samples which include thicknesses of d_{PZT}=3.8 μm and d_{PZT}=4.8 μm. Dielectric measurements show that all samples share ferroelectric behaviour. The bulk samples are commercially available PZT substrates of which cobalt was sputtered on top and bottom to make a simple spin capacitor shape. Impedance spectroscopy show that the 1.00 mm thick PZT samples do not exhibit a peak in the imaginary part of the impedance, since these are too thick and the resonance frequency is overly damped and into the lower frequencies, which are out of the measured range. On the other hand, the 200 μm samples do exhibit a peak on the imaginary part of the impedance. The imaginary peaks are then extrapolated by the fitting of the circuit equation 2.32 of the Jonscher model. The phase angle of the d_{PZT}=1.00 mm samples show that it acts as a capacitor at lower frequencies until it reaches a resonant frequency, whereas the d_{PZT}=200 μm samples show that it starts as almost a resistor, since it is close to 0°and has high dissipation visible in the loss coefficient measurements, meaning

that there is leakage current. This is evident since the sample is 5 times thinner. Furthermore, the thin samples where both SPL deposited PZT samples, show the same behaviour where the phase starts close to 0°at lower frequencies, and falls to almost -90°. The dielectric behaviour is apparent in these samples as well, showing very similar shape as the bulk but at a lower magnitude.

4.1 Experimental Details

PZT substrates of d_{PZT}=1.00 mm with area of 1.00 cm x 1.00 cm and d_{PZT}=200 μm with an area of 3.00 mm x 1.00 mm were obtained and deposited ferromagnetic cobalt contacts on top and bottom by sputtering, giving them simple capacitor shape with ferromagnetic/ferroelectric/ferromagnetic configuration as shown in Figure 3.1a on the previous chapter. These are the bulk samples. Furthermore, thinner samples were made using Spray Pyrolysis to deposit PZT onto a copper laminate that had a top layer of cobalt deposited to make the bottom contact, and after the SPL deposited PZT, a top cobalt contact was deposited to achieve the same capacitor structure as the bulk samples so the measuring devices and methods are equal.

The thin samples where put through a AFM/Profilometer to determine the PZT thickness. The measured average thickness of two selected samples where of 3.8μm and the other of 4.8μm. The thickness achieved is close to 100 times thinner than the commercially obtained samples of 200μm. Following suit as with the samples done before, the SPL deposited Cu/Co/PZT/Co samples where subjected to the same measurements and conditions. Dielectric measurements where done for both bulk and thin samples in the range of 100Hz to 5GHz with a magnetic field presence from 0 T up to 2 T and back down.

4.2 Results and Discussion

4.2.1 Bulk Samples

Various frequency dependent dielectric measurements where carried out for the samples containing the ferromagnetic material of cobalt. Six samples where made that consist of three different capacitor configurations (Co/PZT/Co, Co/PZT/Ag, and Ag/PZT/Ag as reference), with two different PZT substrate thicknesses (d_{PZT}=1.00mm and d_{PZT}=200μm). The dielectric measurements done where: capacitance (which in turn can be translated to dielectric permittivity), phase angle, impedance, loss coefficient, loaded Quality Factor, magnetocapacitance, and magnetoimpedance (which is dependent on magnetic fields). The range of frequencies used where from 100 Hz up to 5 MHz. The magnetocapacitance measurements where done with an external applied magnetic field with maximum strength of 2 T. With the complex impedance information, divided by its real and imaginary components, the reference circuit was calculated for those samples using a Nyquist plot that show a clear peak in the imaginary part and corroborating this with a fitted model equation.

4.2.1.1 Dielectric Permittivity

The samples where subjected to capacitance measurements for the frequency range of 100 Hz up to 5 MHz. As well, the samples where introduced to a magnetic field for a range from 0 T up to 2 T and back down to 0 T, this gives us the relation in the ferroelectric and ferromagnetic coupling and the reminiscence of it. To obtain the dielectric permittivity of each sample, their capacitance measurement was multiplied by a factor containing the information of the ferromagnetic contact area, thickness of the PZT layer and dielectric constant of

vacuum. The Equation 2.12 is in Section 2.2.2.1.

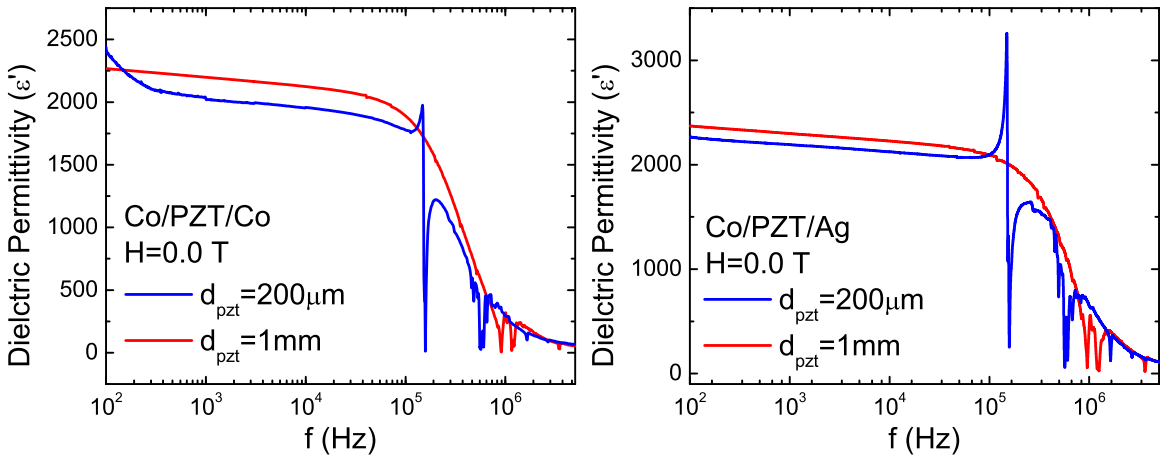

Figure 4.1: Dielectric permittivity of (a) 1mm PZT and 200μm with Co/PZT/Co configuration and (b) 1mm PZT and 200μm with Co/PZT/Ag at 0T and room temperature.

Figure 4.1a show the frequency variation of dielectric permittivity for Co/PZT/Co with both 1mm and 200 μm. We can observe the ability of the sample to store energy as a capacitor and its stability within the frequency range of 100 Hz up to 10^5 Hz. The dielectric permittivity of this range is within 2400 max down to ≈2000. This is a bit higher than the typical range for dielectric constant values for bulk ceramics [2]. The samples decay at an approximate rate of 0.002 ϵ/Hz. At higher frequencies than 10^5 Hz, we find that there is a more erratic behaviour, meaning that the samples loose stability and reach a resonant frequency range. For the sample of Co/PZT/Co d_{PZT}=1.00 mm, it is observable the drop in dielectric permittivity starting at ≈10^5 Hz, same with the d_{PZT}=200 μm sample. This is typical ferroelectric behaviour. These samples show inverse peaks at certain frequencies within the frequency range of 10^5 Hz up to 4MHz. These are moments where the leakage current is very high. At 160 kHz, the Co/PZT/Co 200 μm sample show a large resonance peak, which

is an upward peak followed by a large inverse peak, this can be better observed in Figure 4.2b. This is followed by a set of peaks in the range of 450 kHz to 890 kHz. The 1.00 mm sample show more stability, where it doesn't have the resonance peak, until ≈820 kHz where two inverse peaks are present.

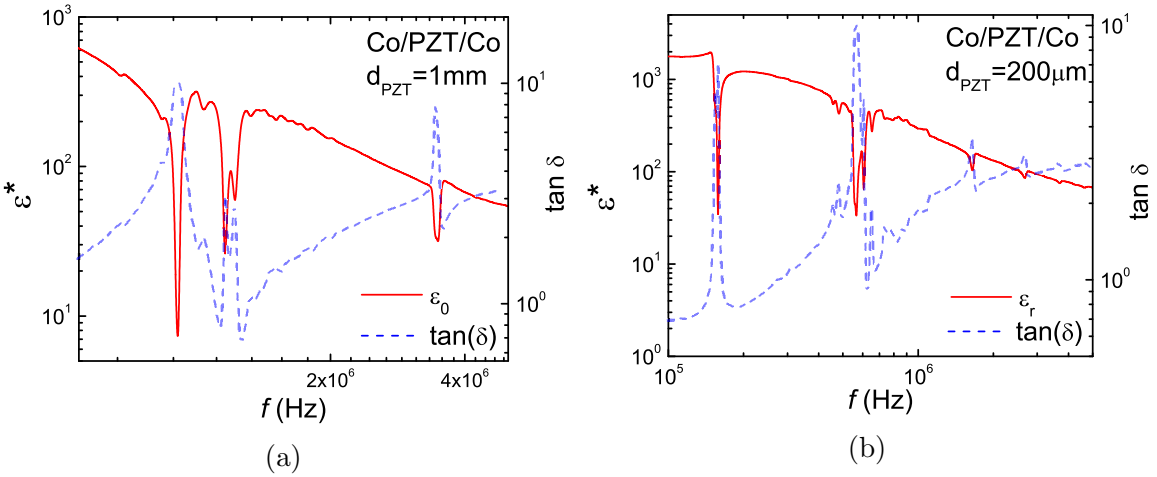

Figure 4.2: Comparison of the dielectric permittivity with loss coefficient of Co/PZT/Co for (a) d_{PZT}= 1.00 mm and (b) d_{PZT}=200μm at 0T and room temperature.

Figures 4.2 and 5.4 show the relationship of the dielectric permittivity with the loss coefficient. Since the loss coefficient is directly related to the capacitance, we can note that where there is a spike in the dielectric permittivity, there is a inverse spike in the loss coefficient, and the opposite is equal, where there are peaks in the loss coefficient, there are inverse peaks in the dielectric permittivity. This tells that where the capacitance drops, there is a loss, or a leakage of current. In an ideal resonator, the power dissipation is zero, whereas in a 'lossy' resonator, due to piezoelectric coupling, the power dissipation becomes large at resonance.

Dividing the dielectric permittivity by its complex components, being the real and imaginary parts, we can observe if there are relaxations and/or resonances present in the frequency range. For the d_{PZT}=1.00mm sample, shown in Figure **??**, we observe that the real part closely resembles the whole complex di-

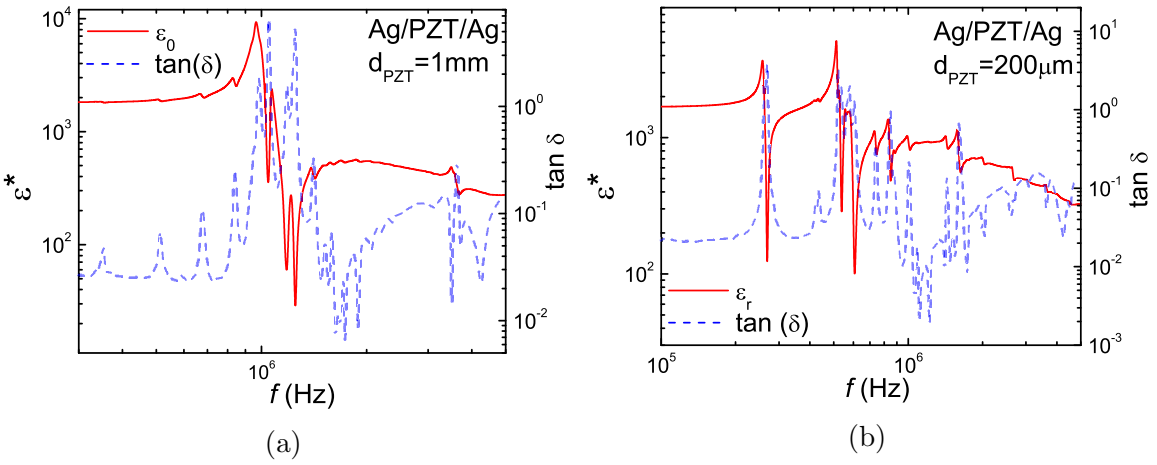

Figure 4.3: Comparison of the dielectric permittivity with loss coefficient of Ag/PZT/Ag for (a) d_{PZT}= 1.00 mm and (b) d_{PZT}=200μm at 0T and room temperature.

Table 4.1: Frequency of resonance and relaxation peaks in the imaginary part of Fe/PZT/Fe.

Co/PZT/Co	**d_{PZT}=1.00 mm**	**d_{PZT}=200 μm**
$\boldsymbol{f}_{peak}$	348 kHz	82 kHz
τ	2.87x10^{-6} s	1.21x10^{-5} s
Max Dielectric	1064	1472

electric permittivity, where there is one drop in magnitude, that is accompanied by a peak in the imaginary part. This is evidence of a relaxation process. This relaxation occurs at the frequency ≈260 kHz, where the imaginary peak is highest. This frequency range correspond to the dipole relaxation range, meaning that there is a relaxation of space-charge within the sample until this frequency, where it stops. We can determine that it is a stop in space-charge polarization because it falls within the range of $<$ 1 MHz. Followed, there are smaller resonance peaks at the range of 1MHz and ≈3 MHz. The resonance peaks are identifiable by their shape. These inverse peaks appear in pairs, we may determine that these are present because of the interface coupling between the ferroelectric and

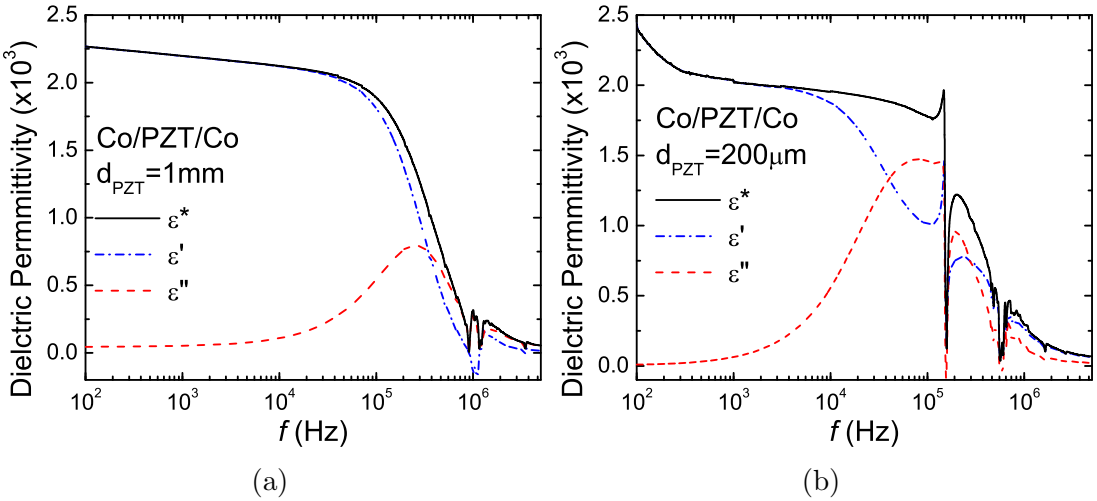

Figure 4.4: Complex dielectric permittivity comparison of (a) 1mm PZT and (b) 200μm of Co/PZT/Co with real and imaginary parts of the dielectric permittivity.

ferromagnetic layers, This can further be proved with the thin film samples and their relaxation peaks. Figure 3.7 is a Cole-Cole diagram of the d_{PZT}=1.00mm sample, where the 'X' axis is the real part and 'Y' axis the imaginary part of the dielectric permittivity, of the relaxation process. Here we can observe that it has a fairly semi-circle shape and a "tail" at the right side. This tail indicates that there are losses in the system, and since it is very low on the 'Y' axis, it means that the losses are not too high. These figures show that there is at least two relaxation processes, specially since the semi-circle is wide on the 'X' axis. Table 3.1 show the frequency of the relaxation at the peak of the imaginary part, and the relaxation time 'τ'. This value contains both relaxation times within. This value is close to reported ones of the range of x^{-5}s [1].

The Figure 4.4b show the real and imaginary components of the dielectric permittivity for the 200μm sample. This sample behaves differently than the 1.00mm sample. The real part show a fast decline from 100Hz, up to ≈340 Hz, followed by a steady decline until it rises into a resonance peak, where there is a sharp rise and fall, then return to unity. This top peak is at 147kHz, and

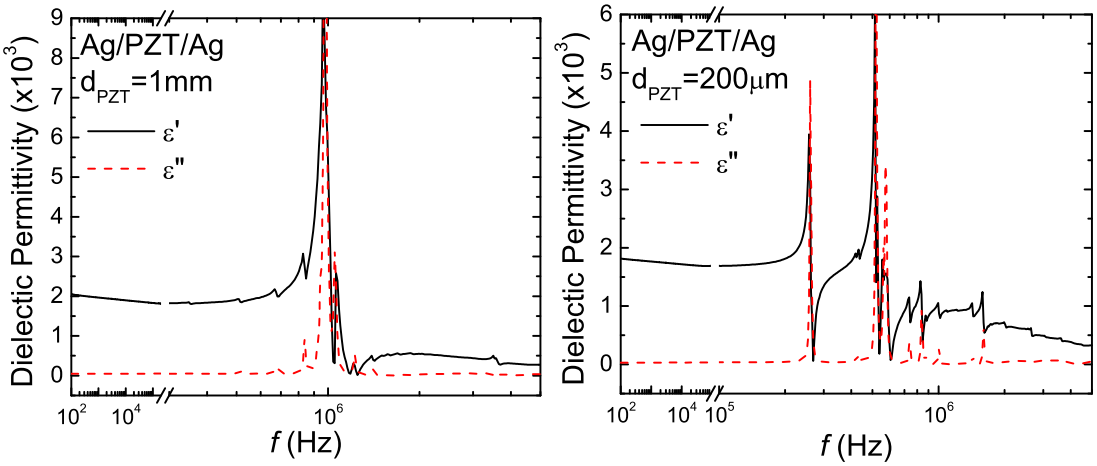

Figure 4.5: Complex dielectric permittivity comparison of (a) 1mm PZT and (b) 200μm of Ag/PZT/Ag with real and imaginary parts of the dielectric permittivity.

bottom at 156kHz. in the middle we see the imaginary peak corresponding to this resonance at 151kHz. The drop of the real part, and rise in the imaginary, suggests that there is a relaxation happening. We can observe that the mean curve for ϵ" follows a broad peak, having the resonant peak wedged almost in the middle. Unfortunately, since the real/imaginary diagram show a very rare behaviour, the Cole-Cole plot show a very erratic collection of curves. At least half a circle is observed, determining that there is relaxation, but due to the resonance, the signal becomes too erratic.

4.2.1.2 Phase Angle and Dielectric Loss

The angle of the phase demonstrate the relationship between the real and imaginary parts of the material and its electrical properties. This relation between the real and imaginary brings the relationship of the loss and storage properties. The phase is the ratio between real and imaginary, where the dielectric loss coefficients represents the electrical loss due to dissipation of energy. Figure 4.7 show the dielectric loss coefficient of samples Co/PZT/Co with both

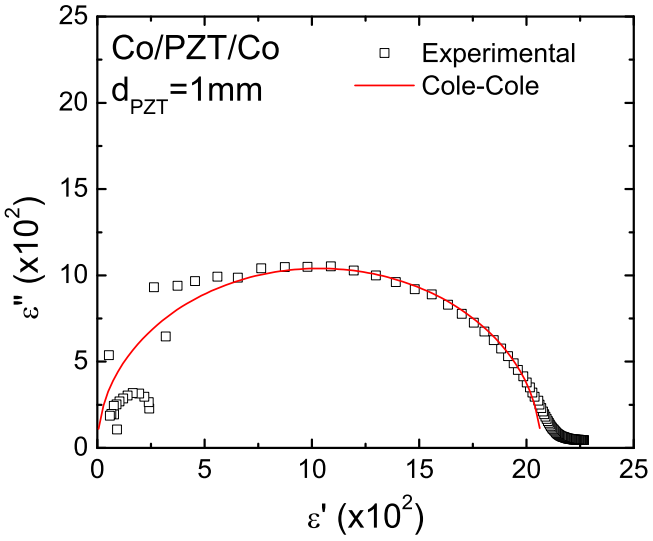

Figure 4.6: Cole-Cole diagram of 1mm PZT with real and imaginary parts of the dielectric permittivity and their relation with the frequency range.

thicknesses (4.7a) and Co/PZT/Ag with both thicknesses (4.7b). Co/PZT/Co with thickness of 1.00mm show a fair stableness up until 10^5 Hz, where it starts to rise until reaches a peak at ≈1 MHz. On the other hand, the 200μm sample starts with a loss of approximately 10, which is the maximum, then lowers to $\tilde{0}.12$ at 10^4 Hz, and rise again to a sharp peak at 156kHz. The mean path is similar to the 1.00mm sample, with the difference at low frequencies. This means that at 10^5 Hz, the 200μm sample is at its lowest dissipation, or at its highest Q factor. Figure 4.8 show the Q-Factor spectroscopy of all Co/PZT/Co and Co/PZT/Ag samples. Since Q is the inverse of the dissipation, we can see that where Q is highest, the dissipation is at its lowest.

Figure 4.9 show the phase angle spectra with both thicknesses of Co/PZT/Co (4.9a), Co/PZT/Ag (4.9b), and Ag/PZT/Ag (5.11c). Here we can appreciate the nature of the sample to behave as either a capacitor at certain frequencies, or as a resistor. Both samples of thickness 200 μm with configuration

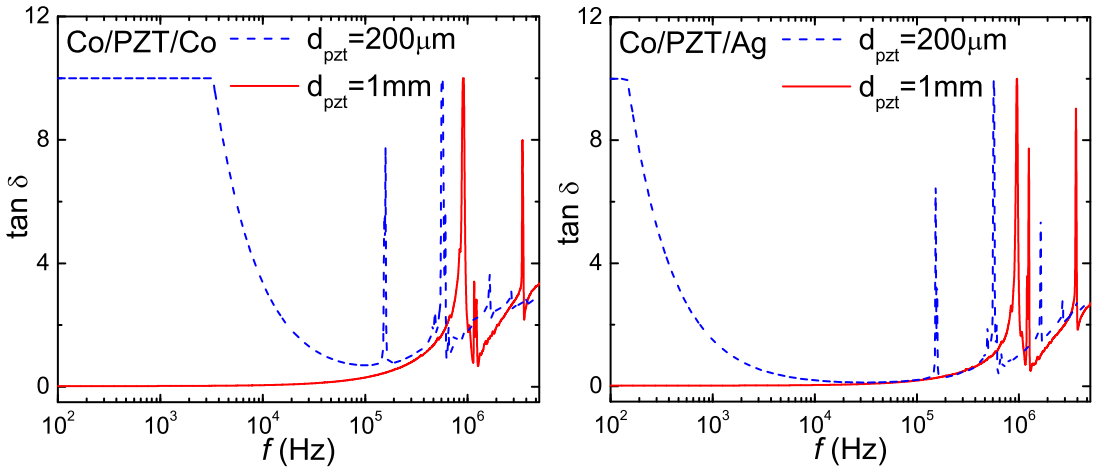

(a) (b)

Figure 4.7: Loss coefficient ($\tan(\delta)$) of (a) 1mm PZT and 200μm with Co/PZT/Co configuration and (b) 1mm PZT and 200μm with Co/PZT/Ag at 0T and room temperature.

Co/PZT/Co and Co/PZT/Ag behave similar, where they start as a resistance, with a phase angle $\simeq 0°$. This equates with the loss portion of the tan δ. Followed with the same behaviour as shown with the loss factor. We can further compare with the simple capacitor Ag/PZT/Ag in Figure 5.11c. Here we see that this truly behaves as a capacitor until the resonance frequencies at >240 kHz. This means that the addition of the ferromagnetic layer is affecting greatly the performance and behaviour of the samples.

4.2.1.3 Impedance Spectroscopy

The impedance spectroscopy of the cobalt based samples were obtained by the measurements of complex impedance, which includes its real (resistance) and imaginary (reactance) parts. The imaginary part holds all the information necessary to study the samples, including resistance values for the equivalent circuitry of the samples. Figure 4.10 show the imaginary part of the impedance for sample Fe/PZT/Fe with PZT thickness of 1.00 mm (4.10a) and 200 μm

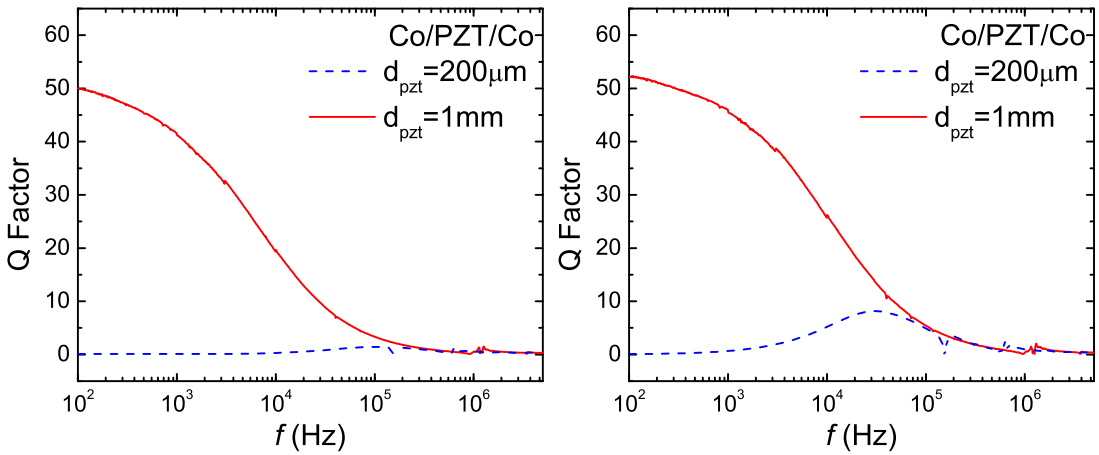

Figure 4.8: Q-Factor of 1mm PZT and 200μm with (a) Co/PZT/Co and (b) Co/PZT/Ag configuration at 0T and room temperature.

(4.10b). The 1.00 mm sample, since is very thick, we can observe that the peak lies outside of the measured area, on the other hand, the 200 μm sample has a broad peak present within the measured spectra. Utilizing Jonscher's dielectric response model mentioned in Section 2.2.2.4 and the equation [3, 4]:

$$Z" = R_g \left[\frac{\omega R_g C_g}{1 + (\omega R_g C_g)^2} \right] + R_{gb} \left[\frac{\omega R_{gb} C_{gb}}{1 + (\omega R_{gb} C_{gb})^2} \right] \tag{4.1}$$

We can extrapolate the peak and gather important information. Figure 4.10 demonstrate the fit of the Jonscher model on top of the measured experimental data. This give the values for the resistance and capacitance for the equivalent circuit which can be represented as two systems of a resistance parallel to a capacitance which are in series, better illustrated in Figure 5.13. Table **??** show all the important information obtained from the Jonscher model fit, including the resistance and capacitance values of the equivalent circuit. Here we observe the resistances for the grain (R_g), and the grain boundary (R_{gb}) are acceptable physical values. The same can be observed for the measured and extrapolated

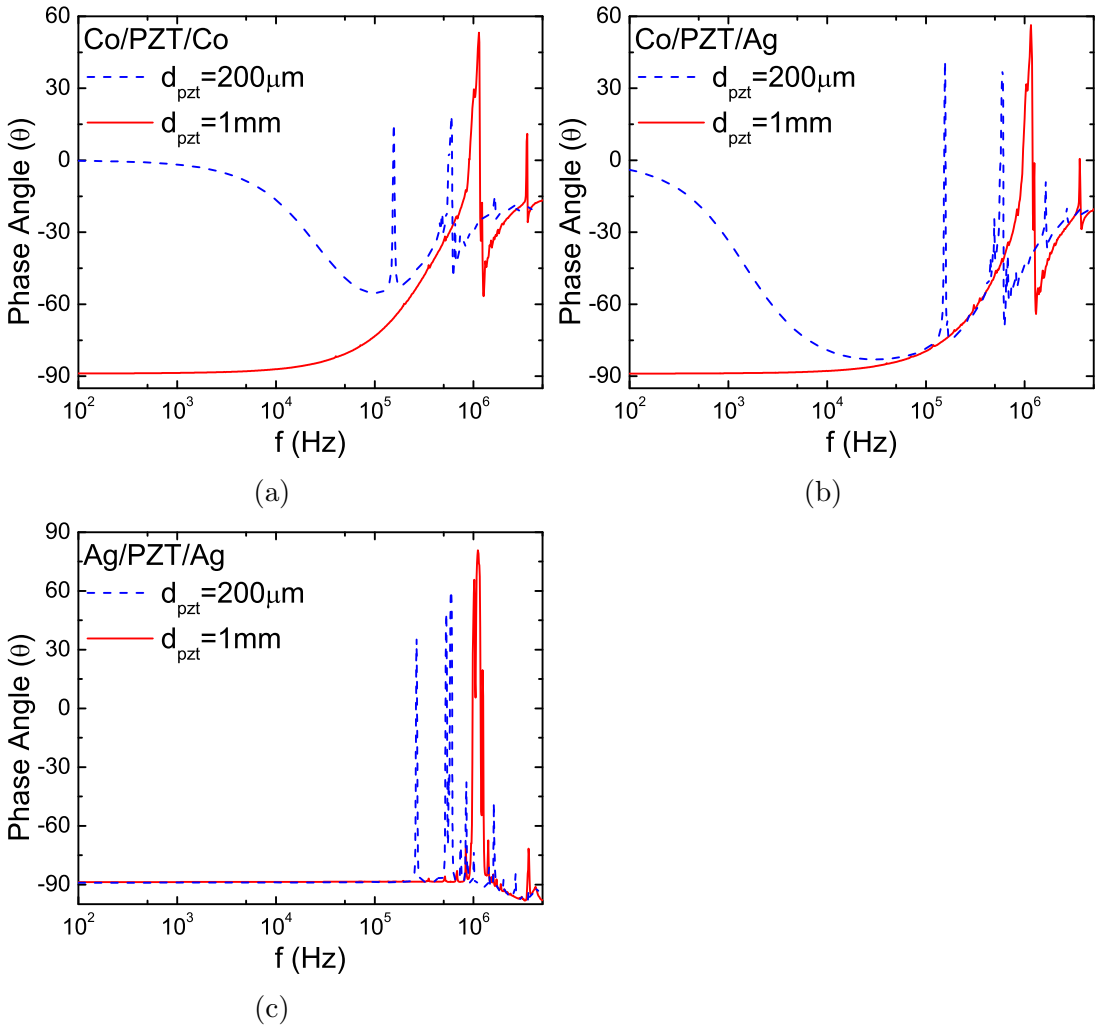

Figure 4.9: Phase Angle (θ) of (a) 1mm PZT and 200μm with Co/PZT/Co configuration, (b) 1mm PZT and 200μm with Co/PZT/Ag, and (c) 1mm PZT and 200μm with Ag/PZT/Ag at 0T and room temperature.

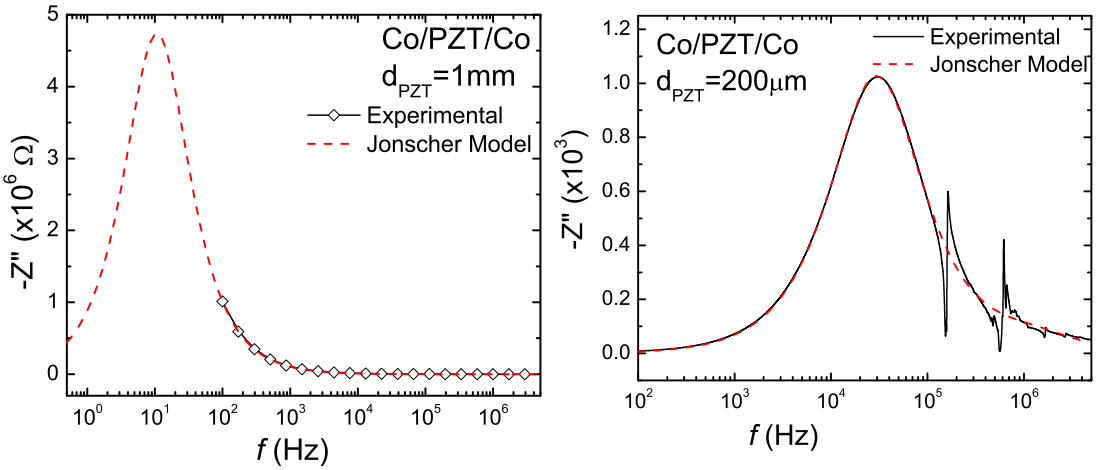

Figure 4.10: Frequency dependent reactance (Z") of Co/PZT/Co (a) d_{PZT}=1.00 mm and (b) d_{PZT}=200 μm.

data of the Co/PZT/Ag samples, where in Figure 4.13 it is shown the plotted and fitted Jonscher model. These values can be corroborated utilizing a fitting software of the nyquist plots using the real and imaginary parts of the samples. Since the 1.00 mm sample's peak lies outside of the measured spectra, the nyquist plot is not possible to build. For the 200 μm sample, since there is a peak in the imaginary part, but is not connected to the real part, the Nyquist plots take a non semi-circle shape. This means that is not a Debye relaxation, and since it has two humps, it can mean that there are two relaxations occurring. This can be observed in Figure 4.12, where the real and imaginary parts are presented (4.12a), and the correspondent Nyquist plot (4.12b).

Using an electrochemical impedance spectroscopy analyser software, we can simulate, fit and obtain real values from the Nyquist plots. The equivalent reference circuit shown in Figure 5.13, we can obtain the same parameters as from the Jonscher equation and corroborate their values.

From Table 4.2, we can observe that the thickness and presence of the ferromagnetic layer affect the placement of the peak in the spectrum. It is evident

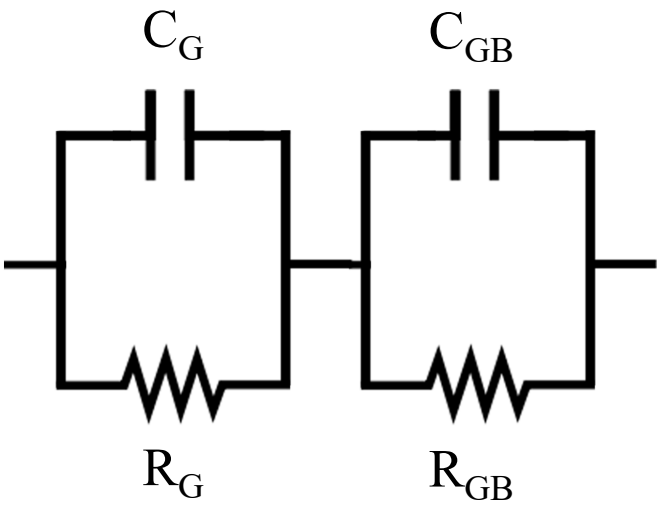

Figure 4.11: Equivalent circuit for samples with grain and grain boundary elements in series.

Table 4.2: Important information from Z" utilizing Equation 5.1 for Co/PZT/Co and Co/PZT/Ag.

Sample	$\mathbf{R}_g$ **(Ω)**	$\mathbf{R}_{gb}$ **(Ω)**	$\mathbf{C}_g$ **(F)**	$\mathbf{C}_{gb}$ **(F)**	$\boldsymbol{f}_{peak}$ **(Hz)**
Co/PZT/Co					
1.00 mm	5732	$9.51\text{x}10^{6}$	$4.39\text{x}10^{-8}$	$1.56\text{x}10^{-9}$	100
200 μm	113.8	$2.05\text{x}10^{3}$	$1.13\text{x}10^{-8}$	$2.61\text{x}10^{-9}$	29794
Co/PZT/Ag					
1.00 mm	5426	$9.52\text{x}10^{6}$	$4.73\text{x}10^{-8}$	$1.63\text{x}10^{-9}$	100
200 μm	7226	$3.84\text{x}10^{4}$	$9.42\text{x}10^{-9}$	$3.01\text{x}10^{-9}$	1483
Ag/PZT/Ag					
1.00 mm	5591	$6.56\text{x}10^{6}$	$4.51\text{x}10^{-8}$	$1.79\text{x}10^{-9}$	13
200 μm	5666	$1.16\text{x}10^{7}$	$4.68\text{x}10^{-8}$	$1.38\text{x}10^{-9}$	9.4

that thicker the sample, greater the resistance, since the charge has to travel a greater distance. The thickness as well brings closer to lower frequencies the thicker the sample, and with greater presence of ferromagnets, the higher the frequency of the peak. We can observe the difference between Fe/PZT/Fe and Fe/PZT/Ag. Ag/PZT/Ag is shown as well as a reference for a normal capacitor

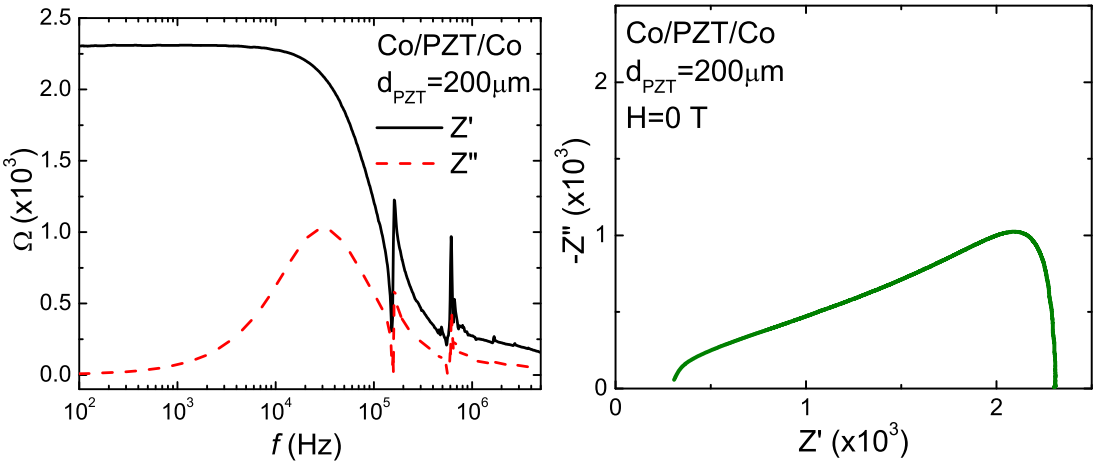

Figure 4.12: (a) Complex impedance of Co/PZT/Co and (b) Nyquist plot of Co/PZT/Co with thickness d$_{PZT}$=200 μm.

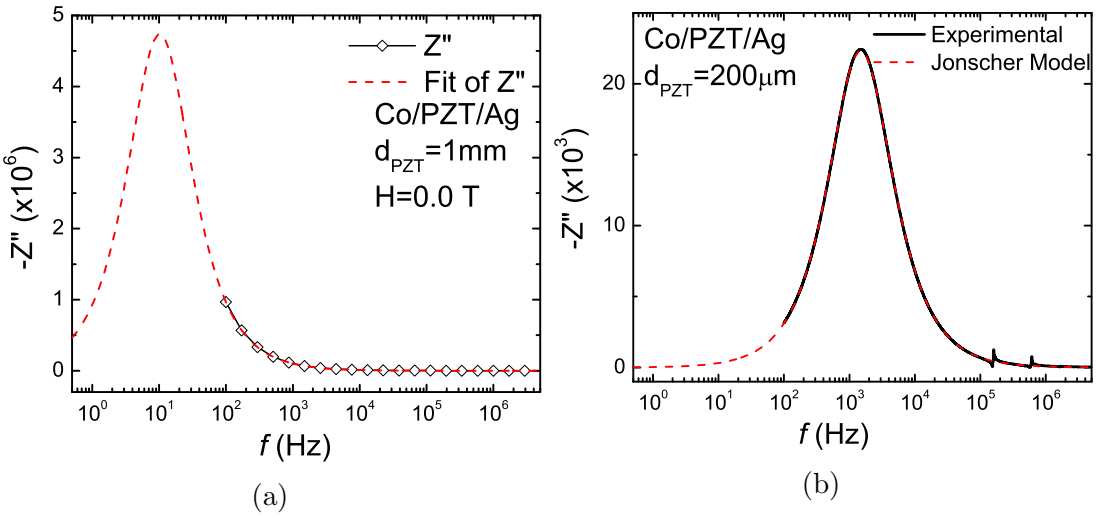

Figure 4.13: Frequency dependent reactance (Z") of Co/PZT/Ag (a) d$_{PZT}$=1.00 mm and (b) d$_{PZT}$=200 μm.

without the spin nature. The imaginary parts of the Ag/PZT/Ag samples are shown in Figure 5.16

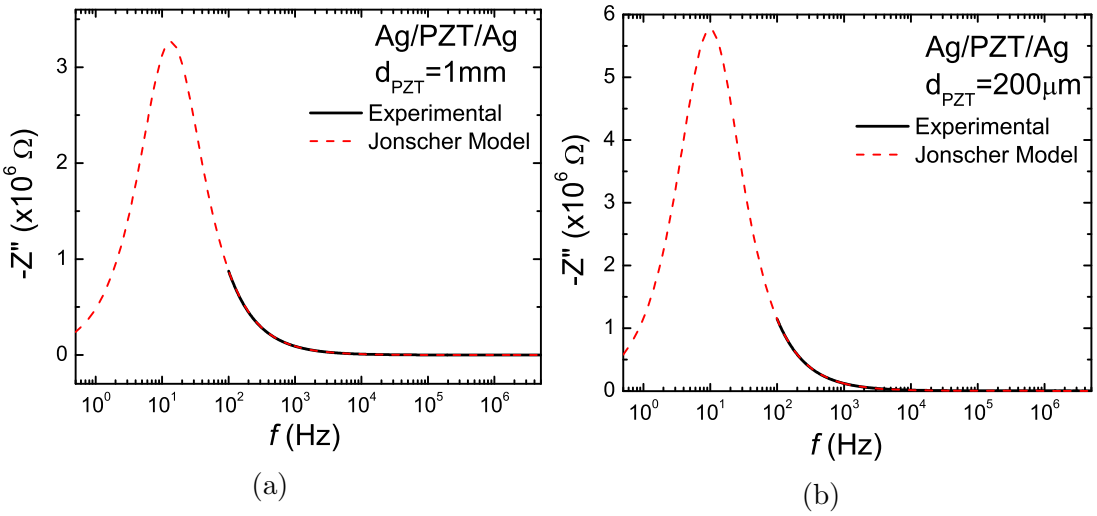

Figure 4.14: Frequency dependent reactance (Z") of Ag/PZT/Ag (a) d_{PZT}=1.00 mm and (b) d_{PZT}=200 μm.

Table 4.3: Information gathered by the imaginary part of the impedance (Z") including resonance frequency (f_r), resonance bandwidth (Δf), Quality factor (Q_m), damping coefficient (β), and damping ratio (ζ) of Fe/PZT/Fe with both thicknesses.

Sample	d_{PZT}	f_r **(Hz)**	Δf	Q_m	β	ζ
Fe/PZT/Fe	**1.4 μm**	63153	258091	0.245	$1.03\text{x}10^{-5}$	2.04
	2.0 μm	58312	219864	0.265	$1.03\text{x}10^{-5}$	1.89

4.2.1.4 Magnetic Properties

In order to understand the magnetodielectric coupling, magnetocapacitance and magnetoimpedance of the heterostructures were measured at room temperature. The samples were subjected to varying magnetic field with a strength up to 2 T. At specific ranges, dielectric measurements were done and compared to each other to determine a difference through the magnetic range. The magnetocapacitance was obtained using Equation 2.33. Similarly, all the magneto related measurements by percentage were calculated using the same equation.

Figure 4.15 show the magnetocapacitance for sample Co/PZT/Co with PZT

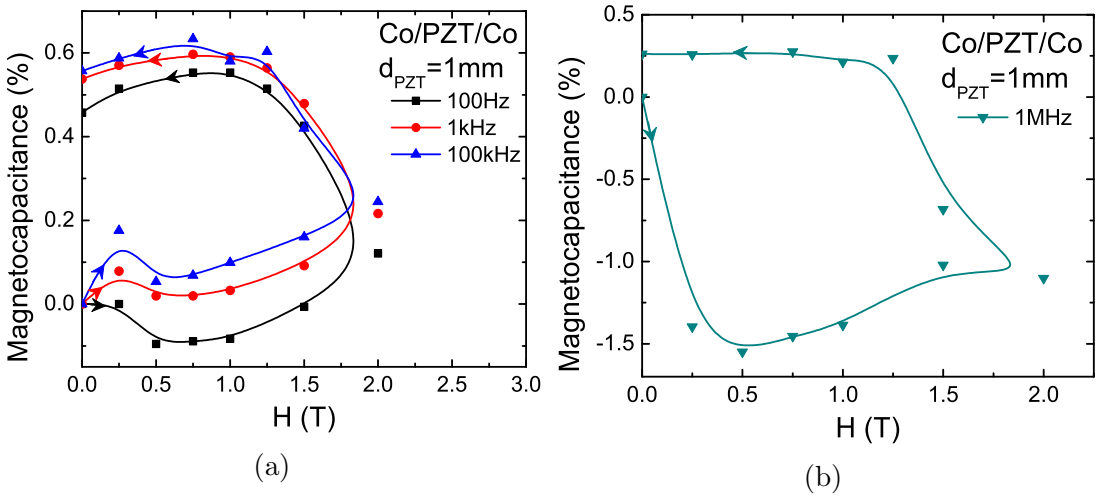

Figure 4.15: Magnetocapacitance of Co/PZT/Co with d_{PZT}=1.00 mm at frequencies (a) 100 Hz and 1 kHz, and (b) 100 kHz and 1 MHz.

thickness of 1.00 mm at specific frequencies in forward and reverse magnetic field (0-2 T) sweeps. As can be seen in Figure 4.15a, the magnetocapacitance is fairly low for these frequencies (100 Hz, 1 kHz, and 100 kHz), only reaching a maximum of 0.45-0.55%. This sample has a loop patterns, which means that it has hysteresis. On the other hand, at 1 MHz in Figure 4.15b, the magnetocapacitance is smaller, negative, and the magnetocapacitance returns back to almost 0%, but on the positive side.This can be expected since at this frequency range the sample becomes more erratic by resonance.

Figure 4.16 show the magnetocapacitance of sample Co/PZT/Ag with PZT thickness of 1.00 mm in the same conditions as previous samples of Co/PZT/Co. In Figure 4.16a, it is observable that the magnetocapacitance reaches a maximum of approx 0.47-0.64%. It is slightly higher compared to the Co/PZT/Co sample. This may be explained with the absence of the second ferromagnetic layer's interference. Both samples, Co/PZT/Co and Co/PZT/Ag, share the same shape and have hysteresis. This means that the sample remains magnetized even after reducing the magnetic field applied. In Figure 4.16b, we observe that for 1 Mhz

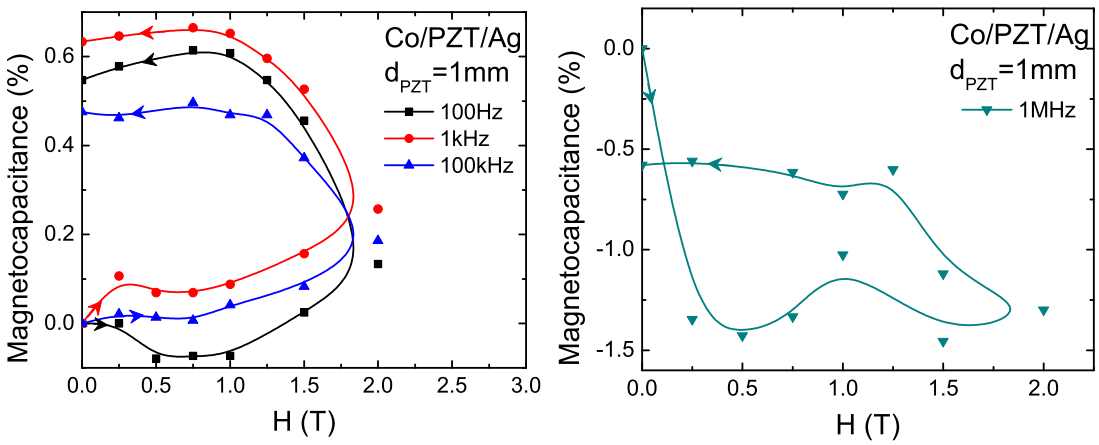

Figure 4.16: Magnetocapacitance of Co/PZT/Ag with d_{PZT}=1.00 mm at frequencies (a) 100 Hz and 1 kHz, and (b) 100 kHz and 1 MHz.

the magnetocapacitance is higher comparable with the lower frequencies, were it reaches up to almost -1.5% and has a remanence of -0.58%. Again, this area is affected by the resonances present.

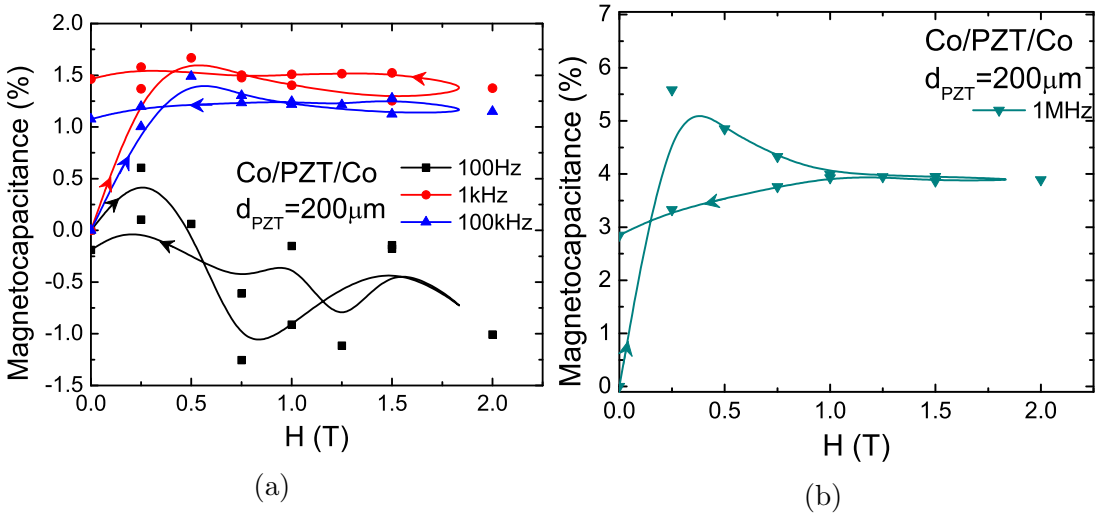

Figure 4.17: Magnetocapacitance of Co/PZT/Co with d_{PZT}=1.00 mm at frequencies (a) 100 Hz, 1 kHz, 100 kHz and (b) 1 MHz.

Figure 4.17 show the magnetocapacitance for sample Co/PZT/Co with PZT thickness of 200 μm at specific frequencies in forward and reverse magnetic field

(0-2 T) sweeps. As can be seen in Figure 4.17a, the magnetocapacitance is fairly low. For 1 kHz and 100 kHz, the magnetocapacitance reaches 1.46% and 1.08% respectively. Interestingly, for 100 Hz, it goes to the negative side, reaching almost -1.5% and returning back to almost 0%. On the other hand, for 1 MHz in Figure 4.17b, a higher result is present. It reaches 5.5%% and a sweep returning to a remanet value of 2.8%. Again, this is close to the relaxation frequency, where the sample has most activity.

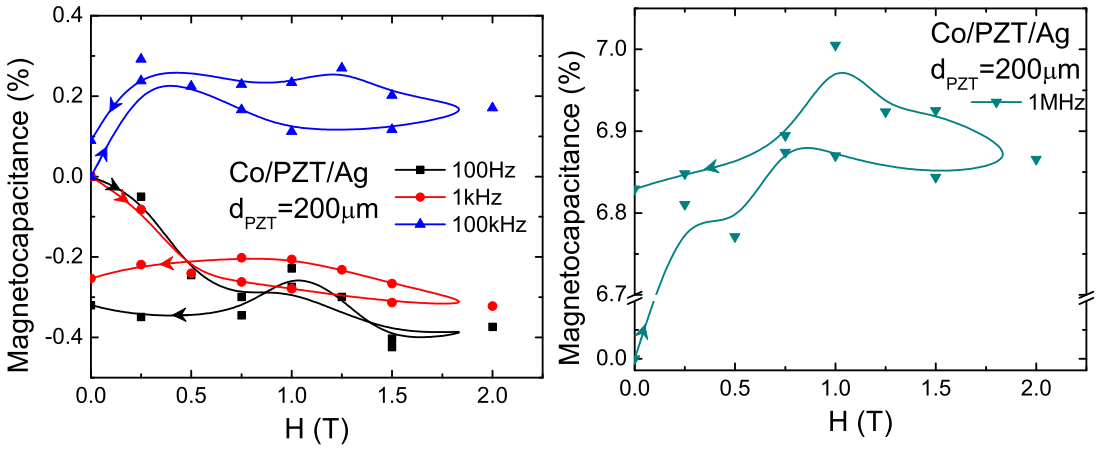

Figure 4.18: Magnetocapacitance of Co/PZT/Ag with d_{PZT}=1.00 mm at frequencies (a) 100 Hz, 1 kHz, 100 kHz and (b) 1 MHz.

Figure 4.18 show the magnetocapacitance for sample Co/PZT/Ag with PZT thickness of 200 μm at specific frequencies in forward and reverse magnetic field (0-2 T) sweeps. As can be seen, the magnetocapacitance is negative for 100 Hz and 1 kHz, reaching between -0.25% for 1 kHz and -0.31% for 100 Hz. For the higher frequencies, we observe that it is of positive change. At 100 kHz it reaches 0.3% and remaining at close to 0.09%. For 1 MHz, as expected, it goes above at a maximum 7% and retains at 6.8%.

Comparing Co/PZT/Co and Co/PZT/Ag, we observe that both samples (Co/PZT/Co and Co/PZT/Ag) of 1.00 mm thick, share striking similarities.

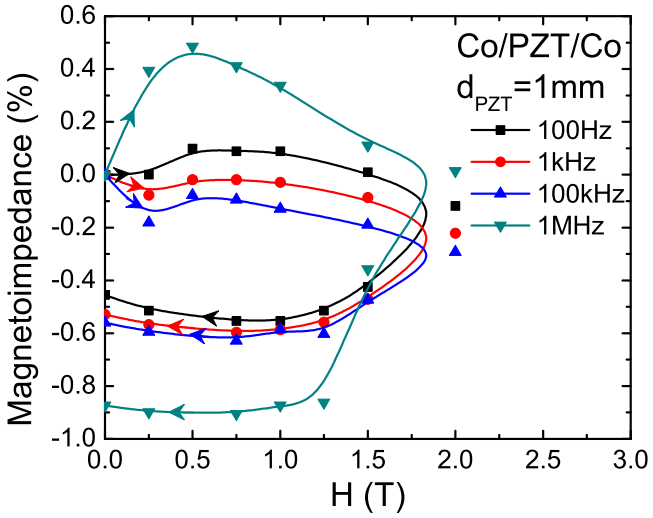

Figure 4.19: Magnetoimpedance of Co/PZT/Co with d_{PZT}=1.00 mm at frequencies 100 Hz, 1 kHz, 100 kHz, and 1 MHz.

On the other hand, the thinner 200 μm sample has higher percent of magnetocapacitance at 1 MHz. These results can be interpreted that the 1.00 mm samples have higher magnetodielectric coupling.

To establish the existence of magnetodielectric coupling, frequency dependent magnetoimpedance measurements were carried out at room temperature. As shown in Figures 4.19 and 4.20, we observe the magnetoimpedance of both samples Co/PZT/Co and Co/PZT/Ag respectively, with PZT thickness of 1.00 mm. Both show low magnetoimpedance and very similar shape, as well, all frequencies chosen fall within the same magnitude. It has a hysteresis shape. This can indicate that there is a present magnetodielectric coupling, but not very large. From Figure 4.20 we observe that for the Co/PZT/Ag sample, having a similar pattern and very low magnetoimpedance percentage reaching in the similar range of negative 0.45-0.8%. These samples show hysteresis. It means it has apparent magnetodielectric coupling.

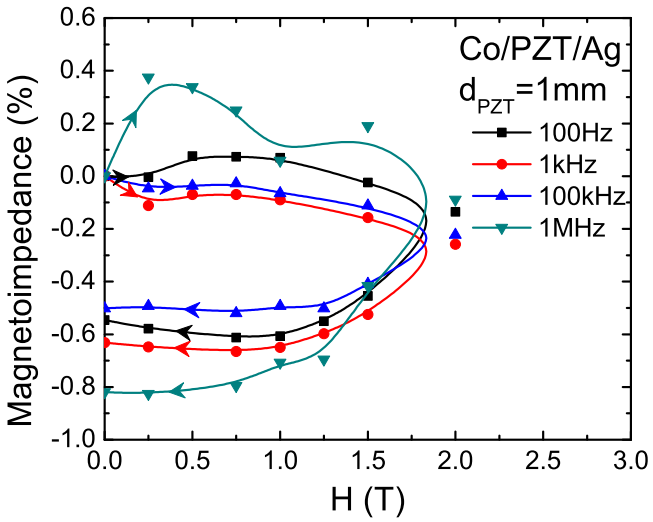

Figure 4.20: Magnetoimpedance of Co/PZT/Ag with d_{PZT}=1.00 mm at frequencies 100 Hz, 1 kHz, 100 kHz, and 1 MHz.

Figure 4.21 show the magnetoimpedance of both samples Co/PZT/Co and Co/PZT/Ag with PZT thickness of 200 μm. On Figure 4.21a show that the frequencies 100 Hz to 100 kHz are on the positive side, with 110 kHz shifting between positive and negative. The 1 MHz plot is on the negative. These samples offer a greater magnetoimpedance that the 1.00 mm samples. The 1 MHz rising up to almost -3% and ending at -1.5%. Both 100 Hz and 1 kHz plots share the shape, reaching almost 8% and ending between 7.8% and 7.6%. The shape is no the expected for a hysteresis, but there is still magnetization.

All the samples show similarities that at higher frequencies there are bigger changes by the applied magnetic field. This information show that there is magnetodielectric coupling.

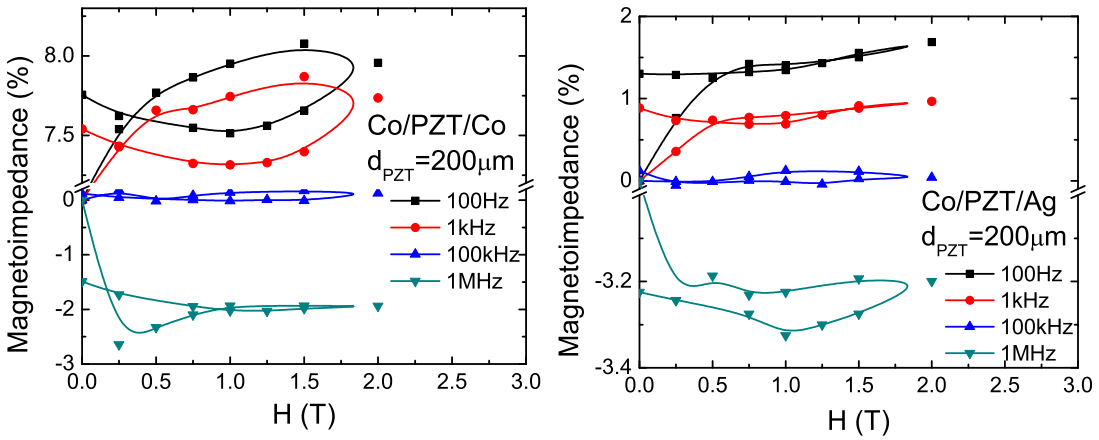

Figure 4.21: Magnetoimpedance of (a) Co/PZT/Co and (b) Co/PZT/Ag with d_{PZT}=200 μm at frequencies 100 Hz, 1 kHz, 100 kHz and, 1 MHz.

4.2.2 Thin Samples

These samples where put through a AFM/Profilometer to determine their thickness. The measured average thickness of two selected samples where of 3.8μm and the thicker one being of 4.8μm. The thickness achieved is "100" times thinner than the commercially obtained samples of 200μm. Following suit as with the samples done before, the SPL deposited Co/PZT/Co samples where subjected to the same measurements and conditions. Dielectric measurements where done in the range of 100Hz to 5GHz with a magnetic field presence from 0 T up to 2 T and back down.

4.2.2.1 Dielectric Permittivity

From Figure 4.22 we can observe the dielectric response of the samples. Both share very similar behaviour and magnitude. The dielectric permittivity starts for both at 9.5. The 3.8 μm sample has a more linear drop per frequency compared to the 4.8 μm, that has a more curved and sharper drop. Both reach 2.5 MHz and have small rise. With further inspection, on Figure 4.23 we observe

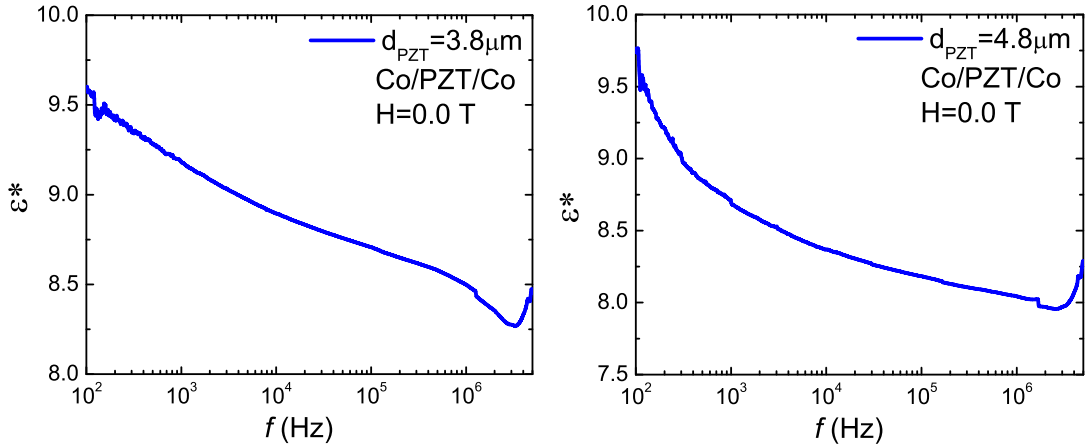

Figure 4.22: Dielectric permittivity of (a) Co/PZT/Co with d$_{PZT}$=3.8μm and (b) Co/PZT/Co with d$_{PZT}$=4.8μm.

the real and imaginary parts of the samples. The whole complex permittivity (ϵ*) has a small slope, only decreasing from almost 10 to 8', but the real and imaginary parts interact from 0 up to the complex unity. This shows the nature of how they add and subtract from each other. The real part has a negative slope, as it is expected, which means that there is a stop in polarization occuring.

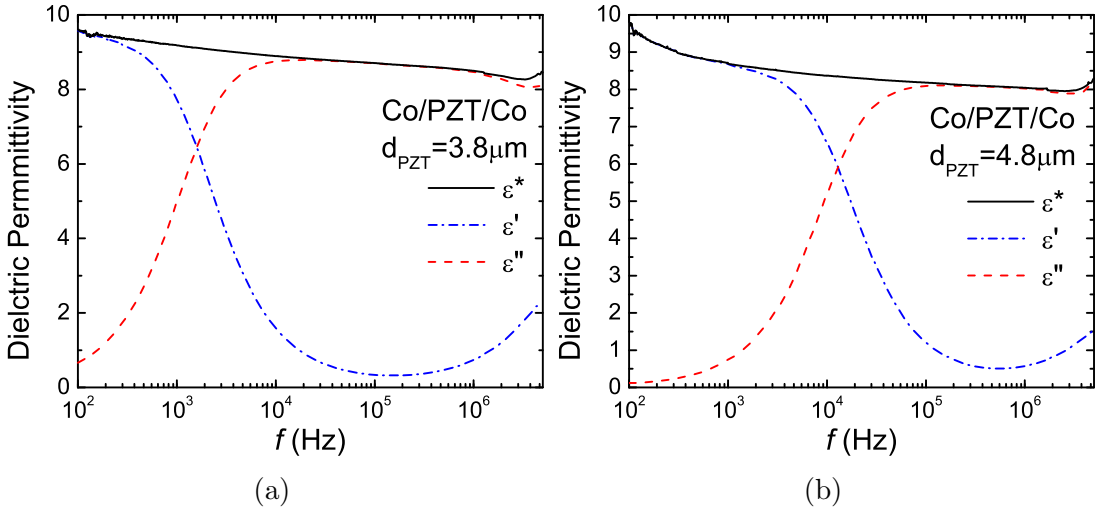

Figure 4.23: Complex permittivity of Co/PZT/Co thin samples illustrating the real and imaginary parts.

The imaginary part, as can be seen, does not present a visible peak, in the meaning of a gaussian shape. In this case we see that ϵ" rises and stays on the top. This can mean that the relaxation time is very wide since it has a sum of relaxations packed together from the diferent components of the sample. Since the frequency range of the peak is <1 MHz it means that is space-charge relaxation.

4.2.2.2 Phase Angle and Dielectric Loss

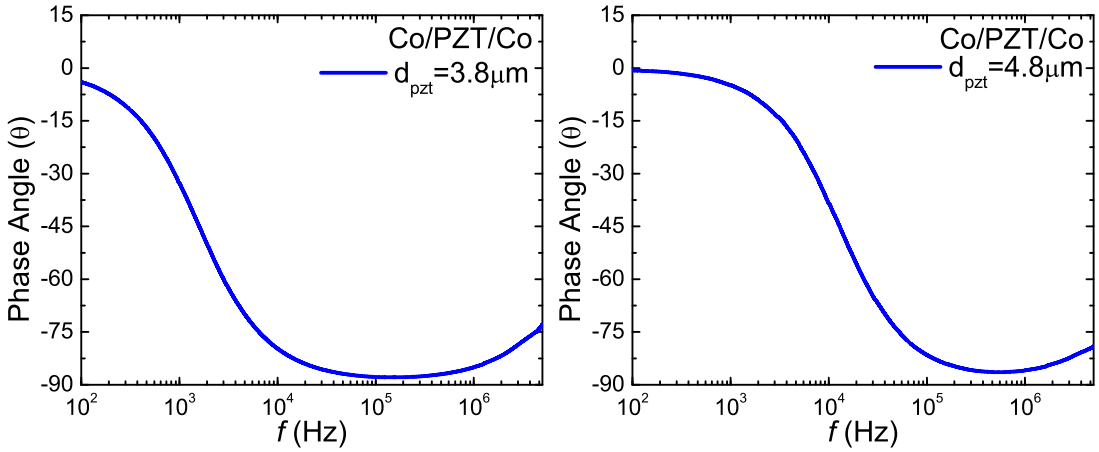

(a) (b)

Figure 4.24: Phase angle of SPL deposited (a) d_{PZT}=1.4μm PZT thickness and (b) d_{PZT}=2μm with Co/PZT/Co configuration at 0T and room temperature in the frequency range of 100Hz to 5MHz.

Both samples at low frequencies start as resistors, given that the bias voltage was of 1V, and that the sample is very thin, it behaves as a resistor, but at further frequencies it starts to shift towards the negative side, reaching almost -90°. For it to be a full capacitor, it must reach -90°. This is shown in Figure 4.24. This means that it has high loss current, and this can be proved and observed further with the loss coefficient graph shown in Figure 4.25a. Here we can observe that for both samples there is high current loss. The sample with thickness 4.8 μm

has higher loss until 1.1 kHz whereas the 3.8 μm stops at 144 Hz. Where the phase angle approaches to the lower negative sides, towards -90°, we observe that the loss coefficient lowers closer to 0. Again, when we have lower, to no dissipation and current loss, we arrive to capacitors area, where there is energy storage. This samples are not that lossy. The Q Factor is the inverse on the loss coefficient, meaning that where there is a peak in Q factor, it has best qualities.

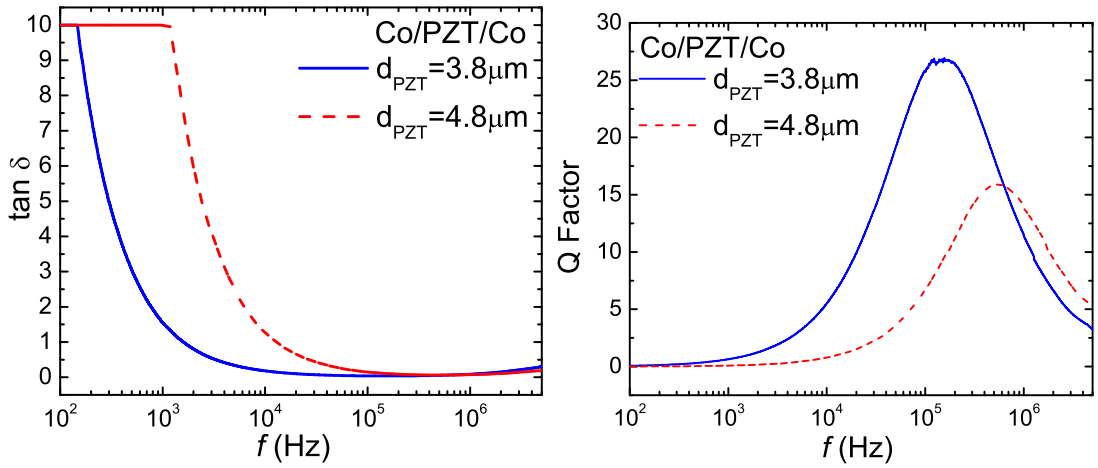

(a) (b)

Figure 4.25: (a) Loss Coefficient of SPL deposited d_{PZT}=1.4μm PZT thickness and d_{PZT}=2μm, and (b) Q factor with Co/PZT/Co configuration at 0T and room temperature in the frequency range of 100Hz to 5MHz.

4.2.2.3 Impedance Spectroscopy

The impedance measurements offers a great spectrum of information of the samples, most data obtained are derived from the impedance of the sample. Here in Figure 4.26 we observe the sample's resistive behaviour by impedance. Since these samples have a very thin thickness we can see that there is a limit of impedance on lower frequencies. This is where we see higher loss current. This is followed by normal exponential decay. The impedance is composed by both real and imaginary parts, these can be observed on Figure 4.26. Figure 4.26a we

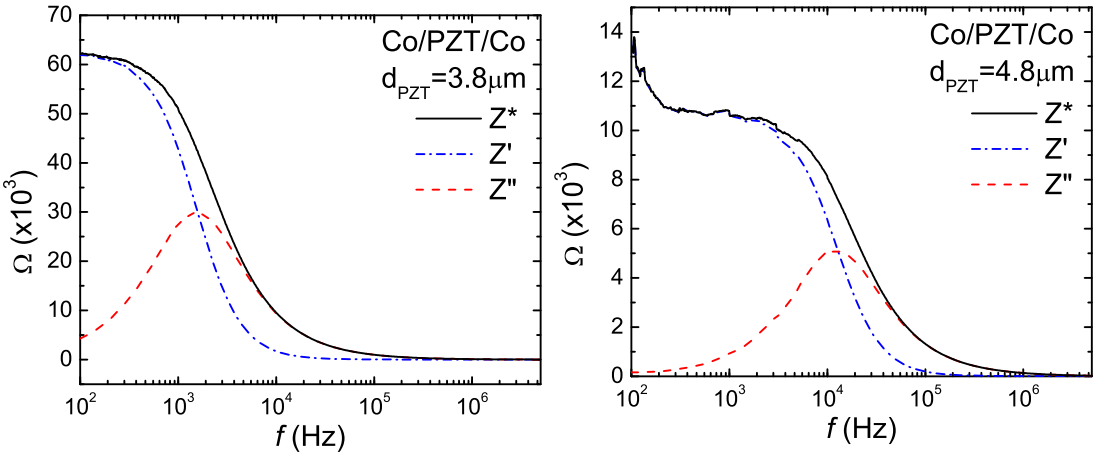

Figure 4.26: Complex impedance of SPL deposited (a) d_{PZT}=3.8μm PZT thickness and (b) d_{PZT}=4.8μm with Co/PZT/Co configuration at 0T and room temperature in the frequency range of 100Hz to 5MHz with the real (Z') and imaginary (Z") parts.

see that for the sample with thickness of 3.8μm, the real and imaginary parts intersect, even thought it is not exatly at the highest point of the peak. This means that the relaxation does not have a strict Debye response. The same can be observed with sample 4.8 μm. For a true Debye response, this occurs exactly in the center. Utilizing the Jonscher model we can obtain all the important information of the equivalent circuitry. This information is present in Table 4.4, where the resistance and capacitance of the grains and grain boundary are shown. These are derived from the Jonscher model using Equation 5.1.

Table 4.4: Important information from impedance spectroscopy utilizing Equation 5.1 and Nyquist plot for Co/PZT/Co thin film samples.

Sample	$\mathbf{R}_g$ **(Ω)**	$\mathbf{R}_{gb}$ **(Ω)**	$\mathbf{C}_g$ **(F)**	$\mathbf{C}_{gb}$ **(F)**	$\boldsymbol{f}_{peak}$ **(Hz)**
3.8 μm	48958	12365	$1.88\text{x}10^{-9}$	$1.39\text{x}10^{-8}$	1583
4.8 μm	10157	306	$1.23\text{x}10^{-9}$	$2.59\text{x}10^{-7}$	11241

Figure 4.27 show the Nyquist plots for the samples Co/PZT/Co with thick-

ness d_{PZT}=3.8 μm (4.27a), and d_{PZT}=4.8 μm (4.27b). These samples, since the imaginary peak is present within the measured spectra, we can obtain a Nyquist plot, which in turn enables us to simulate an equivalent circuit and fit to the experimental data. After simulating the circuit described in Figure 5.13, and within Figure 4.27, we obtain information and values for the circuit of the grain and grain boundary. This is corroborated with the Jonscher model with Equation 5.1 and the information in Table 4.4, and obtain equal results. For both samples, we can observe that the semi-circle start close to 0 Ω, this means that there is a negligible starting resistance which can be attributed to the contacts between the sample and the measuring device. The solid line in Figure 4.27 shows simulated fit of equivalent circuit to the data using a an electrochemical impedance spectroscopy (EIS) spectrum analyser software [5].

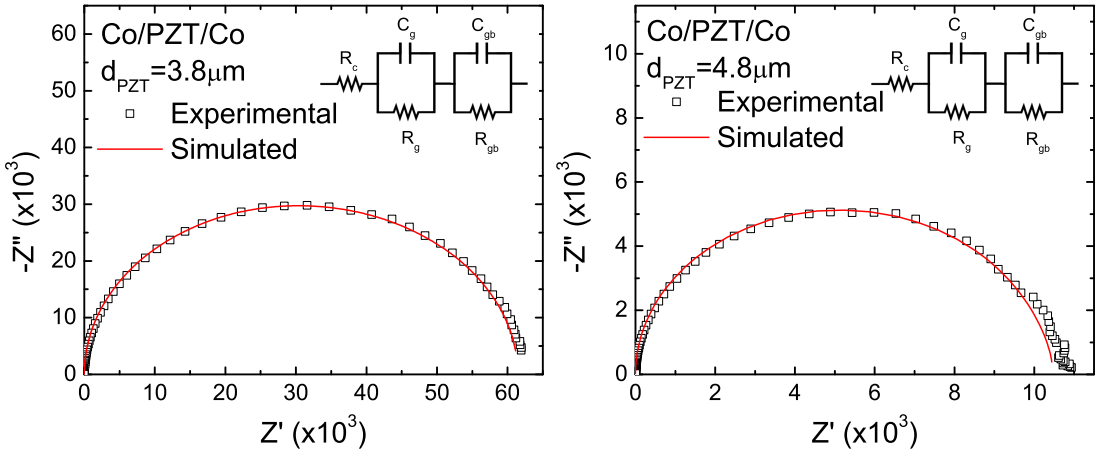

Figure 4.27: Real and imaginary parts from the impedance graphed in a Nyquist plot of SPL deposited (a) d_{PZT}=3.8μm PZT thickness and (b) d_{PZT}=4.8μm with Co/PZT/Co configuration at 0T and room temperature in the frequency range of 100Hz to 5MHz. The Jonscher model is fitted and the equivalent circuit presented.

4.2.2.4 Magnetic Properties

In order to understand the magnetodielectric coupling, magnetocapacitance and magnetoimpedance of the thin film heterostructures were measured at room temperature. The samples were subjected to varying magnetic field with a strength up to 2 T. At specific ranges, dielectric measurements were done and compared to each other to determine a difference through the magnetic range. The magnetocapacitance was obtained using Equation 2.33. Similarly, all the magneto related measurements by percentage were calculated using the same equation.

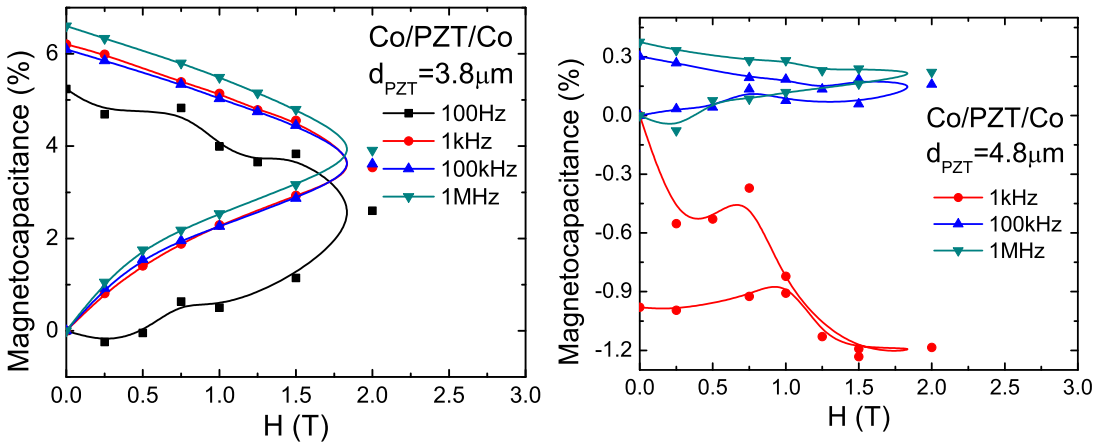

Figure 4.28: Magnetocapacitance of Co/PZT/Co with (a) d_{PZT}=3.8 μm and (b) d_{PZT}=4.8 μm at frequencies 100 Hz and 1 kHz, 100 kHz, and 1 MHz.

Figure 4.28 show the magnetocapacitance of both samples of Co/PZT/Co with thickness 3.8 μm (4.28a) and 4.8 μm (4.28b). Sample 3.8 μm we observe that there is good hysteresis, where the magnetocapacitance reaches a maximum of ≈6%. These are fair magnetocapacitance values. On the other hand, sample 4.8 μm has for the frequencies of 1 kHz and 100 kHz a hysteresis nature, but have low magnetocapacitance for 1 MHz it falls to the negative side and a bit higher magnetocapacitance. This shows that the 3.8 μm sample has better

magnetodielectric coupling.

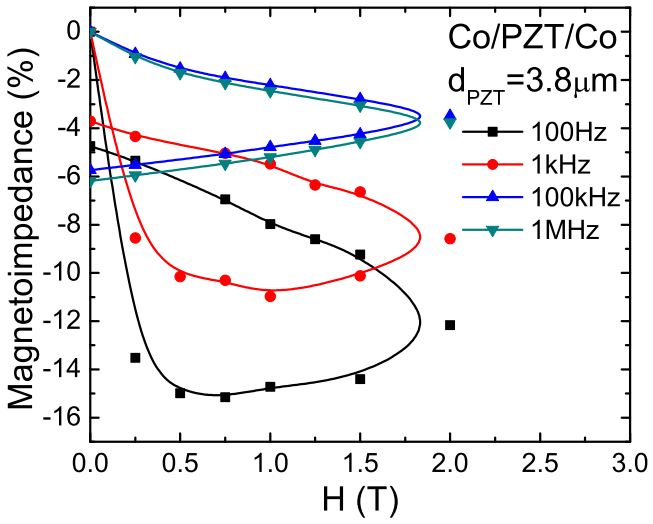

Figure 4.29: Magnetoimpedance of Co/PZT/Co with d_{PZT}=3.8 μm at frequencies 100 Hz and 1 kHz, 100 kHz, and 1 MHz.

To establish the existence of magnetodielectric coupling, frequency dependent magnetoimpedance measurements were carried out at room temperature. As shown in Figure 4.29, we observe the magnetoimpedance of the thin film Co/PZT/Co sample. Similar to the behaviour with the magnetocapacitance, the magnetoimpedance for all frequencies is fairly linear in their increments. For the lower frequencies we see a rise to -4% to -5%. In the higher frequency of 100 kHz and 1 MHz, we see a broader loop with a higher remanent magnetoimpedance that reaches -6%. It is evident that there is a magnetodielectric coupling present. The higher frequencies show better this evidence, thanks to their linear increments and higher magnetic remanent values and hysteresis shape. The Figure 4.30 show the magnetoimpedance of the 4.8 μm thick sample. The frequencies of 100 Hz and 1 kHz are presented in Figure 4.30a since they have bigger magnitude, it reaches to -38% and -50%. This is very high. For the higher frequencies, in Figure 4.30b, the maximum is -1.5% at 100 kHz and -0.43%

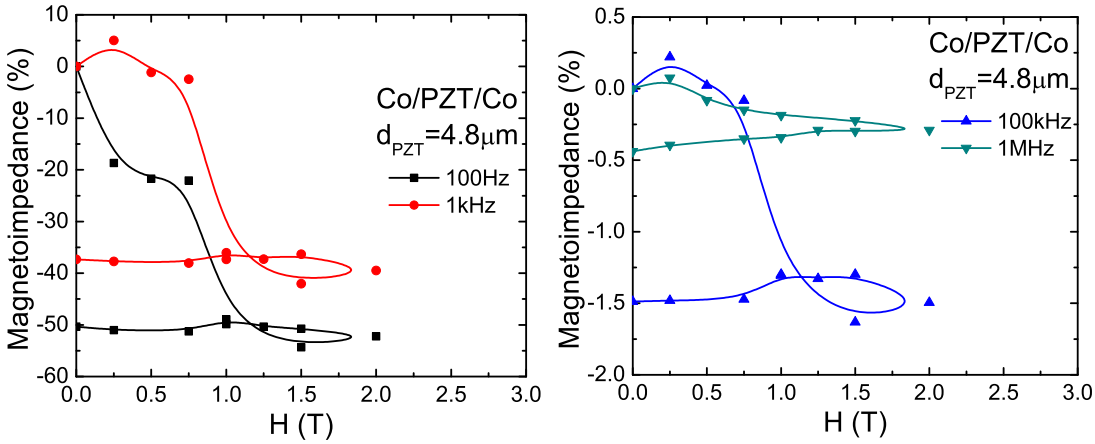

Figure 4.30: Magnetoimpedance of Co/PZT/Co with d_{PZT}=4.8 μm at frequencies (a) 100 Hz and 1 kHz, and (b) 100 kHz and 1 MHz.

at 1 MHz. Still, they show fair hysteresis shape with a remanent magnetization.

4.3 Summary

There are vast differences in magnitude when we compare the bulk samples (1.00 mm and 200 μm) with the thin film samples (3.8 μm and 4.8 μm). It is evident that the thickness plays a huge factor, specially with the resistance and capacitance of the sample. The best result for magnetoelectric coupling can be observed for the thin film samples. this makes then good for device applications, specially the fact that they are made by spray pyrolysis, a very cost effective alternative for thin film growth. It is very interesting to find that the thin film sample (4.8 μm) of Co/PZT/Co has very big magnetoimpedance, which is comparable to reported results [7, 8].

References

[1] Yarmarkin, V. K., Teslenko, S. P., Dielectric relaxation in thin-film metalPZT-ferroelectricmetal structures, Phys. Solid State 40, 17381741 (1998)

[2] Wu, Dawei et al. Dielectric and Piezoelectric Properties of PZT Composite Thick Films with Variable Solution to Powder Ratios. Journal of the American Ceramic Society. American Ceramic Society vol. 92,6 (2009)

[3] Swagatika Dash, R. Padhee, Piyush R. Das & R.N.P. Choudhary, Dielectric and impedance spectroscopy of (Bi0.5Li0.5)(Fe0.5Nb0.5)O3 multiferroics, Phase Transitions, 87:3, 223-235 (2014)

[4] Jonscher AK. The universal dielectric response. Nature. 1977;267:673679.

[5] Bondarenko A. S., Ragoisha G. A. In Progress in Chemometrics Research, Pomerantsev A. L., Ed.; Nova Science Publishers: New York, pp. 89102 (2005)

[6] Y. Zhou, D. Maurya, Y. Yan, G. Srinivasan, E. Quandt, S. Priya, Self-Biased Magnetoelectric Composites: An Overview and Future Perspectives. Energy Harvesting and Systems. 3. 10.1515 (2015)

[7] Jia Y, Zhou W, Ma K, Liu Y. Enhanced Magnetoelectric Effect in Permendur/Pb(Zr0.52Ti0.48)O3 Laminated Magnetostrictive/Piezoelectric Composite. Applied Sciences. 5(3):587-594. (2015)

Chapter 5

Ni/PZT/Ni Multiferroic Heterostructures

This chapter will discuss all the capacitor samples that has nickel as the ferromagnetic layer. The measurements discussed will include the dielectric properties, impedance spectroscopy, and magnetic properties. These samples have the shape of Ni/PZT/Ni, Ni/PZT/Ag, and Ag/PZT/Ag as reference. The chapter is divided in two parts, where the first is the bulk samples that include thicknesses of d_{PZT}=1.00 mm and d_{PZT}=200 μm; and the second part of the chapter being the thin samples which include thicknesses of d_{PZT}=2 μm and d_{PZT}=7 μm. Dielectric measurements show that all samples share a special ferroelectric behaviour. The bulk samples are commercially available PZT substrates of which cobalt was sputtered on top and bottom to make a simple spin capacitor shape. Impedance spectroscopy show that the 1.00 mm thick PZT samples do not exhibit a peak in the imaginary part of the impedance, since these are too thick and the resonance frequency is overly damped and into the lower frequencies, which are out of the measured range. On the other hand, only the 200 μm sample with Ni/PZT/Ag configuration exhibit a peak on the imaginary part of the impedance. The imaginary peaks are then extrapolated by the fitting of the circuit equation 2.32 of the Jonscher model. The phase angle of the d_{PZT}=1.00 mm samples show that it acts as a capacitor at lower frequencies until it reaches a resonant frequency, whereas the d_{PZT}=200 μm sample of shape Ni/PZT/Ag show that it starts as almost a resistor, since it is closer to 0°and has dissipation visible in the loss coef-

ficient measurements, meaning that there is leakage current. This is evident since the sample is 5 times thinner. Furthermore, the thin samples where both SPL deposited PZT samples, show the same behaviour where the phase starts close to 0°at lower frequencies, and falls to almost -90°and then rises up to -30°and -35°. The dielectric behaviour is more apparent in these samples, showing ferroelectric shape. Magnetoelectric coupling is present, as well as hysteresis polarization and will be further discussed.

5.1 Experimental Details

PZT substrates of d_{PZT}=1.00 mm with area of 1.00 cm x 1.00 cm and d_{PZT}=200 μm with an area of 3.00 mm x 1.00 mm were obtained and deposited ferromagnetic cobalt contacts on top and bottom by sputtering, giving them simple capacitor shape with ferromagnetic/ferroelectric/ferromagnetic configuration as shown in Figure 3.1a on the previous chapter. These are the bulk samples. Furthermore, thinner samples were made using Spray Pyrolysis to deposit PZT onto a nickel laminate, and after the SPL deposited PZT, a top nickel contact was deposited to achieve the same capacitor structure as the bulk samples so the measuring devices and methods are equal.

The thin samples where put through a AFM/Profilometer to determine the PZT thickness. The measured average thickness of two selected samples where of 2 μm and the other of 7 μm. The thickness achieved is close to 100 times thinner than the commercially obtained samples of 200 μm. Following suit as with the samples done before, the SPL deposited Ni/PZT/Ni samples where subjected to the same measurements and conditions. Dielectric measurements where done for both bulk and thin samples in the range of 100Hz to 5GHz with a magnetic field

presence from 0 T up to 2 T and back down.

5.2 Results and Discussion

5.2.1 Bulk Samples

Various frequency dependent dielectric measurements where carried out for the samples containing the ferromagnetic material of nickel. Six samples where made that consist of three different capacitor configurations (Ni/PZT/Ni, Ni/PZT/Ag, and Ag/PZT/Ag as reference), with two different PZT substrate thicknesses (d_{PZT}=1.00 mm and d_{PZT}=200 μm). The dielectric measurements done where: capacitance (which in turn can be translated to dielectric permittivity), phase angle, impedance, loss coefficient, loaded Quality Factor, magnetocapacitance, and magnetoimpedance (which is dependent on magnetic fields). The range of frequencies used where from 100 Hz up to 5 MHz. The magnetocapacitance measurements where done with an external applied magnetic field with maximum strength of 2 T. With the complex impedance information, divided by its real and imaginary components, the reference circuit was calculated for those samples using a Nyquist plot that show a clear peak in the imaginary part and corroborating this with a fitted model equation. Further hysteresis magnetoelectric polarization measurements were carried out for the bulk samples by G. Sreenivasulu and G. Srinivasan at Oakland University, Rochester, Michigan, USA.

5.2.1.1 Dielectric Permittivity

The samples where subjected to capacitance measurements for the frequency range of 100 Hz up to 5 MHz. As well, the samples where introduced to a mag-

netic field for a range from 0 T up to 2 T and back down to 0 T, this gives us the relation in the ferroelectric and ferromagnetic coupling and the reminiscence of it. To obtain the dielectric permittivity of each sample, their capacitance measurement was multiplied by a factor containing the information of the ferromagnetic contact area, thickness of the PZT layer and dielectric constant of vacuum. The Equation 2.12 is in Section 2.2.2.1.

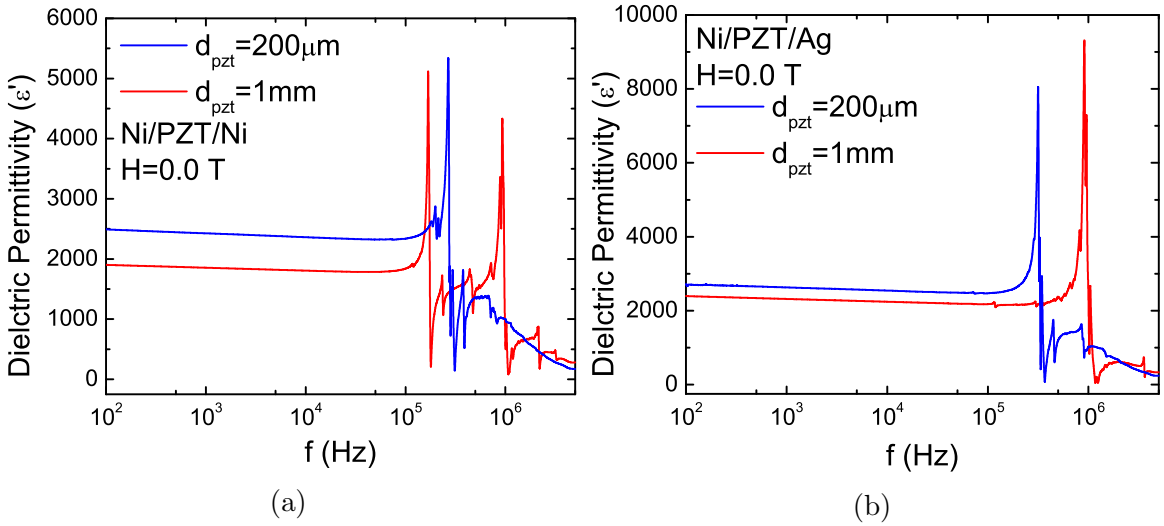

Figure 5.1: Dielectric permittivity of (a) 1mm PZT and 200μm with Ni/PZT/Ni configuration and (b) 1mm PZT and 200μm with Ni/PZT/Ag at 0T and room temperature.

Figure 5.1 show the frequency variation of dielectric permittivity for (a) Ni/PZT/Ni and (b) Ni/PZT/Ag with both 1mm and 200 μm. We can observe that for all the samples, the behaviour is very linear and almost constant at the frequency range of 100 Hz to $\approx 10^5$ Hz, where resonances are present. This resonance peaks are huge, having a gain of $\approx$2500 for the Ni/PZT/Ni samples and $\approx$5000 for the Ni/PZT/Ag samples. These huge resonance peaks are accompanied by smaller reflections. It is observable that comparing the samples Ni/PZT/Ni to Ni/PZT/Ag for the thickness of 1.00 mm, that there are two mayor resonance peaks for Ni/PZT/Ni and one mayor peak for Ni/PZT/Ag. On

the other hand, for the 200 μm we see one mayor resonance peak for both thicknesses, but at closer inspection, the Ni/PZT/Ni sample exhibit extra smaller peaks near to the mayor one, whereas Ni/PZT/Ag does not. This can mean the interaction of the coupling between the ferromagnetic interfaces. At thinner samples, these peaks are closer to each other. Further information about the resonance peaks can be found in Table 5.1.

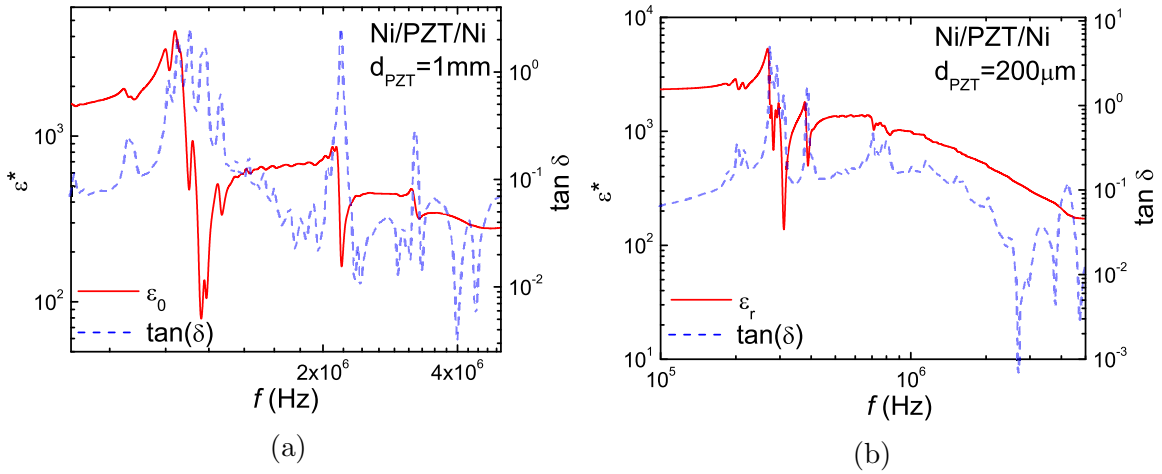

Figure 5.2: Comparison of the dielectric permittivity with loss coefficient of Ni/PZT/Ni for (a) d_{PZT}= 1.00 mm and (b) d_{PZT}=200μm at 0T and room temperature.

Figures 5.2, 5.3, and 5.4 show the relationship of the dielectric permittivity with the loss coefficient. Since the loss coefficient is directly related to the capacitance, we can note that where there is a spike in the dielectric permittivity, there is a inverse spike in the loss coefficient, and the opposite is equal, where there are peaks in the loss coefficient, there are inverse peaks in the dielectric permittivity. This tells that where the capacitance drops, there is a loss, or a leakage of current. In an ideal resonator, the power dissipation is zero, whereas in a 'lossy' resonator, due to piezoelectric coupling, the power dissipation becomes large at resonance.

Dividing the dielectric permittivity by its complex components, being the

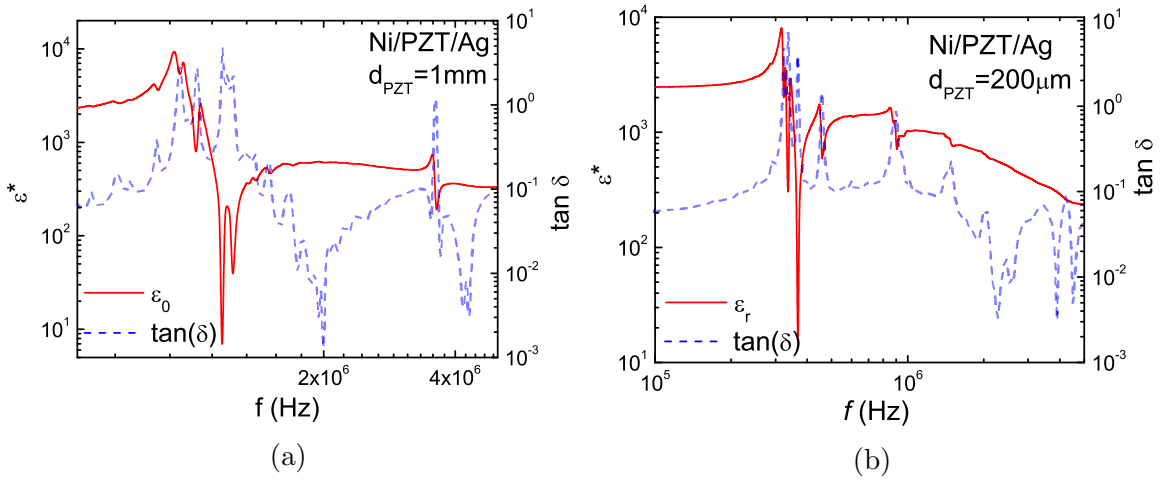

Figure 5.3: Comparison of the dielectric permittivity with loss coefficient of Ni/PZT/Ag for (a) d$_{PZT}$= 1.00 mm and (b) d$_{PZT}$=200μm at 0T and room temperature.

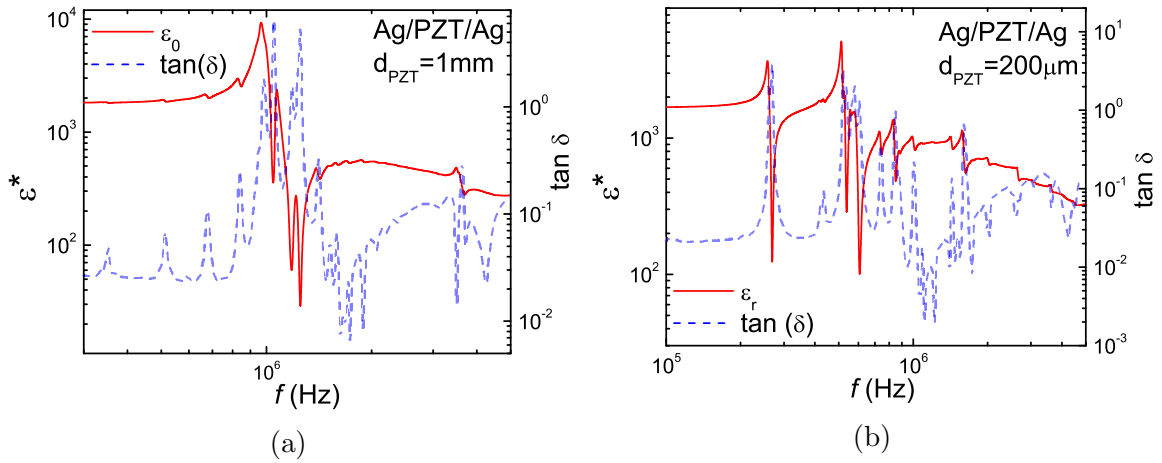

Figure 5.4: Comparison of the dielectric permittivity with loss coefficient of Ag/PZT/Ag for (a) d$_{PZT}$= 1.00 mm and (b) d$_{PZT}$=200μm at 0T and room temperature.

real and imaginary parts, we can observe if there are relaxations and/or resonances present in the frequency range. All samples are shown in Figures 5.5, 5.6, and 5.7. All the samples have similar behaviour, where the real part closely resembles the whole complex dielectric permittivity, were we see that at there are resonance peaks at high frequencies for all samples. The resonance peaks are identifiable by their shape. These inverse peaks appear in pairs, we may

Table 5.1: Frequency information of mayor resonance peaks in the imaginary part of Ni/PZT/Ni and Ni/PZT/Ag.

Ni/PZT/Ni	$\mathbf{d_{PZT}}$**=1.00 mm**	$\mathbf{d_{PZT}}$**=200 μm**
$\boldsymbol{f}_{peak}$	170 kHz	271 kHz
τ	5.87x10^{-6} s	3.68x10^{-6} s
Q Factor	32	31
Max Dielectric	3835	4018
Ni/PZT/Ag	$\mathbf{d_{PZT}}$**=1.00 mm**	$\mathbf{d_{PZT}}$**=200 μm**
$\boldsymbol{f}_{peak}$	922 kHz	319 kHz
τ	1.08x10^{-6} s	3.13x10^{-6} s
Q Factor	15	22
Max Dielectric	6357	6288

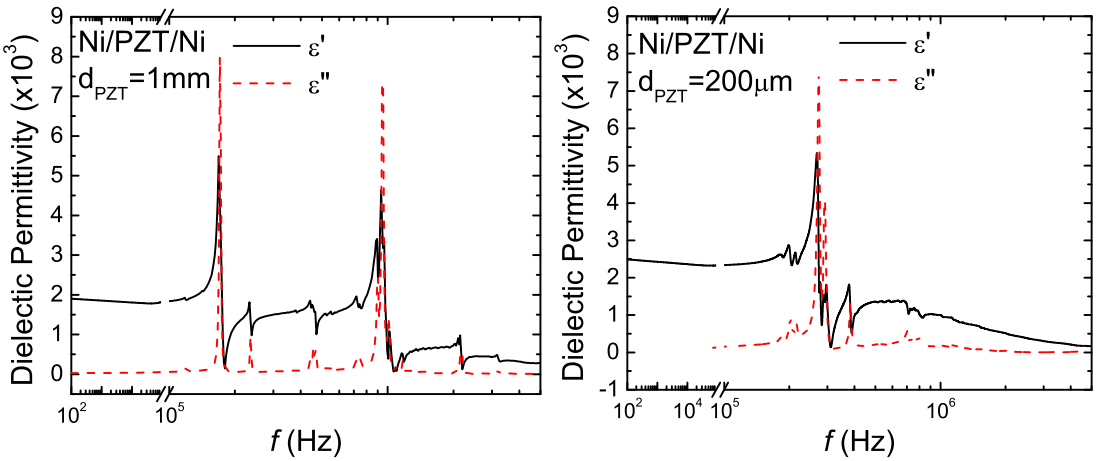

(a) (b)

Figure 5.5: Complex dielectric permittivity comparison of (a) 1mm PZT and (b) 200μm of Ni/PZT/Ni with real and imaginary parts of the dielectric permittivity.

determine that these are present because of the interface coupling between the ferroelectric and ferromagnetic layers, This can further be proved with the thin film samples and their relaxation peaks. Utilizing the peaks in the imaginary part we can obtain valuable information like the relaxation time τ, and the Q factor, which is dependent on the resonance peak frequency and the bandwidth.

The best way to observe the difference the ferromagnetic layer add to the

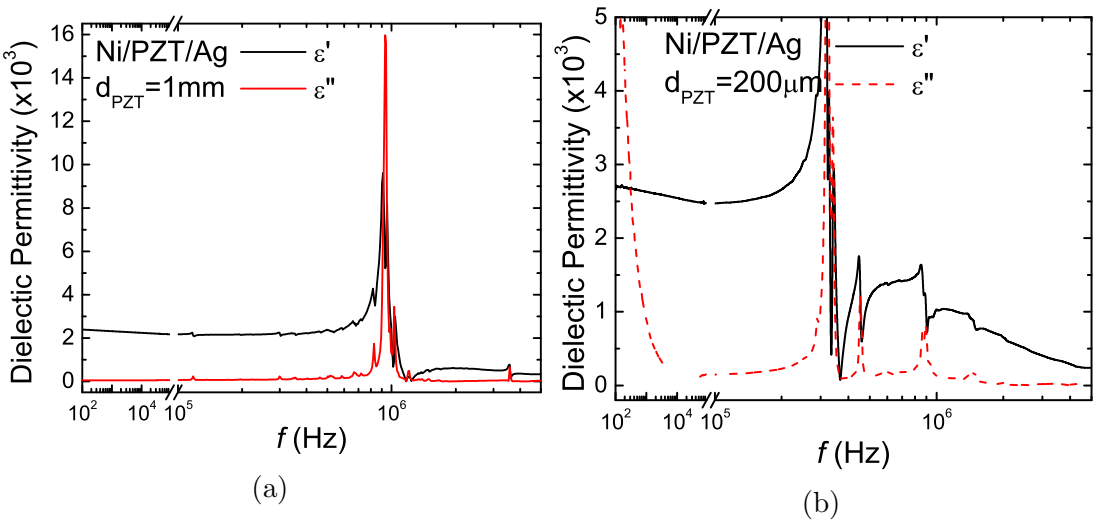

Figure 5.6: Complex dielectric permittivity comparison of (a) 1mm PZT and (b) 200μm of Ni/PZT/Ag with real and imaginary parts of the dielectric permittivity.

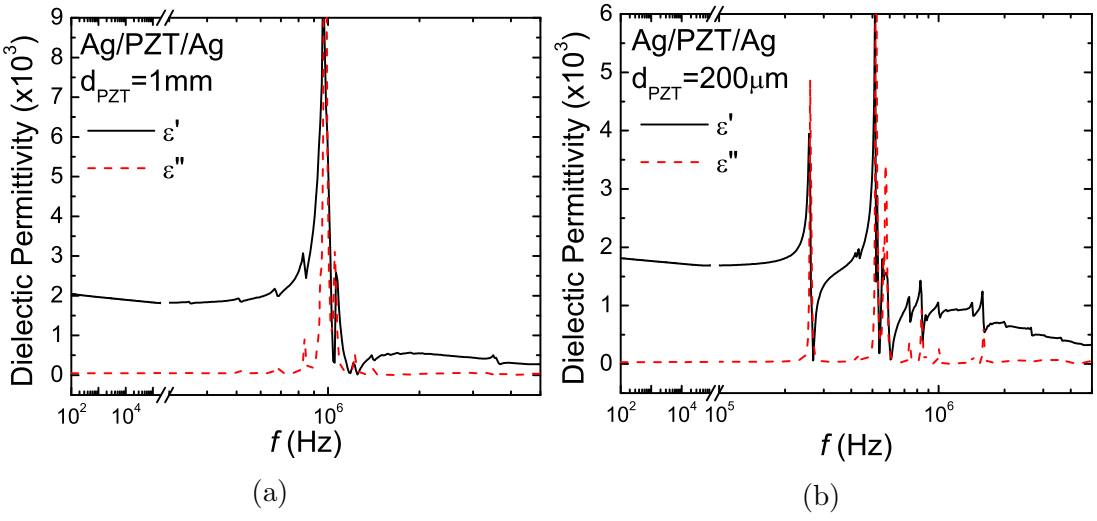

Figure 5.7: Complex dielectric permittivity comparison of (a) 1mm PZT and (b) 200μm of Ag/PZT/Ag with real and imaginary parts of the dielectric permittivity.

sample is shown in Figure 5.8. This figure show how the dielectric response is affected once a ferromagnetic layer is present, and the further addition of both ferromagnetic layers. It is highly acceptable that there is an interaction in the FE/FM interface, enough to affect the dielectric response and shift the peaks in the spectra. We can see that for the thick sample of 1.00 mm, the big resonance peak at ≈1 MHz shifts only slightly, meaning that the interaction may be easily dampened by the thickness, whereas the 200 μm sample show grater shift.

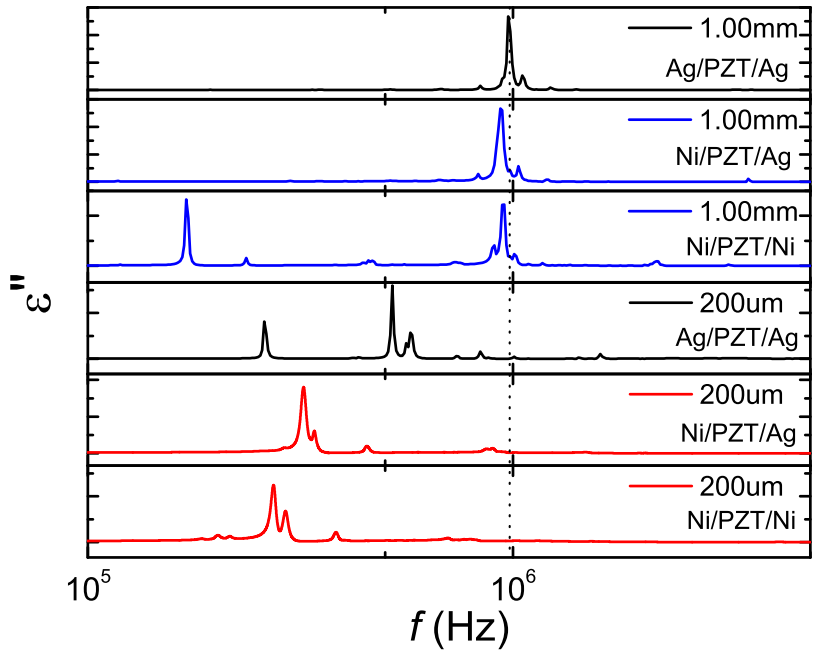

Figure 5.8: Imaginary part of the complex dielectric permittivity of all bulk samples.

5.2.1.2 Phase Angle and Dielectric Loss

The angle of the phase demonstrate the relationship between the real and imaginary parts of the material and its electrical properties. This relation between the real and imaginary brings the relationship of the loss and storage properties. The phase is the ratio between real and imaginary, where the di-

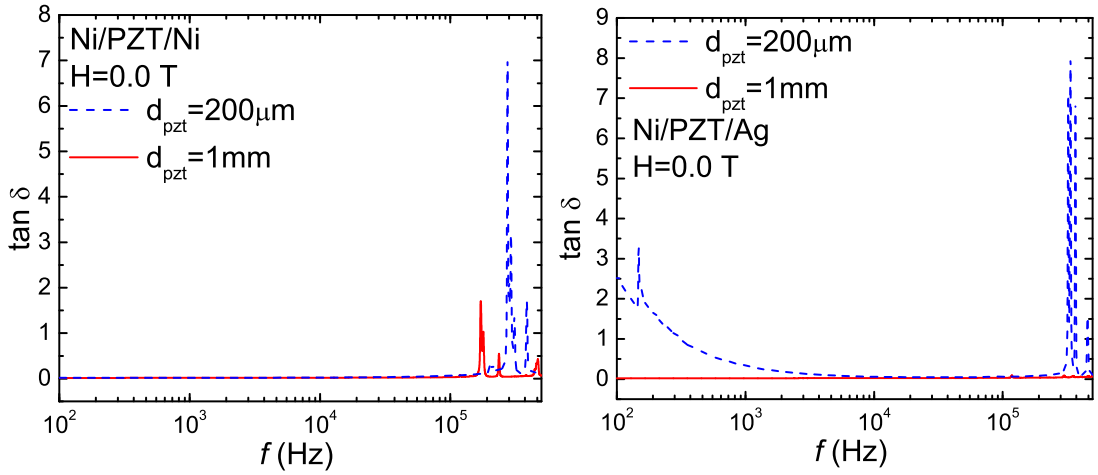

Figure 5.9: Loss coefficient ($\tan(\delta)$) of (a) 1mm PZT and 200μm with Ni/PZT/Ni configuration and (b) 1mm PZT and 200μm with Ni/PZT/Ag at 0T and room temperature.

electric loss coefficients represents the electrical loss due to dissipation of energy. Figure 5.9 show the dielectric loss coefficient of samples Ni/PZT/Ni with both thicknesses (5.9a) and Ni/PZT/Ag with both thicknesses (5.9b). In Figure 5.9a we observe that for the sample Ni/PZT/Ni, both thicknesses share very similar and stable low loss up until resonance after 1 MHz. On Figure 5.9b we observe that sample Ni/PZT/Ag with 1.00 mm thickness has a stable low loss behaviour until after 1 MHz, whereas the sample with 200 μm thickness starts with some loss and gradually falls to almost 0, followed by huge peaks at resonance after the 1 MHz mark. All these samples show high stableness and low loss. These have very promising device applications. Figure 5.10 show the Q-Factor spectroscopy of all Ni/PZT/Ni and Ni/PZT/Ag samples. Since Q is the inverse of the dissipation, we can see that for lower frequencies, the Q Factor is fairly linear in decay, but at resonance it exhibit large peaks.

Figure 5.11 show the phase angle spectra with both thicknesses of Ni/PZT/Ni (5.11a), Ni/PZT/Ag (5.11b), and Ag/PZT/Ag (5.11c). Here we can

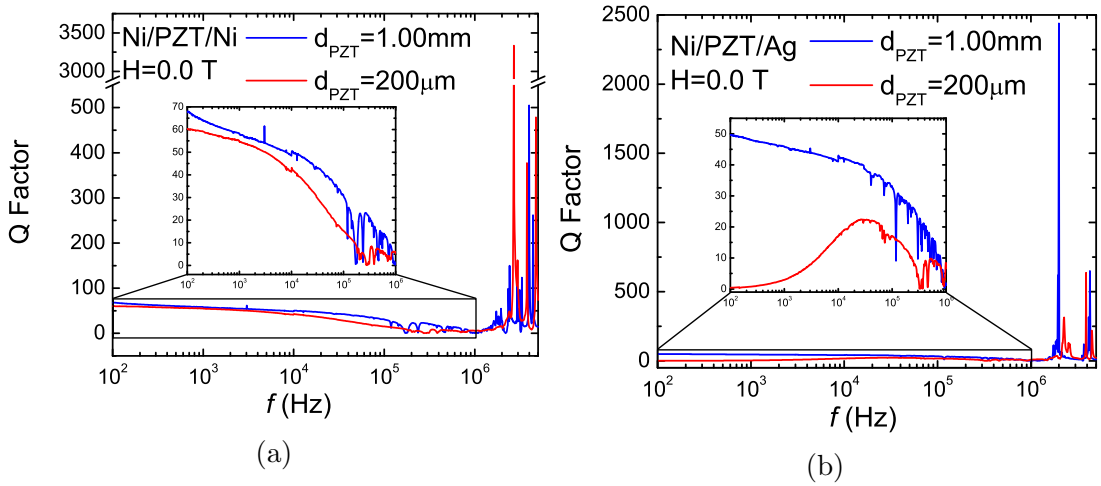

Figure 5.10: Q-Factor of 1mm PZT and 200μm with (a) Ni/PZT/Ni and (b) Ni/PZT/Ag configuration at 0T and room temperature.

appreciate the nature of the sample to behave as either a capacitor at certain frequencies, or as a resistor. All samples, except the Ni/PZT/Ag with 200 μm thickness, behave almost equal, all at almost -90°until after 1 MHz, where the resonance is present. For sample Ni/PZT/Ag with thickness 200 μm, we see that at 100 Hz starts almost 20°, and gradually falls to almost -90°. We can further compare with the simple capacitor Ag/PZT/Ag in Figure 5.11c. Here we see that it has very similar behaviour as the samples.

5.2.1.3 Impedance Spectroscopy

The impedance spectroscopy of the nickel based samples were obtained by the measurements of complex impedance, which includes its real (resistance) and imaginary (reactance) parts. The imaginary part holds all the information necessary to study the samples, including resistance values for the equivalent circuitry of the samples. Figure 5.12 show the imaginary part of the impedance for sample Ni/PZT/Ni with PZT thickness of 1.00 mm (5.12a) and 200 μm (**??**). These samples do not exhibit a peak on the measured range. Utilizing Jonscher's

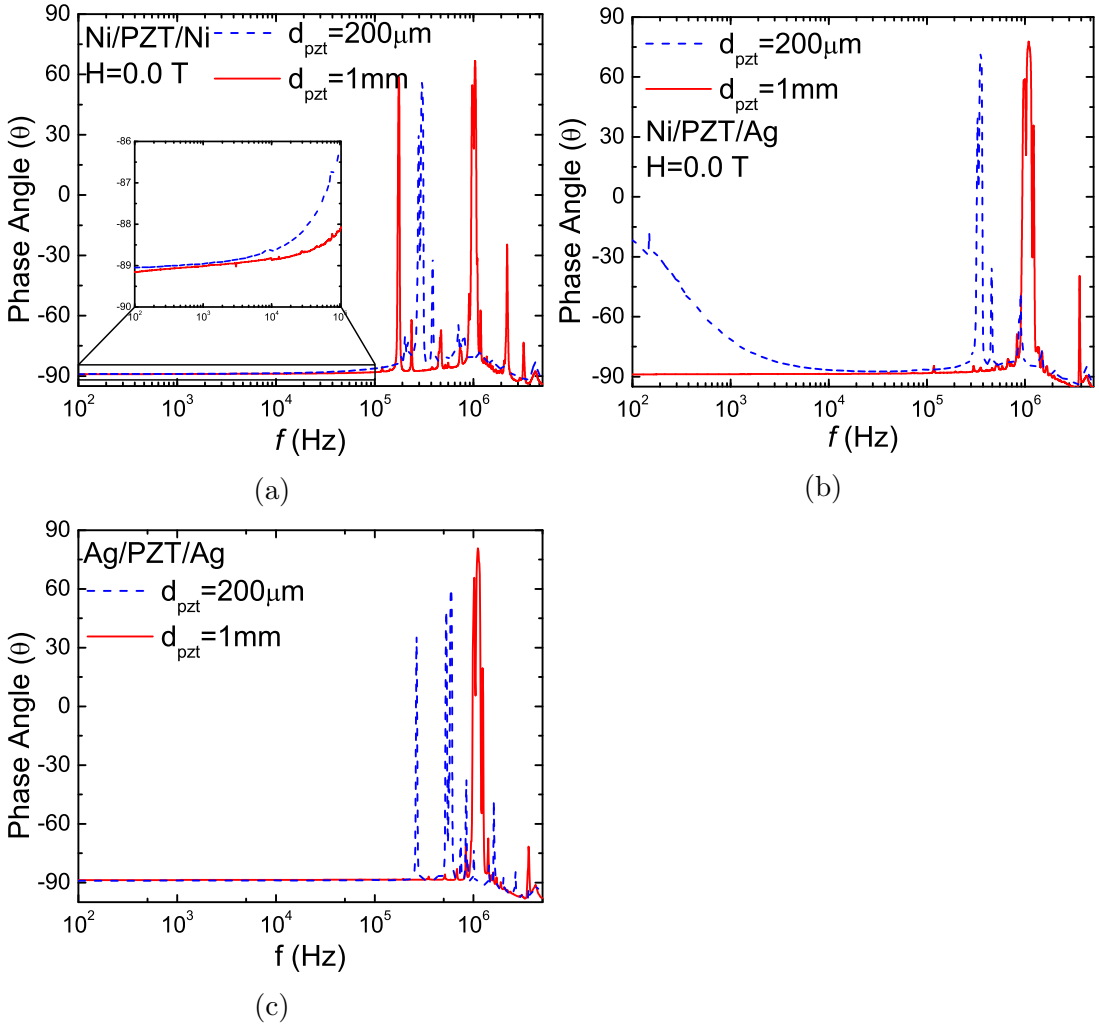

Figure 5.11: Phase Angle (θ) of (a) 1mm PZT and 200μm with Ni/PZT/Ni configuration, (b) 1mm PZT and 200μm with Ni/PZT/Ag, and (c) 1mm PZT and 200μm with Ag/PZT/Ag at 0T and room temperature.

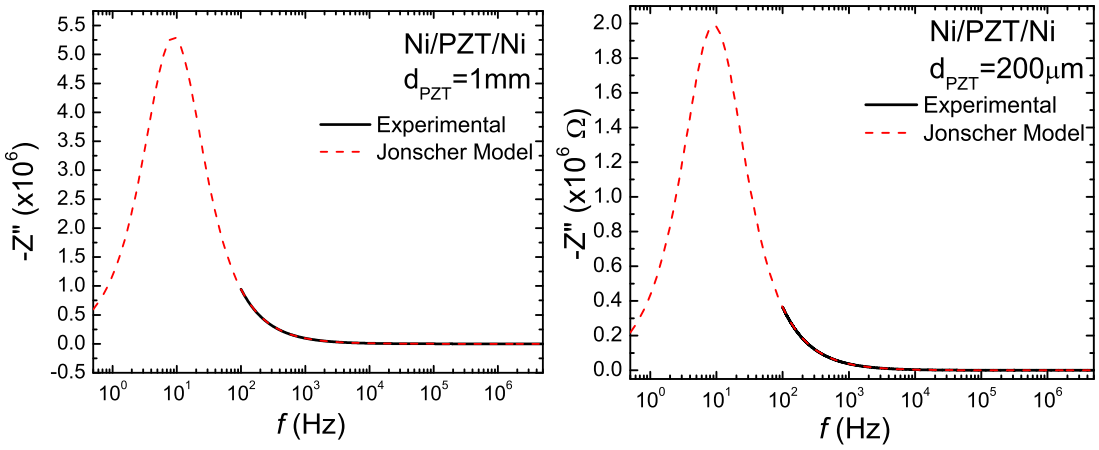

Figure 5.12: Frequency dependent reactance (Z") of Ni/PZT/Ni (a) d_{PZT}=1.00 mm and (b) d_{PZT}=200 μm.

dielectric response model mentioned in Section 2.2.2.4 and the equation [3, 4]:

$$Z" = R_g \left[\frac{\omega R_g C_g}{1 + (\omega R_g C_g)^2} \right] + R_{gb} \left[\frac{\omega R_{gb} C_{gb}}{1 + (\omega R_{gb} C_{gb})^2} \right] \tag{5.1}$$

We can extrapolate the peak and gather important information. Figure 5.12 demonstrate the fit of the Jonscher model on top of the measured experimental data. This give the values for the resistance and capacitance for the equivalent circuit which can be represented as two systems of a resistance parallel to a capacitance which are in series, better illustrated in Figure 5.13. Table 5.2 show all the important information obtained from the Jonscher model fit, including the resistance and capacitance values of the equivalent circuit. Here we observe the resistances for the grain (R_g), and the grain boundary (R_{gb}) are acceptable physical values. The same can be observed for the measured and extrapolated data of the Ni/PZT/Ag samples, where in Figure 5.15 it is shown the plotted and fitted Jonscher model. The sample Ni/PZT/Ag with 200 μm thickness does exhibit the peak, even though it's in the lowest part of the spectra and

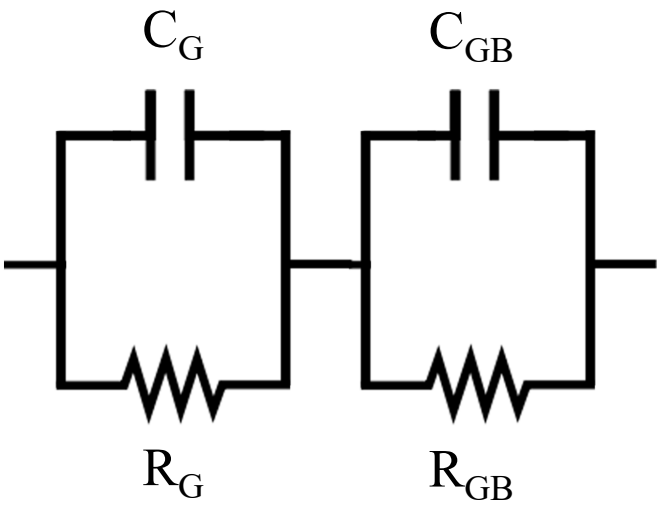

Figure 5.13: Equivalent circuit for samples with grain and grain boundary elements in series.

not complete. The values obtained by the fitting of the Jonscher model can be corroborated utilizing a fitting software of the nyquist plots using the real and imaginary parts of the samples. Since these samples have the peak outside of the measured spectra, the nyquist plot is not possible to build. For the 200 μm sample, since there is a peak in the imaginary part, but is not connected to the real part, the Nyquist plots take a non semi-circle shape. This means that is not a Debye relaxation.

From Table 5.2, we can observe that the thickness and presence of the ferromagnetic layer affect the placement of the peak in the spectrum. It is evident that thicker the sample, greater the resistance, since the charge has to travel a greater distance. The thickness as well brings closer to lower frequencies the thicker the sample, and with greater presence of ferromagnets, the higher the frequency of the peak. We can observe the difference between Ni/PZT/Ni and Ni/PZT/Ag. Ag/PZT/Ag is shown as well as a reference for a normal capacitor without the spin nature. The imaginary parts of the Ag/PZT/Ag samples are

Table 5.2: Important information from Z" utilizing Equation 5.1 for Ni/PZT/Ni and Ni/PZT/Ag.

Sample	R_g (Ω)	R_{gb} (Ω)	C_g (F)	C_{gb} (F)	f_{peak} (Hz)
Ni/PZT/Ni					
1.00 mm	1.06x10^7	4364	1.67x10^{-9}	5.9x10^{-8}	9.37
200 μm	4.0x10^6	1889	4.35x10^{-9}	1.54x10^{-7}	29794
Ni/PZT/Ag					
1.00 mm	9.22x10^6	5696	1.67x10^{-9}	4.61x10^{-8}	9.37
200 μm	1.82x10^5	141	3.5x10^{-9}	1.83x10^{-6}	243
Ag/PZT/Ag					
1.00 mm	6.56x10^6	5591	1.79x10^{-9}	4.51x10^{-8}	13
200 μm	1.16x10^7	5666	1.38x10^{-9}	4.68x10^{-8}	9.4

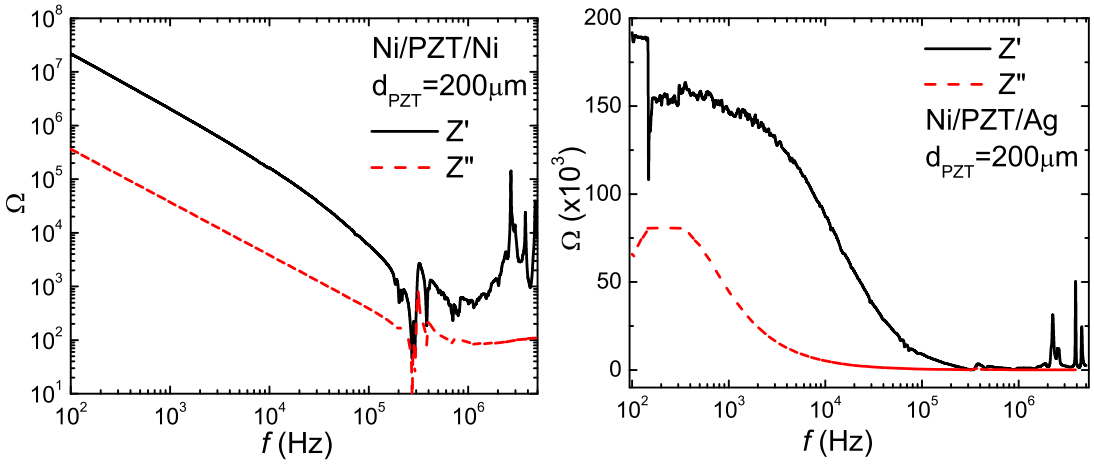

(a) (b)

Figure 5.14: (a) Complex impedance of Ni/PZT/Ni and (b) Complex impedance of Ni/PZT/Ag with thickness d_{PZT}=200 μm.

shown in Figure 5.16

5.2.1.4 Magnetic Properties

In order to understand the magnetodielectric coupling, magnetocapacitance and magnetoimpedance of the heterostructures were measured at room temperature. The samples were subjected to varying magnetic field with a strength up

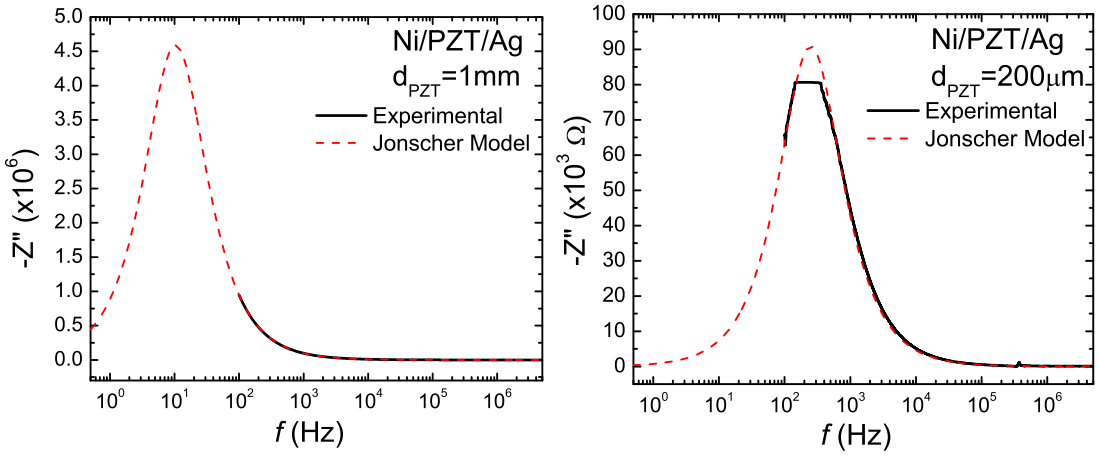

Figure 5.15: Frequency dependent reactance (Z") of Ni/PZT/Ag (a) d$_{PZT}$=1.00 mm and (b) d$_{PZT}$=200 μm.

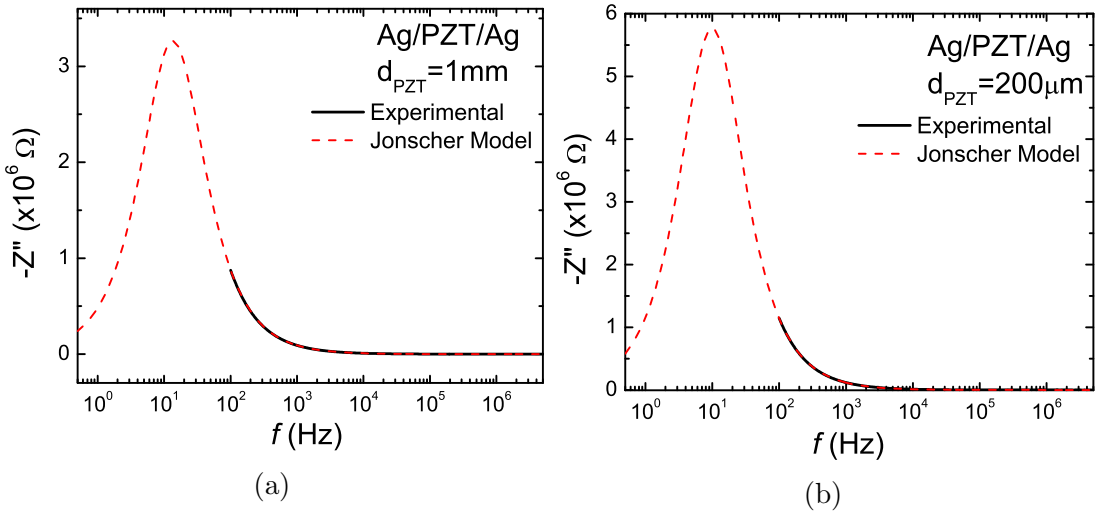

Figure 5.16: Frequency dependent reactance (Z") of Ag/PZT/Ag (a) d$_{PZT}$=1.00 mm and (b) d$_{PZT}$=200 μm.

to 2 T. At specific ranges, dielectric measurements were done and compared to each other to determine a difference through the magnetic range. The magneto-capacitance was obtained using Equation 2.33. Similarly, all the magneto related measurements by percentage were calculated using the same equation.

Figure 5.17a show the magnetocapacitance for sample Ni/PZT/Ni with PZT thickness of 1.00 mm at specific frequencies in forward and reverse magnetic field

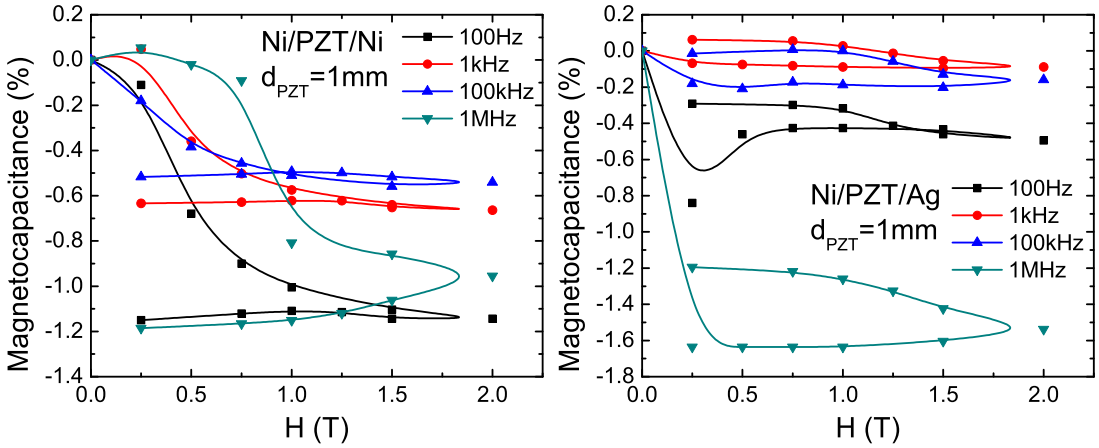

Figure 5.17: Magnetocapacitance of (a) Ni/PZT/Ni and (b) Ni/PZT/Ag with d_{PZT}=1.00 mm at frequencies 100 Hz, 1 kHz, 100 kHz, and 1 MHz.

(0-2 T) sweeps. As can be seen in Figure 5.17a, the magnetocapacitance is fairly low for these frequencies (1 kHz, and 100 kHz), only reaching a maximum of -0.5% and -0.6%. This sample has a loop pattern, which means that it has hysteresis. On the other hand, at 100 kHz and 1 MHz, the magnetocapacitance is higher, and the magnetocapacitance reaching both almost -1.2%. This can be expected since at this frequency range the sample becomes more erratic by resonance.

Figure 5.17b show the magnetocapacitance of sample Ni/PZT/Ag with PZT thickness of 1.00 mm in the same conditions as previous samples of Ni/PZT/Ni. It is observable that the magnetocapacitance has a fairly loop shape, but the difference in MC is not high. For the range of 1 MHz, the MC reaches -1.6% and back down to -1.2%.

Figure 5.18a show the magnetocapacitance for sample Ni/PZT/Ni with PZT thickness of 200 μm at specific frequencies in forward and reverse magnetic field (0-2 T) sweeps. As can be seen, the magnetocapacitance is similar to the previous samples. On the other hand, sample Ni/PZT/Ag (Figure 5.18b with 200 μm

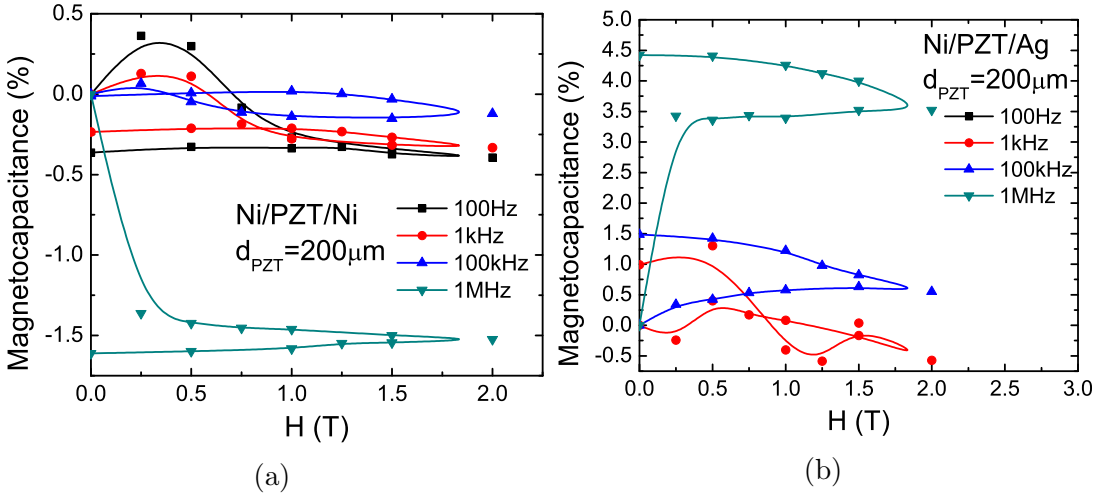

Figure 5.18: Magnetocapacitance of (a) Ni/PZT/N and (b) Ni/PZT/Ag with d_{PZT}=200 μm at frequencies 100 Hz, 1 kHz, 100 kHz, and 1 MHz.

thickness show higher MC, with the 1 MHz range reaching up to 4.5%, and 1 kHz and 100 kHz reaching 1% and 1.5% respectively.

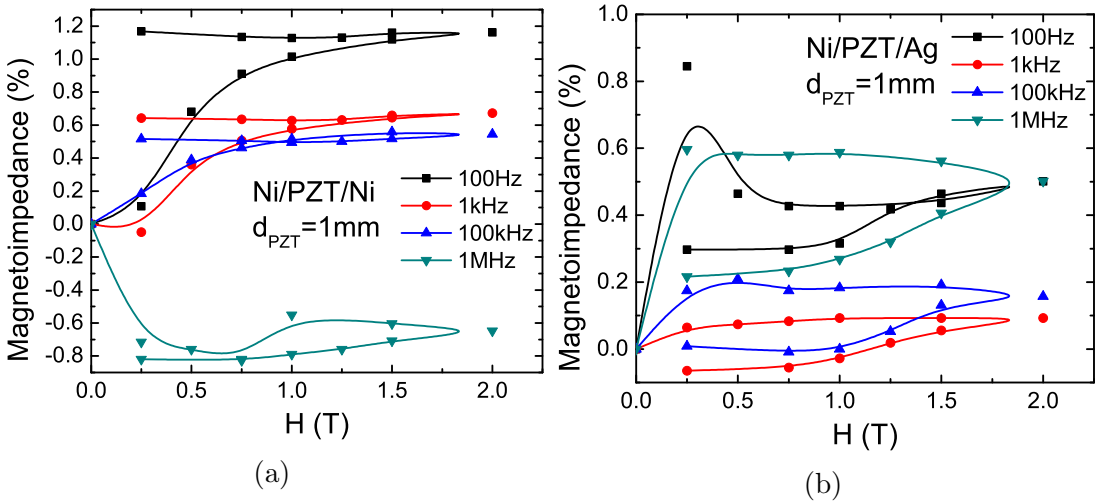

Figure 5.19: Magnetocapacitance of (a) Ni/PZT/Ni and (b) Ni/PZT/Ag with d_{PZT}=1.00 mm at frequencies 100 Hz, 1 kHz, 100 kHz, and 1 MHz.

Comparing Ni/PZT/Ni and Ni/PZT/Ag, we observe that both samples of 1.00 mm thick, share striking similarities. On the other hand, the thinner 200 μm sample has higher percent of magnetocapacitance at 1 MHz. These results can

be interpreted that the 200 μm samples have higher magnetodielectric coupling.

To establish the existence of magnetodielectric coupling, frequency dependent magnetoimpedance measurements were carried out at room temperature. As shown in Figure 5.19, we observe the magnetoimpedance of both samples Ni/PZT/Ni and Ni/PZT/Ag with PZT thickness of 1.00 mm. Both show low magnetoimpedance. From Figure 5.19a we observe that for the Ni/PZT/Ni, the 1 MHz range fall to the negative side, reaching approximately -0.8%. Whereas the lower frequencies reach almost 1.2% at 100 Hz, 0.65% at 1 kHz, and 0.5% at 100 kHz.

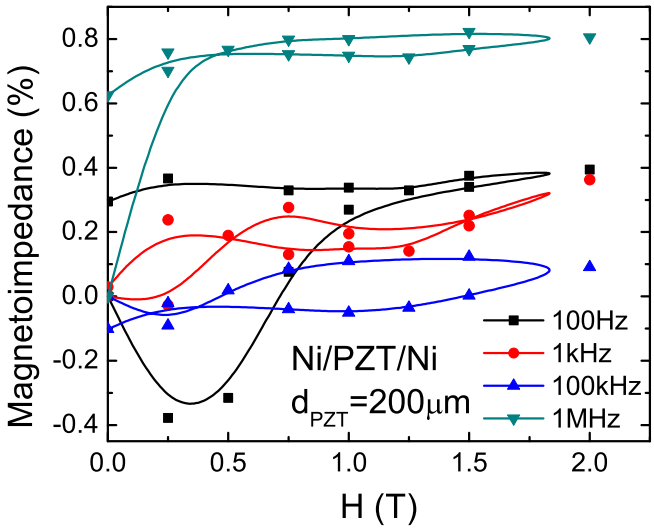

Figure 5.20: Magnetoimpedance of Ni/PZT/Ni with d_{PZT}=200 μm at frequencies 100 Hz, 1 kHz, 100 kHz, and 1 MHz.

Figure 5.20 show the magnetoimpedance of sample Ni/PZT/Ni with PZT thickness of 200 μm. We can see that for 100 Hz , the MZ falls to the negative side and then rise to the positive, reaching at 0.3%. The 1 kHz range does a loop that ends almost at 0%, the 100 kHz does similar but on the negative side. The 1 MHz range rises and stays at approximately 0.65%.

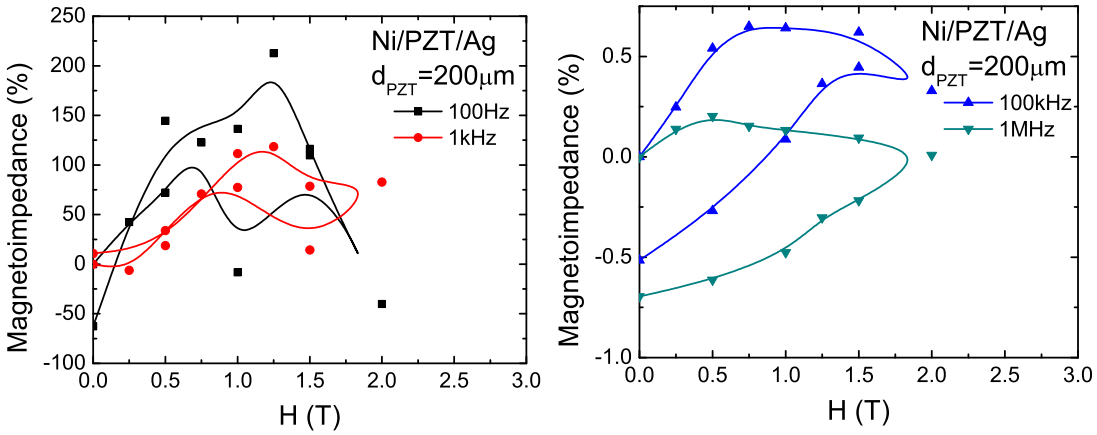

Figure 5.21: Magnetoimpedance of Ni/PZT/Ag with d_{PZT}=200 μm at frequencies (a) 100 Hz and 1 kHz, (b) 100 kHz and, 1 MHz.

All the samples show similarities that at higher frequencies there are bigger changes by the applied magnetic field. This information show that there is magnetodielectric coupling. Ferroelectric polarization measurements were carried out using Marine PE loop tracer.

5.2.1.5 Ferroelectric Polarization

Figure 5.22 show the ferroelectric polarization due to an electric field at varied applied magnetic flux. We can observe that there is polarization and magnetization. The Ag/PZT/Ag (Figure 5.22d) sample, which is our reference capacitor, we observe that the remanent polarization is very close to that observed in literature [6]. As well, we see that there is no difference with an applied field. This is expected since this sample lack the ferromagnetic element. Once the ferromagnetic element is present, we observe considerable change. The actual percentage of difference from without the applied magnetic field to when the field is applied can be observed of Figure 5.23. This magnetopolarization is significant, reaching up to 14% for Ni/PZT/Ag (1.00 mm), 6.5% for Ni/PZT/Ni

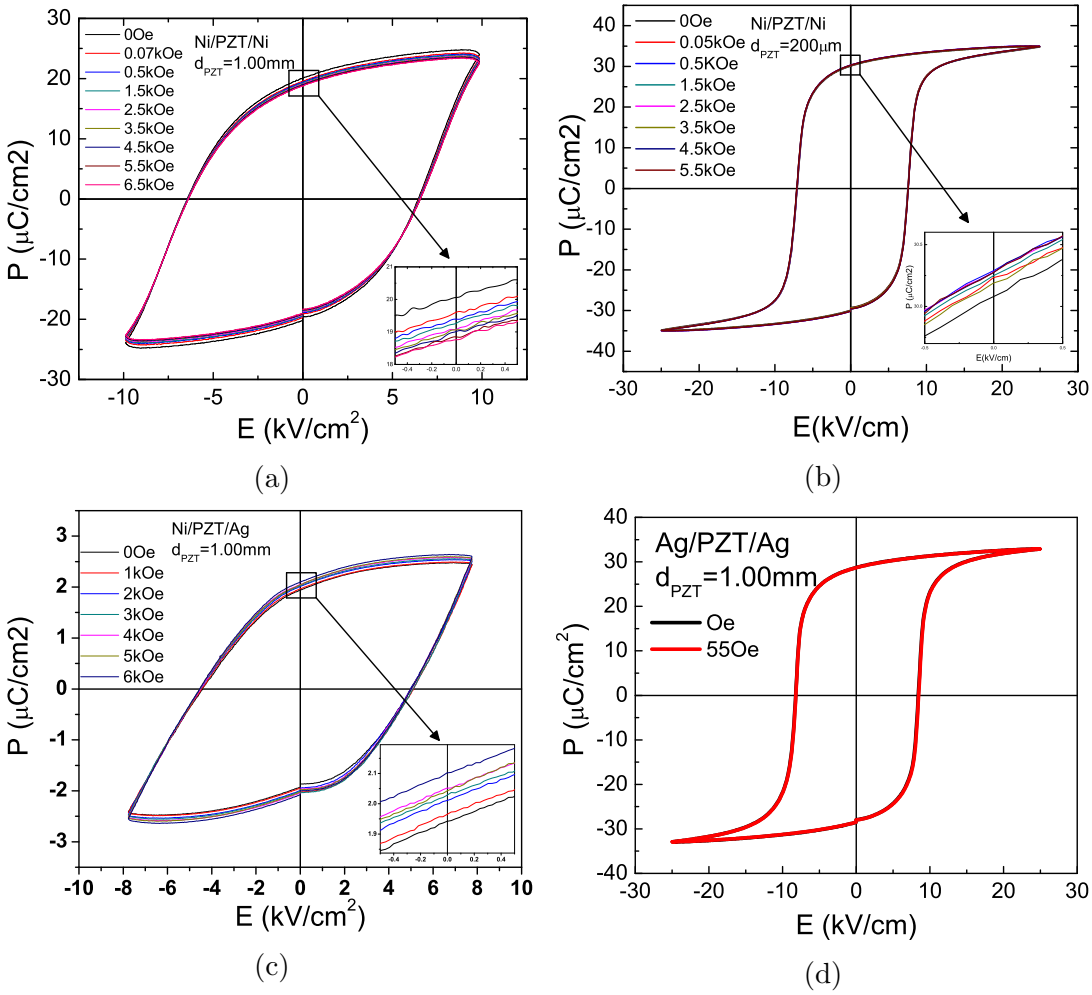

Figure 5.22: Ferroelectric polarization of Ni/PZT/Ni with (a) 1.00 mm and (b) 200 μm thickness, (c) for Ni/PZT/Ag of 1.00 mm, and (d) Ag/PZT/Ag with 1.00 mm thickness.

(1.00 mm), and 0.7% for Ni/PZT/Ni (200 μm).

5.2.2 Thin Samples

These samples where put through a AFM/Profilometer to determine their thickness. The measured average thickness of two selected samples where of 2 μm and the thicker one being of 7 μm. The thickness achieved is "100" times thinner than the commercially obtained samples of 200μm. Following suit as with the samples done before, the SPL deposited Ni/PZT/Ni samples where subjected to

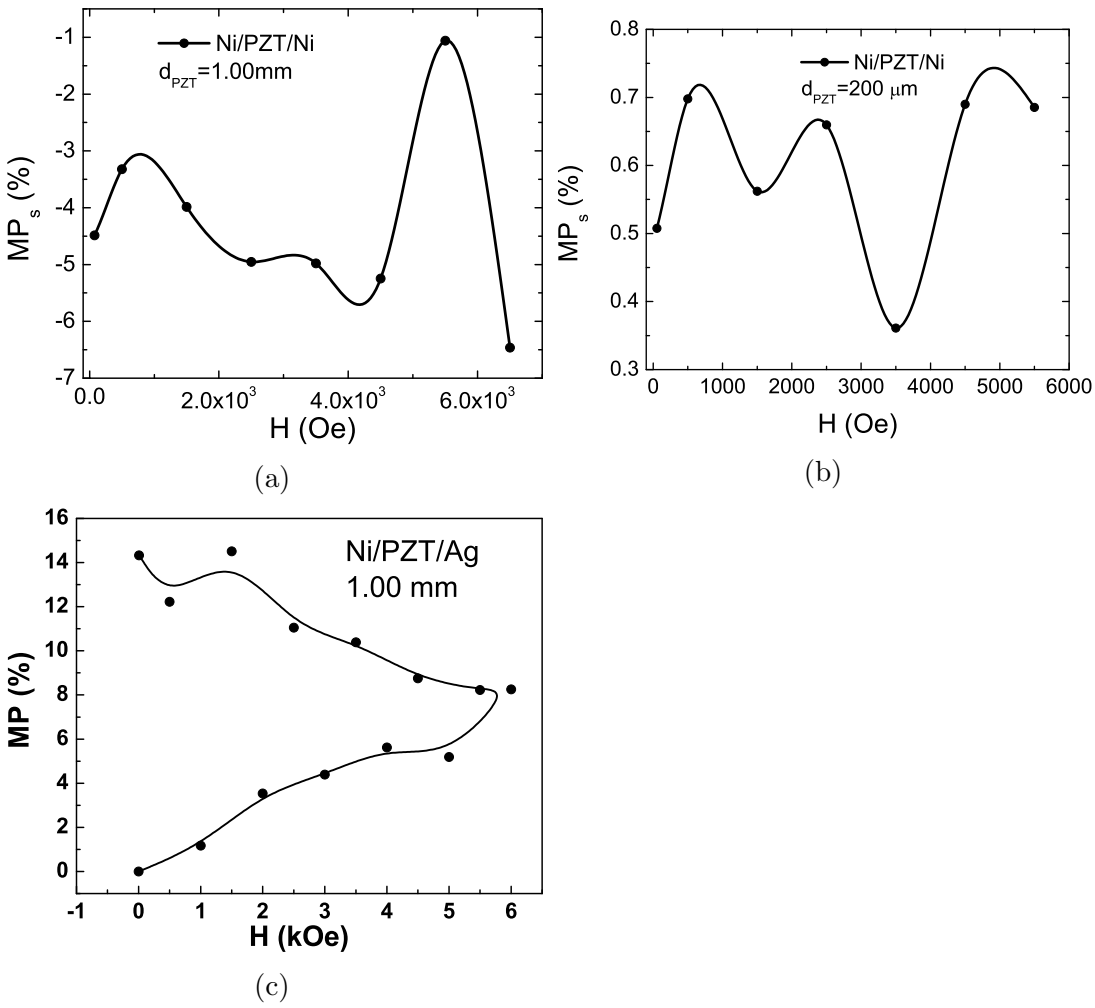

Figure 5.23: Magnetopolarization of Ni/PZT/Ni with (a) 1.00 mm, (b) 200 μm thickness, and (c) Ni/PZT/Ag with 1.00 mm PZT thickness.

the same measurements and conditions. Dielectric measurements where done in the range of 100Hz to 5GHz with a magnetic field presence from 0 T up to 2 T and back down.

5.2.2.1 Dielectric Permittivity

From Figure 5.24 we can observe the dielectric response of the samples. Both share very similar behaviour but different magnitude. The 2 μm sample (Figure 5.24a) starts at ≈8 and drops to ≈6 before 1 MHz, after it drops fith

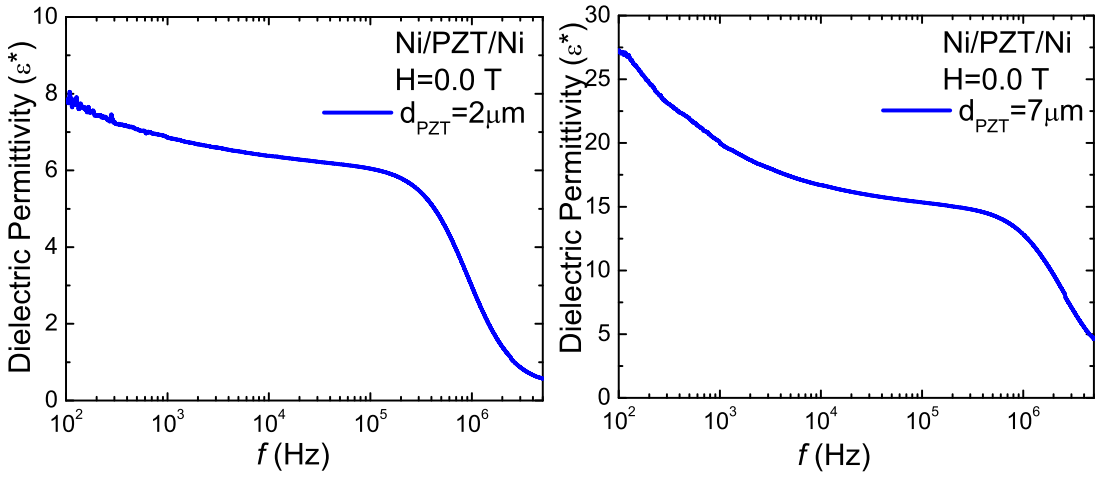

Figure 5.24: Dielectric permittivity of (a) Ni/PZT/Ni with d_{PZT}=2μm and (b) Ni/PZT/Co with d_{PZT}=7μm.

a fair negative slope until reaching 0.5. The 7 μm sample has higher dielectric permittivity, starting at 27 and droping to 15 before 1 MHz, a greater rate that the thinner sample. After 1 MHz, it drops down to 5. These samples show very ferroelectric behaviour and almost no interference nor resonances at high frequencies. We can further analyze the samples with the divided complex permittivity. Figure 5.25 shows the complex dielectric permittivity and its real and imaginary parts. With this we can observe the dielectric response of the samples and we see that both share similar behaviour. The important observation is that they seem to have two relaxations present since there are two drops in the real part and one wide peak in the imaginary. This wide peak can be two peaks convoluted into one. Since this behaviour is before and at 1 MHz, we can determine that there is space-charge relaxation, but can mean that since the sample is a heterostructure of two materials, then each relaxation can be for each.

Table 5.3 show important information of the broad peak of both samples.

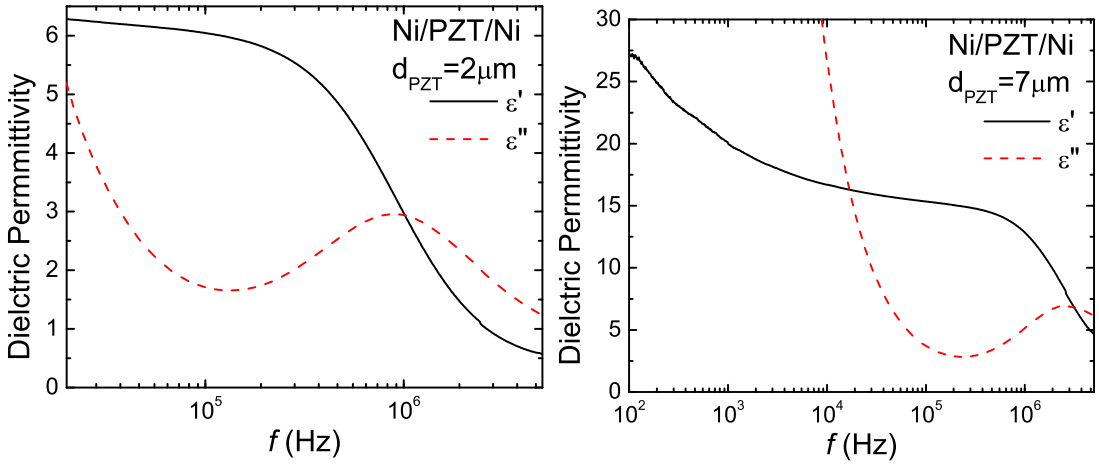

Figure 5.25: Complex permittivity of Ni/PZT/Ni thin samples illustrating the real and imaginary parts.

Table 5.3: Frequency information of the broad peak in the imaginary part of Ni/PZT/Ni.

Ni/PZT/Ni	$\mathbf{d}_{PZT}$**=2** μ**m**	$\mathbf{d}_{PZT}$**=7** μ**m**
$\boldsymbol{f}_{peak}$	82 kHz	109 kHz
τ	1.23x10^{-5} s	9.15x10^{-6} s
Q Factor	0.12	0.05
Max Dielectric	5.8	15

Since it is a very broad peak, the Q factor is very low, but then again, this peak can be a sum o two narrower peaks for each relaxation.

5.2.2.2 Phase Angle and Dielectric Loss

Both samples at low frequencies start as resistors, given that the bias voltage was of 1V, and that the sample is very thin, it behaves as a resistor, but at further frequencies it starts to shift towards the negative side, reaching towards -90°. For it to be a full capacitor, it must reach -90°. This is shown in Figure 5.26. This means that it has high loss current, and this can be proved and observed further

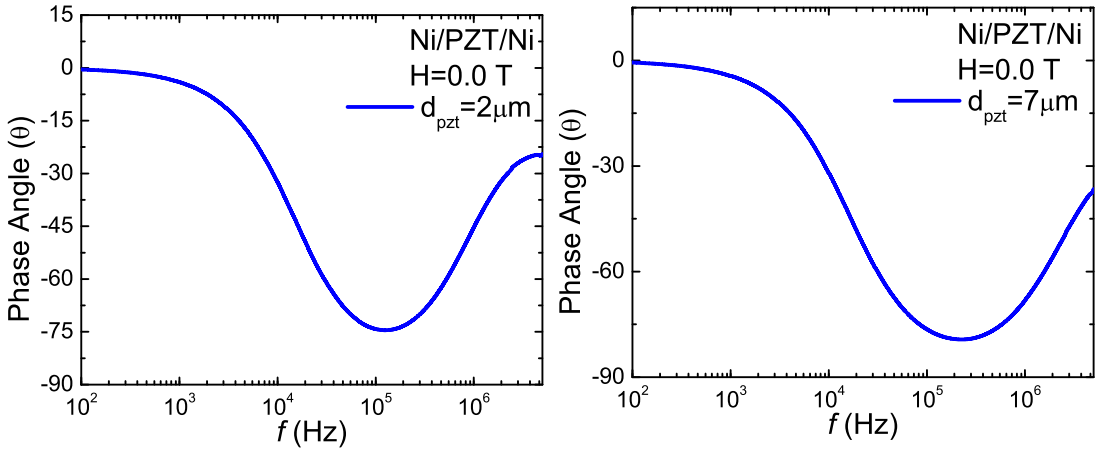

Figure 5.26: Phase angle of SPL deposited (a) d_{PZT}=2μm PZT thickness and (b) d_{PZT}=7μm with Ni/PZT/Ni configuration at 0T and room temperature in the frequency range of 100Hz to 5MHz.

with the loss coefficient graph shown in Figure 5.27a. Here we can observe that for both samples there is high current loss. Both samples behave very similar until after 10^5 Hz, where the 2 μm sample increase faster until was seems to be the edge of a peak.. Where the phase angle approaches to the lower negative sides, towards -90°, we observe that the loss coefficient lowers closer to 0. Again, when we have lower, to no dissipation and current loss, we arrive to capacitors area, where there is energy storage. This samples are not that lossy. The Q Factor is the inverse on the loss coefficient, meaning that where there is a peak in Q factor, it has best qualities. Figure 5.27b show the Q factor, and as stated, where the loss is at a minimum, the Q factor is at highest. The 2 μm sample show lower Q factor peak of height ≈3.5 and the 7 μm sample reaching ≈5.4.

5.2.2.3 Impedance Spectroscopy

The impedance measurements offers a great spectrum of information of the samples, most data obtained are derived from the impedance of the sample.

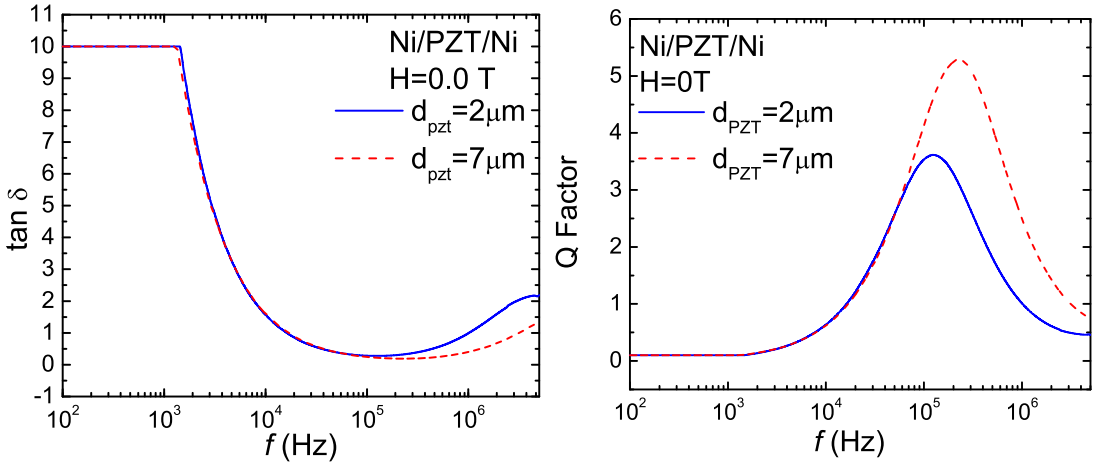

Figure 5.27: (a) Loss Coefficient of SPL deposited d_{PZT}=2μm PZT thickness and d_{PZT}=7μm, and (b) Q factor with Ni/PZT/Ni configuration at 0T and room temperature in the frequency range of 100Hz to 5MHz.

Here in Figure 5.28 we observe the sample's resistive behaviour by impedance. Since these samples have a very thin thickness we can see that there is a limit of impedance on lower frequencies. This is where we see higher loss current. This is followed by normal exponential decay. The impedance is composed by both real and imaginary parts, these can be observed on Figure 5.28a for the 2 μm sample and 5.28b for the 7 μm sample. Figure 5.28a we see that for the sample with thickness of 2 μm, the real and imaginary parts intersect, almost at the highest point of the peak. This means that the relaxation does not have a strict Debye response. The same can be observed with sample 7 μm (5.28b). For a true Debye response, this occurs exactly in the center. Utilizing the Jonscher model we can obtain all the important information of the equivalent circuitry. This information is present in Table 5.4, where the resistance and capacitance of the grains and grain boundary are shown. These are derived from the Jonscher model using Equation 5.1. The fit can be observed on Figure 5.29 for both samples.

Figure 5.30 show the Nyquist plots for the samples Ni/PZT/Ni with thick-

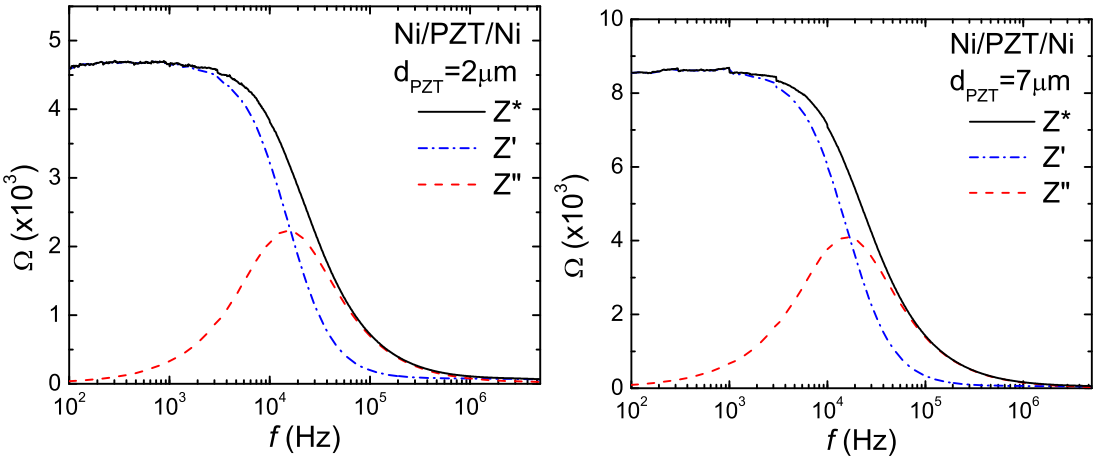

Figure 5.28: Complex impedance of SPL deposited (a) d_{PZT}=2μm PZT thickness and (b) d_{PZT}=7μm with Ni/PZT/Ni configuration at 0T and room temperature in the frequency range of 100Hz to 5MHz with the real (Z') and imaginary (Z") parts.

Table 5.4: Important information from impedance spectroscopy utilizing Equation 5.1 and Nyquist plot for Ni/PZT/Ni thin film samples.

Sample	$\mathbf{R}_g$ **(Ω)**	$\mathbf{R}_{gb}$ **(Ω)**	$\mathbf{C}_g$ **(F)**	$\mathbf{C}_{gb}$ **(F)**	$\boldsymbol{f}_{peak}$ **(Hz)**
2 μm	3899	702	$2.43\text{x}10^{-9}$	$2.88\text{x}10^{-8}$	15897
7 μm	7436	1247	$1.20\text{x}10^{-9}$	$2.20\text{x}10^{-8}$	16601

ness d_{PZT}=2 μm (5.30a), and d_{PZT}=7 μm (5.30b). These samples, since the imaginary peak is present within the measured spectra, we can obtain a Nyquist plot, which in turn enables us to simulate an equivalent circuit and fit to the experimental data. After simulating the circuit described in Figure 5.13, and within Figure 5.30, we obtain information and values for the circuit of the grain and grain boundary. This is corroborated with the Jonscher model with Equation 5.1 and the information in Table 5.4, and obtain equal results. For both samples, we can observe that the semi-circle start close to 0 Ω, this means that there is a negligible starting resistance which can be attributed to the contacts between the sample and the measuring device. The solid line in Figure 5.30

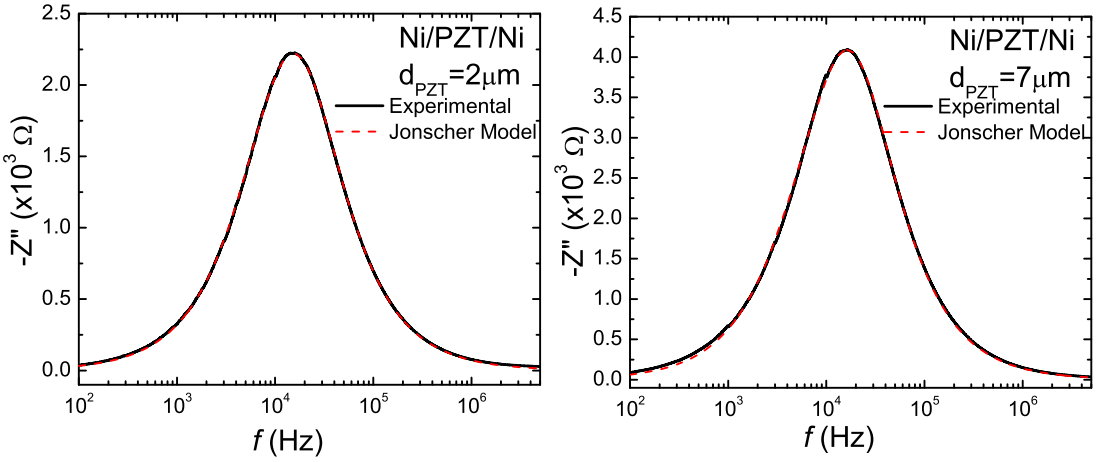

Figure 5.29: Imaginary part of SPL deposited (a) d_{PZT}=2μm PZT thickness and (b) d_{PZT}=7μm with Ni/PZT/Ni configuration at 0T and room temperature in the frequency range of 100Hz to 5MHz with the Jonscher model fitting.

shows simulated fit of equivalent circuit to the data using a an electrochemical impedance spectroscopy (EIS) spectrum analyser software [5].

5.2.2.4 Magnetic Properties

In order to understand the magnetodielectric coupling, magnetocapacitance and magnetoimpedance of the thin film heterostructures were measured at room temperature. The samples were subjected to varying magnetic field with a strength up to 2 T. At specific ranges, dielectric measurements were done and compared to each other to determine a difference through the magnetic range. The magnetocapacitance was obtained using Equation 2.33. Similarly, all the magneto related measurements by percentage were calculated using the same equation.

Figure **??** show the magnetocapacitance sample Ni/PZT/Ni with thickness 7 μm. The 2 μm sample, since the thin film is very delicate, did not provide workable results. With the 7 μm should be enough to prove the presence of the

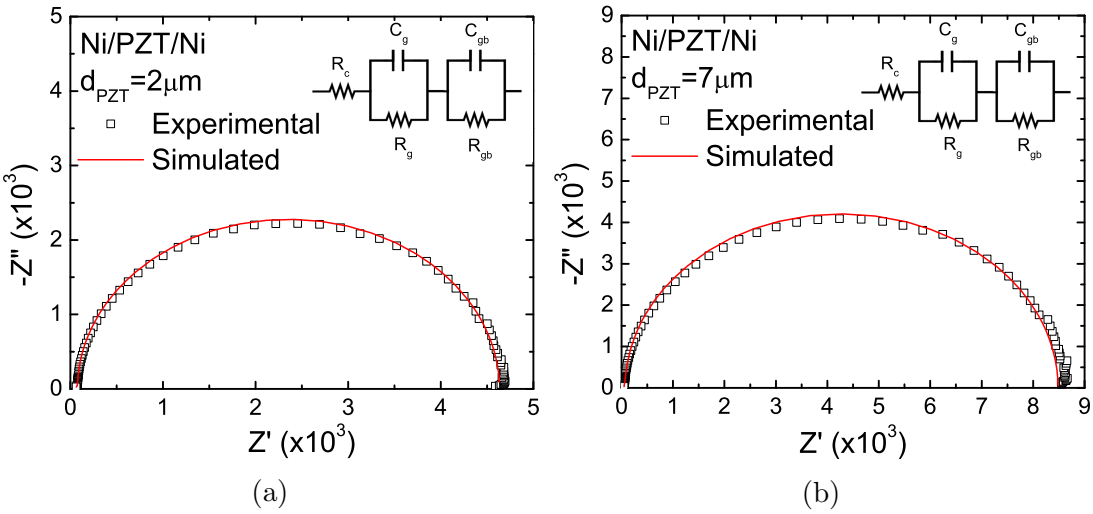

Figure 5.30: Real and imaginary parts from the impedance graphed in a Nyquist plot of SPL deposited (a) d_{PZT}=2 μm PZT thickness and (b) d_{PZT}=7 μm with Ni/PZT/Ni configuration at 0T and room temperature in the frequency range of 100Hz to 5MHz. The Jonscher model is fitted and the equivalent circuit presented.

magnetoelectric coupling with both magnetocapacitance and magnetoimpedance in Figure 5.32. The MC values show fair magnitudes, reaching -7% at 1 kHz and almost -20% at 100 kHz. These are strong values, and the hysteresis shape is present, retaining MC at the end of the loop.

Figure 5.32 show the magnetoimpedance of the 7 μm sample. We can observe that both frequencies share a common path and magnitude. They reach almost 10% and have a rising hysteresis shape. The negative MC suggest a common magnetostrictive origin for the magnetic field dependence of the two quantities.

5.3 Summary

There are vast differences in magnitude when we compare the bulk samples (1.00 mm and 200 μm) with the thin film samples (2 μm and 7 μm). It is evident that the thickness plays a huge factor, specially with the resistance and capacitance of the sample. The best result for magnetoelectric coupling can be

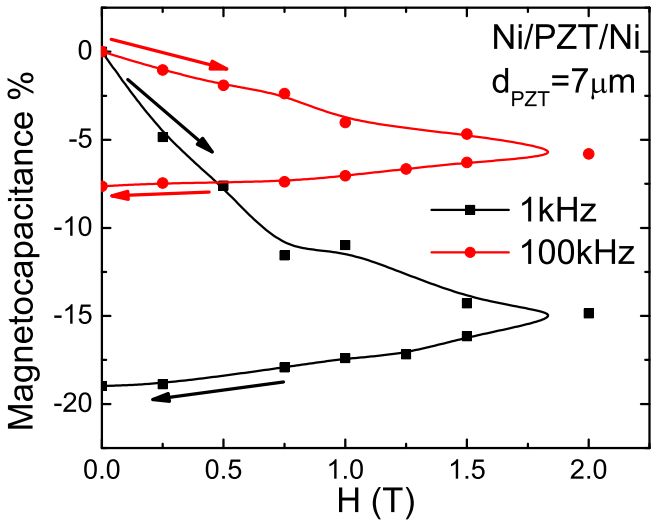

Figure 5.31: Magnetocapacitance of Ni/PZT/Ni with d_{PZT}=7 μm at frequencies 1 kHz and 100 kHz.

observed for the thin film samples. this makes then good for device applications, specially the fact that they are made by spray pyrolysis, a very cost effective alternative for thin film growth. It is great to observe that these samples offer great magnetoelectric coupling and robust behaviour for a wide range in the spectra [7, 8].

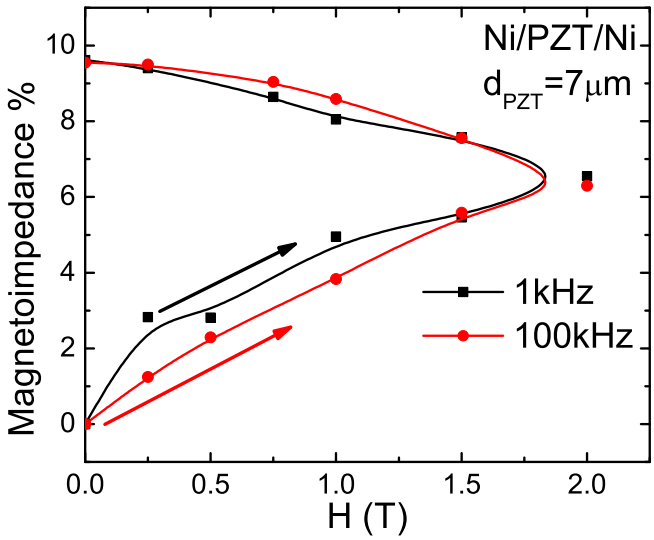

Figure 5.32: Magnetoimpedance of Ni/PZT/Ni with d_{PZT}=7 μm at frequencies 1 kHz and 100 kHz.

References

[1] Yarmarkin, V. K., Teslenko, S. P., Dielectric relaxation in thin-film metalPZT-ferroelectricmetal structures, Phys. Solid State 40, 17381741 (1998)

[2] Wu, Dawei et al. Dielectric and Piezoelectric Properties of PZT Composite Thick Films with Variable Solution to Powder Ratios. Journal of the American Ceramic Society. American Ceramic Society vol. 92,6 (2009)

[3] Swagatika Dash, R. Padhee, Piyush R. Das & R.N.P. Choudhary, Dielectric and impedance spectroscopy of (Bi0.5Li0.5)(Fe0.5Nb0.5)O3 multiferroics, Phase Transitions, 87:3, 223-235 (2014)

[4] Jonscher AK. The universal dielectric response. Nature. 1977;267:673679.

[5] Bondarenko A. S., Ragoisha G. A. In Progress in Chemometrics Research,

Pomerantsev A. L., Ed.; Nova Science Publishers: New York, pp. 89102 (2005)

[6] M. W. Hooker, Properties of PZT-Based Piezoelectric Ceramics Between -150 and 250C, NASA/CR-1998-208708 (1998)

[7] Y. Zhou, D. Maurya, Y. Yan, G. Srinivasan, E. Quandt, S. Priya, Self-Biased Magnetoelectric Composites: An Overview and Future Perspectives. Energy Harvesting and Systems. 3. 10.1515 (2015)

[8] Jia Y, Zhou W, Ma K, Liu Y. Enhanced Magnetoelectric Effect in Permendur/Pb(Zr0.52Ti0.48)O3 Laminated Magnetostrictive/Piezoelectric Composite. Applied Sciences. 5(3):587-594. (2015)

Chapter 6

Conclusion and Future Work

$Pb[Zr_xTi_{1-x}]O_3$(PZT) is one of the most studied piezoelectric ceramic, thanks to its great piezoelectric coefficient, and high ME and MD coupling. In order to study and further understand the MD coupling, in the present work ferromagnetic/ferroelectric heterostructures, using the most common and greatest ferromagnets (Fe, Co, and Ni), were made in the shape of a capacitor and systematically investigated.

In this thesis, we report the synthesis and suitable approach to study the magnetodieelectric (MD) coupling of PZT with a ferromagnet fabricated in shape of a spin capacitor by various methods. This had the shapes of Fe/PZT/Fe, Co/PZT/Co, Ni/PZT/Ni with silver being alternated in place of one of the ferromagnetic layers and Ag/PZT/Ag as a reference normal capacitor without the spin part. The samples were systematically characterized and examined to study the heterostructure correlation with the MD coupling. Detail of the structural, dielectric, ferroelectric, impedance, and magnetodielectric properties have been shown in the light of the magnetic ordering at room temperature [1–4].

The dielectric permittivity of the PZT based samples are characterized by a rapid decrease of the permittivity and a loss peak in the GHz frequency range, this is contributed by both domain wall motion and piezoelectric grain resonances related to the brick layer model. The dielectric and electrical properties as a function of the magnetic field indicated the signature of ME coupling in all samples, where the thinner show best outcome and enhanced ME and MD coupling. The Ni/PZT/Ni samples show better robust and stable dielectric response

for the frequency range of 100 Hz up to almost 1 MHz, after that, resonances are present, but not on the thin film samples. This study determined that the relaxation process occurring relaxation process occurring in our samples are of the kind of space charge Polarization. The thin film growth process of spray pyrolysis has proven effective for PZT as the material. These films had a semi-rough nature, some did not adhere properly, and inconsistent growth thickness per pass of the spray. This can be further studied and perfected in future works, were the equipment could be modified to tackle these deficiencies. The laminates can further be obtained for the specific ferromagnet desired and specific thickness. As well the surface roughness or smoothness to improve better film adherence. This can prove to be a cost effective alternative to grow thin films on various substrates of any shape.

6.1 Publications

F.J. Aponte Rivera, R. Palai, Nucleation, Growth, and Electrical Characterization of Al2O3 Thin Films Grown by Atomic Layer Deposition, (2015). (M.S. Thesis).

F. Aponte, R. Masso, K. Dasari, G. Sreenivasulu, G. Srinivasan, R. Palai, Magnetodielectric coupling in Ferromagnetic/Ferroelectric/Ferromagnetic spin capacitor, MRS Adv. 2 (2017) 241246. DOI:10.1557/adv.2017.31.

R Masso, S N Tripathy, F J Aponte, D K Pradhan, R Martinez, R Palai, 2021 Mater. Res. Express 8016302

References

[1] Narendra Babu, S., Siddeshwar, A., Srinivas, K. et al. Magnetoelectric properties of Ni/PZT/Ni layered composite for low field applications. J Mater Sci 44, 39483951 (2009)

[2] D A Pan, Y Bai, W Y Chu and L J Qiao, NiPZTNi trilayered magnetoelectric composites synthesized by electro-deposition, J. Phys.: Condens. Matter 20 025203 (2007)

[3] D.A. Pan, J.J. Tian, S.G. Zhang, J.S. Sun, A.A. Volinsky, L.J. Qiao, Geometry effects on magnetoelectric performance of layered Ni/PZT composites, Materials Science and Engineering: B,Volume 163, Issue 2, (2009)

[4] V.M. Laletin, N. Paddubnaya, G. Srinivasan, C.P. De Vreugd, M.I. Bichurin, V.M. Petrov, D.A. Filippov, Frequency and field dependence of magnetoelectric interactions in layered ferromagnetic transition metal-piezoelectric lead zirconate titanate, Appl. Phys. Lett. **87**, 1-3 (2005)